Report on the activity of the GILDA-CRG beamline 2009-2013

1 April 2014

F. d'Acapito[@], A. Trapananti[@], S. Torrengo[@], S. Mobilio[#,$], F. di Benedetto[‰], F. Boscherini[^], G. Giuli[&], P. Ghigna[*], A. Gualtieri[\], S. Mangani[=], C. Maurizio[>]

[@] *CNR-IOM-OGG, Grenoble (France),* [#] *Univ. Roma Tre, Dip di Fisica, Roma (Italy),* [$] *INFN, Lab. Naz. Frascati, Frascati (Italy),* [‰] *Univ. di Firenze, Dip. di Scienze della Terra, Firenze (Italy),* [^] *Univ di Bologna, Dip. Di Fisica,* [&] *Univ. Camerino, Dip di Scienze della Terra, Camerino (Italy),* [*] *Univ. di Pavia, Dip. Di Chimica Pavia, (Italy),* [\] *Univ di Modena e Reggio Emilia, Dip di Scienze della Terra, Modena (Italy),* [=] *Univ. di Siena, dip di Chimica, Siena (Italy),* [>] *Univ. di Padova, Dip di Fisica, Padova (Italy)*

Index

Technical description of the beamline

Introduction

The Italian Collaborating Research Group GILDA [Dacapito-98] is a general-purpose beamline built on a bending magnet source (BM08) of the ESRF. It is co-funded and operated by two major Italian public research institutes, Consiglio Nazionale delle Ricerche (CNR) and Istituto Nazionale di Fisica Nucleare (INFN). The beamline is operational since 1994 and it is specialized in techniques for the structural characterization of materials of importance in a very wide range of research fields. The two main techniques are X-ray Absorption Spectroscopy (XAS) and X-ray Diffraction (XRD). The GILDA beamline consists in four hutches: the first contains the optical elements and the three others the experimental apparata for different kind of experiments.

The first experimental hutch, is dedicated to X-ray Absorption Spectroscopy (XAS) and it is placed in the 1:3 horizontal focal configuration to obtain the maximum flux from the sagittally focusing monochromator. The wide energy range (potentially, 4-90 keV) of the beamline makes GILDA well-suited for XAS investigations on mid-heavy elements with the possibility to access the K absorption edges from Ca to Au and the L edges from Sb on. Experiments are carried out in transmission, fluorescence and total electron yield detection modes. For the study of highly diluted samples, solid state energy resolving detectors (two arrays of 13 and 12 high purity Ge diodes manufactured by ORTEC) are currently used (current limit sensitivity: ~50 ppm or ~10^{14} at/cm^2).

The second hutch, in 1:1 focal geometry, is dedicated to X-ray diffraction. Time-resolved (minutes-time scale) powder diffraction experiments can be performed, by using a 2-dimensional detector coupled to a hot air blower. A third experimental hutch at the end of the beamline equipped with an ultrahigh vacuum chamber is available, although not operative at the moment.

Optics

The beamline optics, schematically shown in Figure T1, is designed to provide a monochromatic x-ray photon beam in the energy interval 4-90 keV, with an energy resolution $\Delta E/E \approx 10^{-5}$-$10^{-4}$, a spot size from about 2.0×1.0 mm^2 to 0.2×0.2 mm^2 and a flux up to 10^9 -10^{11}ph/s.
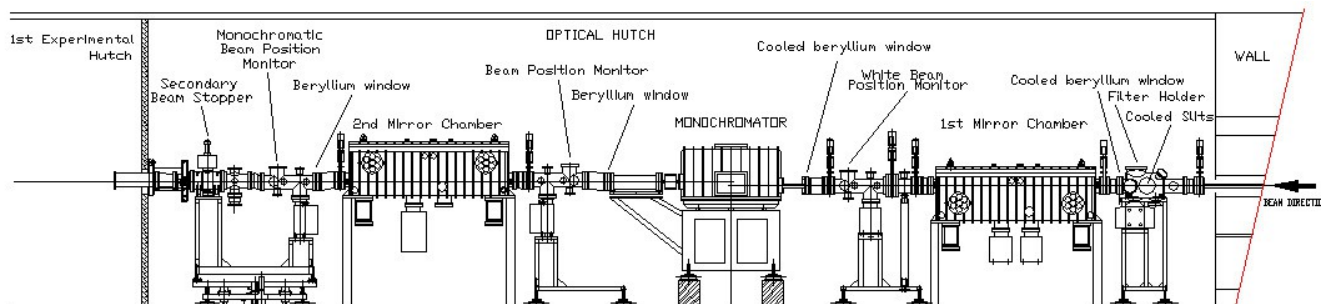
Figure T1: Layout of the optical hutch.

Two mirrors are used for vertical collimation (first mirror, fixed curvature radius of 16.5 km) and focusing (second mirror, variable radius), both coated with two stripes of Pd and Pt. The beamline works in three distinct optical configurations. At low energies (6-18 keV) the mirrors are placed to have the beam reflected by the Pd stripe and the glancing angle is set to 3.6 mrad ensuring a cut-off energy of 18 keV. At intermediate energy the mirrors are placed on the Pt stripe and the incidence angle is 2.7 mrad (E_{cutoff}=32 keV). At high energies (30-90 keV) the mirrors are taken out of the beam. For very low energies (<6 keV) a pair of Pt coated flat mirrors set to have a cut-off energy of 12 keV are used.

The monochromator is a double-crystal and double rotation axis device with fixed-exit. The second crystal is sagittally curved to focus the beam in the horizontal plane; dynamical focusing [Pascarelli-96] is used to keep beam dimensions in the focal point constant throughout a full energy scan and can be used in the whole energy range of the beamline.

Since the beginning, the nominal energy range was covered by mounting pairs of Si(111), Si(311) or Si(511) crystals. This operation was lengthy (because of the time needed to vent/pump the monochromator chamber and re-align both the monochromator crystals) and prevented us from carrying out measurements at absorption edges with very different energy values within the same experimental session. For this reason during the 2012 stop it was decided to realize the arrangement shown in Fig. T2.

4

Figure T2: Schematic view of the sagittally focussing monochromator operative at GILDA.
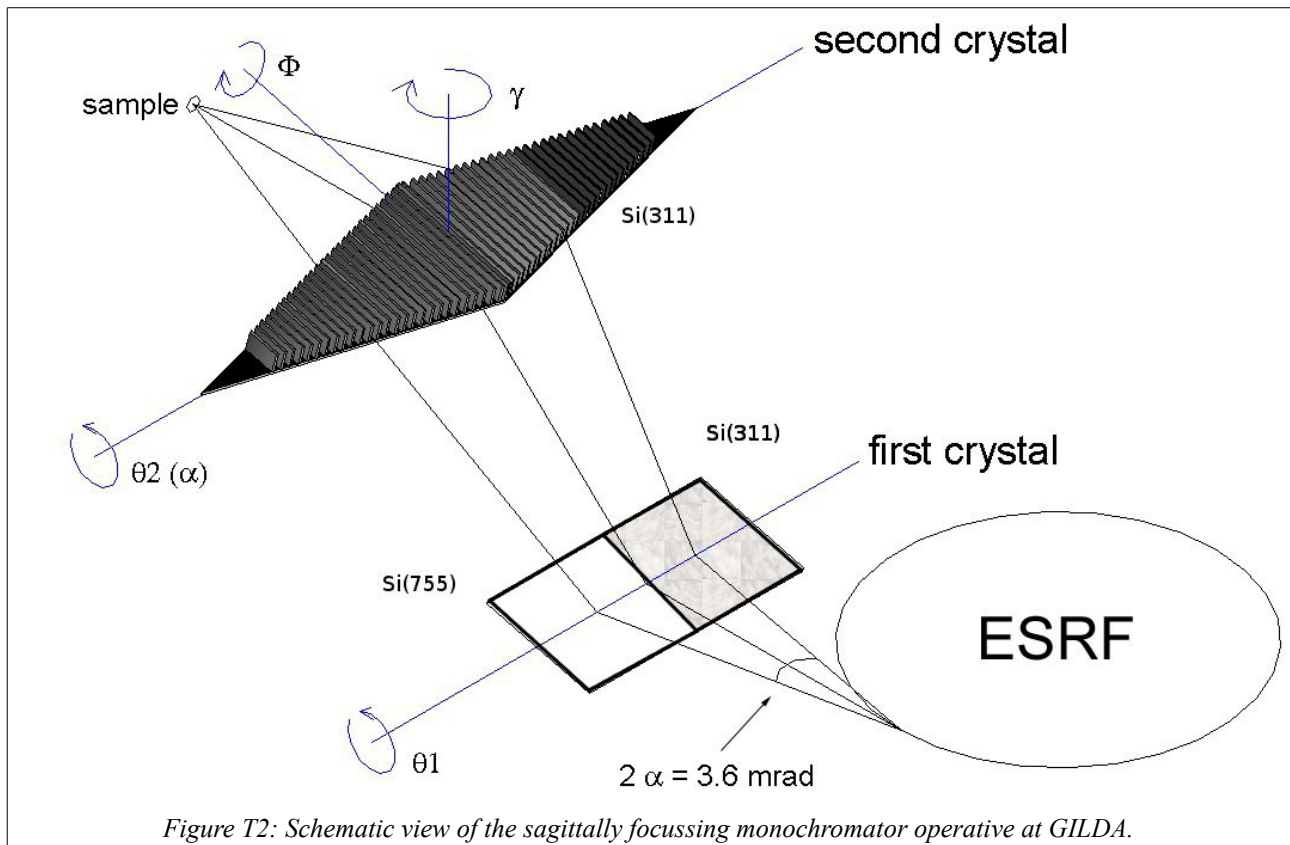
The first rotation axis holds two Si crystals, one cut following the (311) planes and the other along the (755) planes. The second crystal is Si(311) and the reflection of the beam coming from the (755) crystal happens through the (933) planes. Moving the horizontal primary slits one crystal pair can be selected and the accessible energy easily changed.

We have performed a number of tests to measure the flux and the signal to noise ratio achievable with this crystal mounting. The typical photon flux at the sample for standard ring current was in the 10^9 photons/s range allowing also measurements in fluorescence on diluted samples. In Figure T3 (left panel), we show the La K-edge absorption spectrum measured in fluorescence on a La doped (1%mol) silicate glass and the corresponding XAFS signal. Spectra with a very good signal to noise ratio were also collected in transmission mode (Fig. T3, right panel)
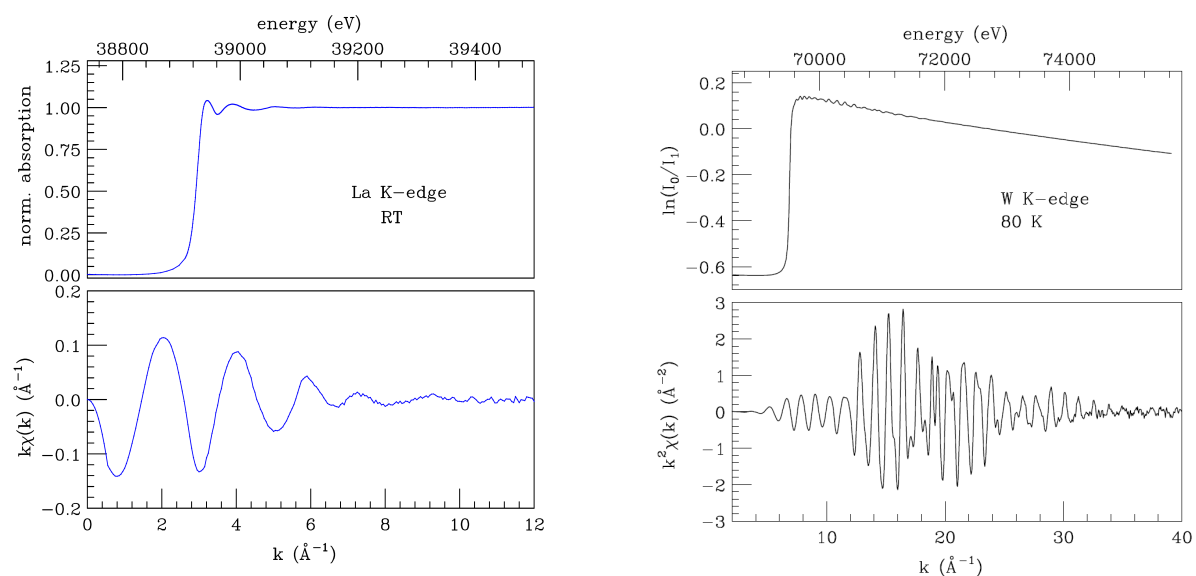
Figure T3: Example of spectra taken with the Si(755) crytal. (left) La K-edge XAS measured in fluorescence mode on a La doped (1%mol) silicate glass . Right: Tungsten K edge XAS spectrum and signal collected in transmission mode on a Tungsten foil at 80 K.

Usually an horizontal divergence of 1 mrad is collected and, when needed, the part of the crystal between two ribs (about 0.1-0.2 mrad hor) can be used to achieve a beam horizontal FWHM of about 200 μm.

A flat crystal operation mode is used for carrying out higher quality measurements in transmission mode. In this configuration the ribbed second crystal is left un-bent and only the crystal portion between two ribs is shined. In this way a noticeable improvement in the beam horizontal homogeneity has been achieved, that revealed to be crucial in the study of inhomogeneous samples (poorly ground powders, high absorbing matrices) requiring very low levels of noise ($<10^{-4}$). The considerable intensity loss (about one order of magnitude or more) is not critical since in the case of transmission mode data the noise is dominated by other sources than the statistical fluctuations.

The XAS end station

Standard data collection setup

The x-ray absorption spectroscopy (XAS) hutch has been conceived to carry out XAS experiments in different ways, ranging from concentrated to dilute samples (limit dilution 50 ppm

or 10^{14} at/cm^2) and from bulk to surfaces (limit thickness 0.2 ML). The conventional XAS apparatus consists in two experimental high vacuum chambers.
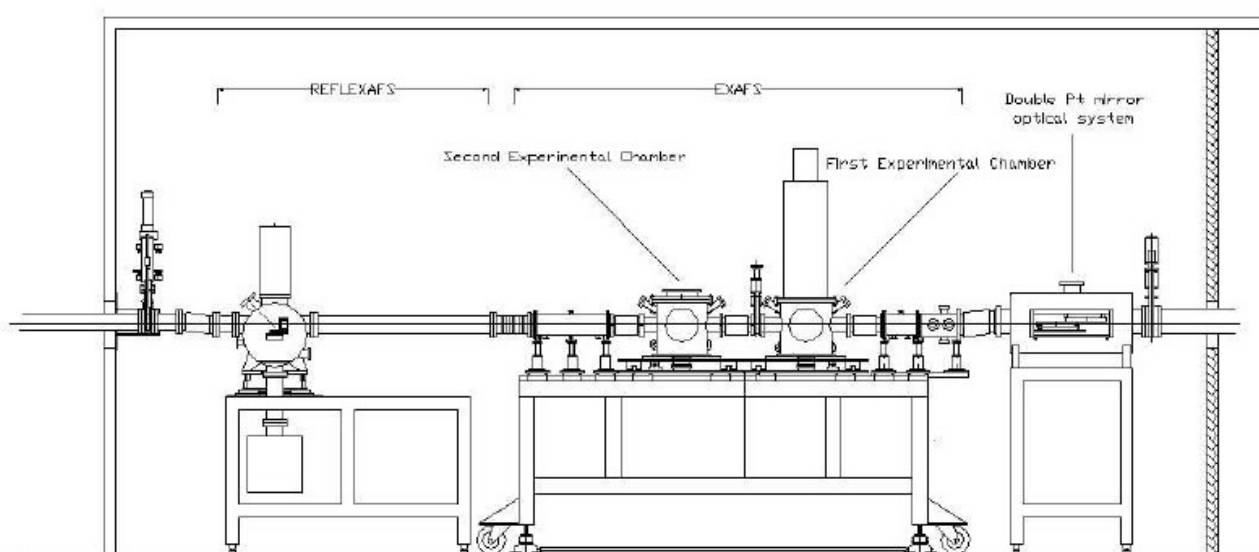

Figure T4: Layout of the EXAFS Hutch

The first chamber is used for standard experiments, while the second one is available for the installation of bulky/heavy cells from the users (Figure T4). Depending on the nature of the samples a number of different detectors are available at the beamline, namely:

1. Ion Chambers: two chambers are used for measurements in transmission mode. They can be filled with N_2, Ar or Kr gases to ensure an optimal efficiency in the whole energy range.

2. High Purity Ge multidetectors (13 and 12 elements arrays): these detectors are used for the collection of high quality fluorescence spectra with a typical energy resolution of 200 eV and maximum count rate of 100 kcps/element. A digital pulse processing permits a fast and reliable calibration of the device.

3. Electron detectors to perform measurements with surface sensitivity. In particular the measurement of the sample current or the detection of electrons amplified by a He chamber are available.

The recent acquisition of a further 12 elements HP-Ge array has improved the beamline capability of studying diluted samples and the possiblity of collecting data with both the arrays has been demonstrated.

XAS measurements can be carried out in a wide temperature range using a liquid He/N_2 cryostat (20-400 K). A translation/rotation stage mounted on top the liquid nitrogen cryostat allows the accurate positioning of the sample respect to the beam polarization direction, so permitting to

easily carry out "polarized EXAFS" experiments; the use of a vibrating sample holder helps in minimizing the effect of coherent scattering when analyzing single crystals.

A reaction cell for *in situ* studying solid samples in controlled atmosphere is also available with the possiblitiy of treatments in a temperature range from 100 to 700 K.

Surface XAS apparata

Total reflection and grazing incidence data collection modes represent a peculiar point of the XAS instrumentation available at GILDA. An *ad-hoc* experimental chamber is dedicated to total reflection EXAFS (ReflEXAFS) measurements for the investigation of surfaces or buried interfaces. The ReflEXAFS collection mode is based on the total external reflection of the probe beam by the sample surface. In this condition, the beam enters the sample only for a few nm (typically 5 to 10) realizing a surface sensitive technique without needing an Ultra High Vacuum environment. By slightly changing the incidence angle above the critical value the probed depth can be increased to a few μm so opening the possibility of carrying out depth sensitive investigations. The sample is oriented with the surface parallel to the polarization vector and the incidence angle can be adjusted within 0.001 deg. The vertical size of the incident beam is about 50 μm. The intensity of the "incoming" and "specularly reflected" beams is measured by ion chambers whereas the fluorescence signal can be collected using the multi-element high purity Ge detector. An Atomic Force Microscope working in contact mode (Model Molecular Imaging, PicoSPM) is also available to users for surface morphological characterization of the samples. The ReflEXAFS apparatus has permitted the realization of several studies on surface systems like those in [Bergamino-13, Bordiga-13, Naidu-13, Tougerti-12, Mohiddon-12a , Mohiddon-12b, Battocchio-11, Giubertoni-10]. In the recent years a new original procedure for the quantitative rigorous analysis of ReflEXAFS data has been developed [Benzi-2008] that gave rise to the CARD code [CARD-2012] freely available to users.

The main limitation on the use of ReflEXAFS technique is represented by the stringent conditions required on the samples in terms of length (a few cm), roughness and flatness, that could not be always satisfied in some cases. Therefore, an alternative data collection system for measurements in grazing incidence (φ ~1-2 degrees) mode inside the first EXAFS chamber has been developed. Both the calculation and the experimental data demonstrate that this setup, that combines grazing incidence and grazing collection geometry, is extremely advantageous when compared to the standard geometry used to perform XAS experiments in fluorescence mode,

allowing an enhancement in the fluorescence signal from the surface layer without a corresponding increase in the elastic scattering contribution from the matrix [Maurizio-2009].

Recent sample environment and Instrumentation developments

Cryostat for XAS measurements on frozen solutions

XAS experiments on biological samples are typically performed on frozen solutions in order to lower the thermal disorder and minimize the damage due to x-ray exposure. At this purpose, a liquid nitrogen bath cryostat has been recently commissioned and made available for experiments on frozen liquids. Samples are loaded through the top of the cryostat and cooled by nitrogen exchange gas. With respect to the standard cryostat hosting sample holders attached to a cold finger, the device has the advantage of not needing vacuum around the sample. Solutions are measured in plastic cells covered with glued Kapton windows, smaller and thinner than those designed to be used in vacuum and disposable to prevent cross contamination. The 'hold time' is more than 12 hours at 80 K, allowing a full set of measurements to be collected without refilling. Cooling down to 80 K is made in less than half an hour. The apparatus is compatible with both transmission and fluorescence detection modes. Two user experiments on diluted (~ 0.5 mM) protein samples have been successfully carried out up to now.

Figure T5: Picture of the cryostat for liquid samples

X-ray excited optical luminescence (XEOL) spectrometer

An apparatus for the collection of the optical emission from the sample following the x-ray excitation has been developed and successfully tested. The aim was to make available an additional XAS data collection mode that is capable to provide information on the luminescent regions of the sample. The apparatus consists in a collector bearing two lenses, one to collect light from the sample and the other for the focusing on an optical fibre. The system provides a moderate demagnification of a factor 1.6 in order to feed the entire image of the sample into the fibre. The lenses are made of BK7 glass and have a transparency range between 350 nm and 2000 nm. The collector is inserted in a vacuum chamber in order to allow measurements also at low temperature (liquid nitrogen). The optical signal is sent to the detector via an optical silica fibre passing through the vacuum environment.
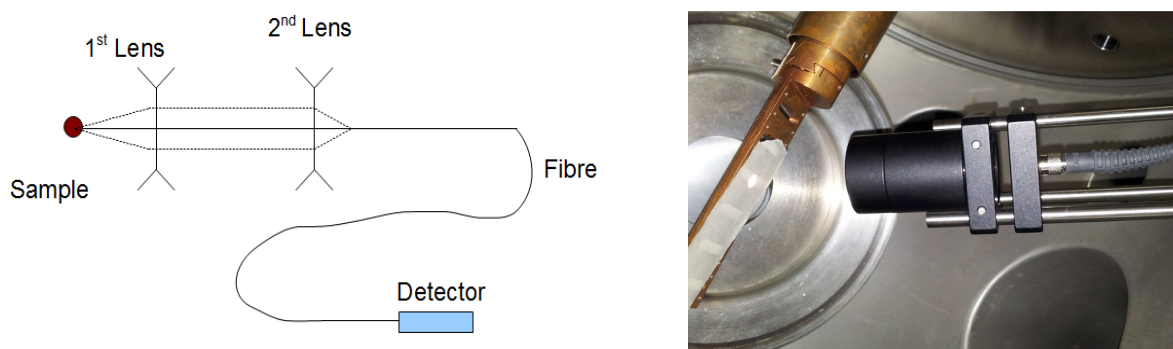
Figure T6: Sketch and picture of the XEOL apparatus.

The fibre is 10 m long and it can be drawn even outside the experimental hutch if needed. The detector can be either a Si-PIN photodiode for measurements in current mode or a Photo Multiplier Tube (PMT) for single photon counting. The Si-PIN photodiode (model Hamamatsu S-3584-08) is operative between 350 and 1100 nm whereas the PMT (Hamamatsu H-3164-10) is sensible between 300 and 650 nm. At present no monochromator is available but it is foreseen to achieve wavelength selection keeping a high luminosity by using bandpass filters. The installation of the filters is foreseen for year 2014.

Figure T7: EXAFS spectra of ZnO in transmission mode (blue), XEOL with the PMT detector (red) and XEOL with the SiPIN detector (green).

The readout of both detectors is easily implemented in the standard XAS data collection system of GILDA. XAS-XEOL data have b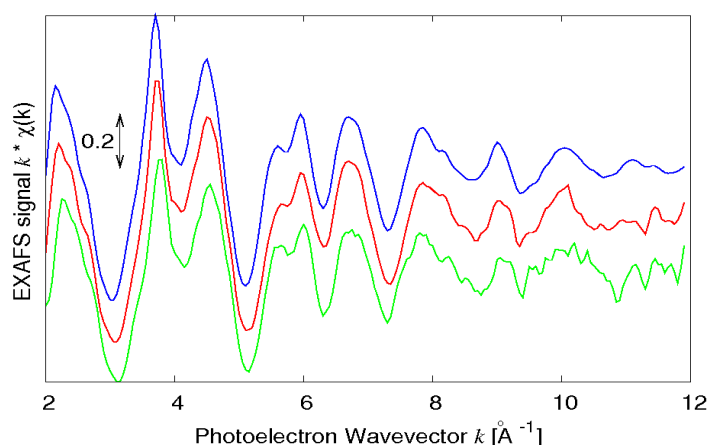een collected with this apparatus on model compounds like ZnO; further spectra have been collected on different luminescent systems namely Mn-doped GaN (Ga-K edge), (Ce,Tb)-doped $Y_2Si_2O_7$ (Y K-edge), Er-doped SiO_2 nanoparticles. The apparatus is thus operative and available for user experiments.

Time-resolved studies

The participation of GILDA in the FEL-PIK project named EX-PRO-REL (EXcitation PROcesses and RELaxation in condensed matter and nanostructures) lead to the development of new capabilities for the beamline in the field of time-resolved studies. In particular, our goal was the realization of pump and probe experiments exploiting the 16-bunch and 4-bunch filling modes of the ESRF storage ring. In these two timing modes, x-ray pulses of about 100 ps duration are available with a spacing of 176 and 704 ns respectively. If combined with a pump signal at the same frequency and fixed time lag with the x-rays, a stroboscopic data collection can be realized without needing the use of fast detectors. A first class of experiments was aimed to study structural deformation of (piezo/ferro)-electric materials like Lead Zirconium Titanate (PZT) under fast electrical excitation. Small capacitors (dimensions 300 μm × 800 μm) consisting in 100nm-thick PZT were investigated with a sub-mm x-ray beam (200 μm × 200 μm, Figs. T8a and T8b) while applying intense electric field pulses (200 kV/mm, duration 200ns). The pulse generator was

especially realized for the project by the CNR-Istituto Officina dei Materiali electronics laboratory in Trieste.
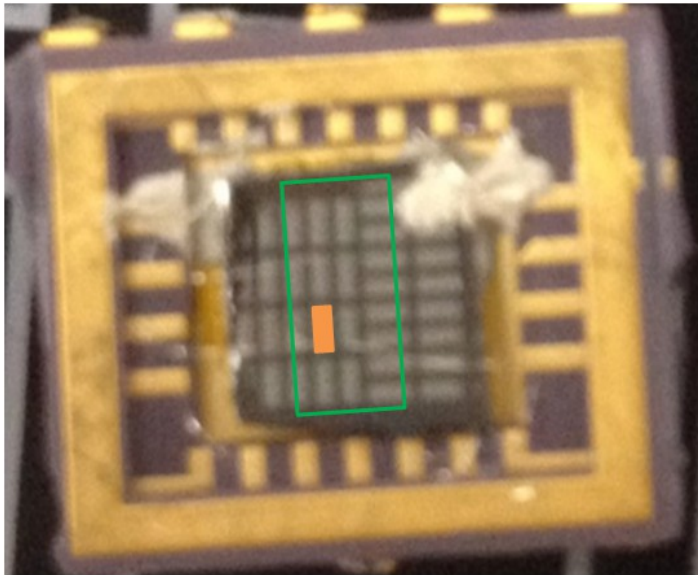

Figure T8a: (left) picture of an array of PZT capacitors. The area mapped with x-ray fluorescence (green square) and the wired capacitor measured with x-rays (orange rectangle) are shown.
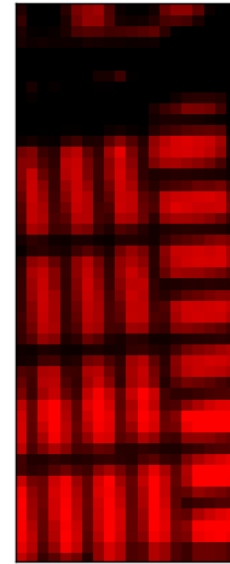
Figure T8b: x-ray fluorescence map (Pt L_α line) of the array of PZT capacitors.

Some problems encountered with samples are presently being addressed in order to complete this experiment, but the capability of data collection in stroboscopic mode has been fully demonstrated. As an evolution of the technique, we plan to use it for light excitation with high power Light Emitting Diodes (LED) in the UV range, in 2014. A collaboration with the CNR-IEIIT institute has been signed with the aim of developing highly performing drivers (high current, low rise time, ..) for this class of experiments.

Two-Dimentional Fluorescence imaging

We have recently carried out 2D x-ray fluorescence imaging pilot experiments for the characterization of cm-sized zones of heterogeneous samples for which the extreme spatial resolution values achieved with micro/nano beams are not needed. The x-ray spot of GILDA of about 200 μm×200 μm allows the collection of fluorescence maps on large areas. Data collection can be carried out at characteristic energy values around the absorption edge of an element (pre-edge peaks, inflection point, …) in order to enhance the contribution from a a particular valence state or site symmetry of the absorber. This technique can be applied to academic studies (physics, materials science, environment, cultural heritage) as well as to industrial characterization (reservoir

rocks, composite materials) and presents the advantage that elements even at considerable dilution levels (hundreds of ppm) can be studied.

Fig. T9 presents the preliminary results from a test experiment carried out on a fragment of ancient ceramics containing Cu (coming from 'Museo Regionale della Ceramica di Deruta', courtesy of Prof. B. Brunetti, Univ. Perugia).
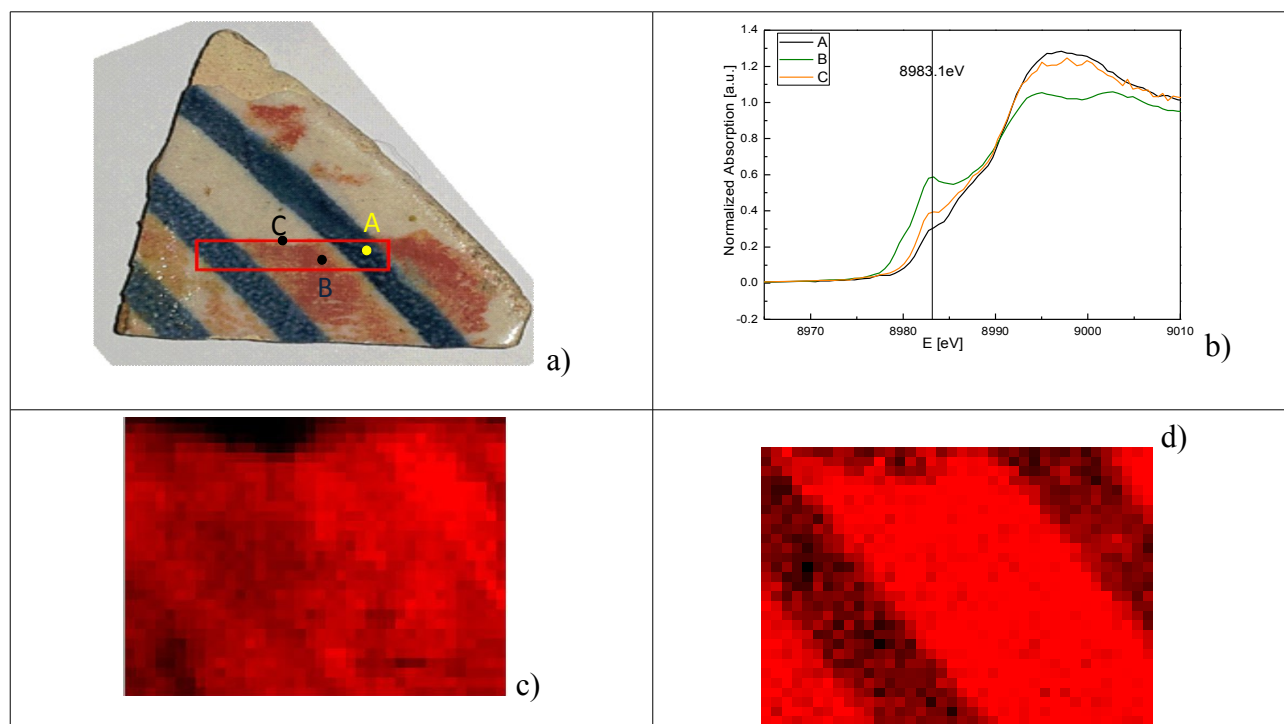
Figure T9: Example of Valence State mapping applied to an ancient ceramic fragment. a) Optical image of the fragment, the dimensions are about 3 cm × 2 cm ; b) XANES spectra taken in different points of the manufact; c) elemental map relative to Cu, d) valence state map collected at 8983 eV enhancing mostly the distribution of Cu^+ ions

Panel a) presents the optical image of the ceramic fragment with the X-ray probed zone marked as a red rectangle. In points A), B) and C) Cu-K edge XANES spectra were collected (panel b)) in order to select the best energy point for the subsequent image collection (in this case 8983 eV, at a resonance typically encountered in Cu^+ glasses). Images c) and d) were obtained after background subtraction and normalization. Image c) (collected well above the edge) contains information on the distribution of elemental Cu which appears to be quite uniform. Conversely, image d), collected at 8983 eV enhances the zones with higher content of Cu^+. The blue bands appear to contain Cu but predominantly in a Cu^{2+} oxidation state.

The x-ray diffraction (XRD) end-station

In year 2010 the x-ray powder diffraction (XRD) setup based on translating image plates (IP) read by an external IP reader has been upgraded to host a MAR-345 image plate detector, on

short-term loan from the ESRF Instrument Pool. A fast shutter controlled by the acquisition software (under SPEC) was also installed to allow precise control of the exposure time. The typical focused beam size at the sample is 200 μm x 200 μm (FWHM). The sample to detector distance and the incident beam wavelength can be tuned to match the experimental requirements in terms of angular resolution and accessible portion of the reciprocal space. The collection of a full pattern in the minutes timescale is now possible and opens large opportunities for time-resolved *in-situ* studies of structural transformations induced by temperature and/or chemical reactions. The available sample environment includes a hot air blower working up to 1200 K (also controlled by SPEC) and a reaction chamber for in-situ catalysis studies. An x-ray fluorescence detector (Si PIN photodiode) has been also mounted to collect both XRD patterns and XAS spectra (even from dilute phases) from a sample within a capillary under the same thermodynamic and chemical conditions. The XRD activity has been interrupted in 2012 due to lack of staff.

The third experimental hutch was conceived for users wishing to install their own apparata on the beamline. At present, an apparatus dedicated to EXAFS in Ultra High Vacuum conditions is mounted. The instrument is not operative at present.

Beamline control

A series of interventions on the beamline control systems has been carried out aiming to a long-term use of the instrument. Obsolete control systems with no perspective of maintenance (beamline and experimental chamber vacuum, stepping motors, detectors) have been changed with new ones using standard ESRF equipment. This, also fulfills some of the recommendations of the previous review panel (namely, moving to SPEC). During the stop in 2012 a huge transition to SPEC has been carried out regarding both the stepping motor controls and the data acquisition system. Motors are now driven by the standard ICEPAP drivers controlled under SPEC and the data from detectors (both ion chambers and multi element Ge detectors) are implemented under SPEC and standard ESRF TANGO device servers. This has permitted to control most of the optical elements via SPEC macros adding new capabilities of control. Namely, it is now possible to switch between different beamline configurations (Pd mirrors, Pt mirrors, no mirrors, Si(311) or Si(755) crystals) in a considerably shorter time than previously achievable (about 2hrs against 1 day). Added to the novel configuration of the monocromator crystals GILDA can now access the entire energy range (6-90 keV) without critical mechanical interventions, allowing users to perform experiments at different absorption edges in a single experimental session. Added to that,

new data acquisition schemes have become possible profiting of the standard ESRF routines like the collection of fluorescence maps on the samples (Fig. T9) for their characterization or selection of a particular zone of interest (Fig. T8b). This has required a considerable coding work aimed to the modification of the Labview User interface to cope with the new SPEC data acquisition system. The monochromator control remained under the old software due to the considerable complexity of the intervention not justified in the perspective of a replacement of this device.

Also the vacuum control for the optical hutch and the experimental chambers has been modified and now is based on a standard ESRF PLC computer and WAGOBOXES.

All these interventions fulfill the recommendations of the previous Review Panel (May 2009) and pose the bases for a long-term operation of the beamline even in a refurbished configuration.

GILDA Beamline

Administrative aspects

Organisation

GILDA is a Collaborative Research Group (CRG) at the ESRF. This means that 70% of the beamtime is made available for research groups from Italian institutions. The remaining 30% of the beam time, according to ESRF regulations, is made available to general ESRF users. The current CRG contract covers the period January 1st, 2010 to December 31st, 2014. Consiglio Nazionale delle Ricerche (CNR) and Istituto Nazionale di Fisica Nucleare (INFN) are the legal contracting parties to the ESRF and the formal representatives of GILDA to the ESRF are Francesco d'Acapito and Settimio Mobilio. The recurrent budget is managed by both CNR (2/3) and INFN (1/3).

Resident staff is entirely appointed by CNR through a local section (Operative Group in Grenoble, OGG) of the Istituto Officina dei Materiali (IOM). Beam time proposals submitted for the CRG beamtime (70% of the total available beamtime) are selected by referees jointly appointed by the two funding institutes. CRG beamtime is made available to Italian users on a scientific-evaluation basis and it is not proportional to the financial contributions from the funding bodies. There is no differentiation between scientific/technical user support for international ESRF and CRG users but CRG users do not receive financial support to cover travel/accommodation expenses.

Beamline Staff Situation

The staff in Grenoble maintains, operates and develops the beamline and provides user support in the broadest sense. This ranges from maintaining scientific contacts with the existing user community, establishing contacts with potential new user groups, investigate technical improvements, design and initiate new experiments, discuss the scientific issues with the users, help and train users in data analysis. Each of the scientific staff members is involved in research activities as well. This both via the in-house research program but as well as via collaborations with user groups. The resident scientific and technical staff running the beamline in the period 2009-2013, as well as their areas of interest/competences is listed below:

Francesco d'Acapito

- Role: Co-Responsible, local coordinator of the beamline activities
- Position: CNR-IOM-OGG, Permanent researcher
- Period of activity: whole contract
- Scientific interests: point defects in insulators and semiconductors, methods and instrumentation, cultural heritage and environment.

Chiara Maurizio

- Role: Beamline scientist
- Position: CNR-IOM-OGG, Permanent researcher
- Period of activity: till October 2010
- Scientific interests: Materials for optoelectronics, materials for energy storage, methods and instrumentation

Angela Trapananti

- Role: Beamline scientist
- Position: CNR-IOM-OGG, Permanent researcher
- Period of activity: January 2010 - present
- Scientific interests: Liquids and disordered systems at extreme conditions, earth science, methods and instrumentation.

Hernan Pais

- Role: Beamline Technician

- Position: CNR-IOM-OGG, fixed term technician

- Period of activity: January 2008 - January 2009

- Competences: Mechanics.

Antonello Rizzo

- Role: Beamline Operation Manager

- Position: CNR-IOM-OGG, fixed term technician

- Period of Activity: March 2011 - April 2012

- Competences: Beamline control hardware and software.

Simona Torrengo

- Role: Post-doctoral Researcher

- Position: CNR-IOM-OGG, fixed term post doc

- Period of activity: February 2013 - present

- Scientific interests: imaging, rare earth doped glasses.

Figures S1 and S2 illustrate the staff availability (person months) and the staff turnover within the period 2009-2013:

Staff at GILDA
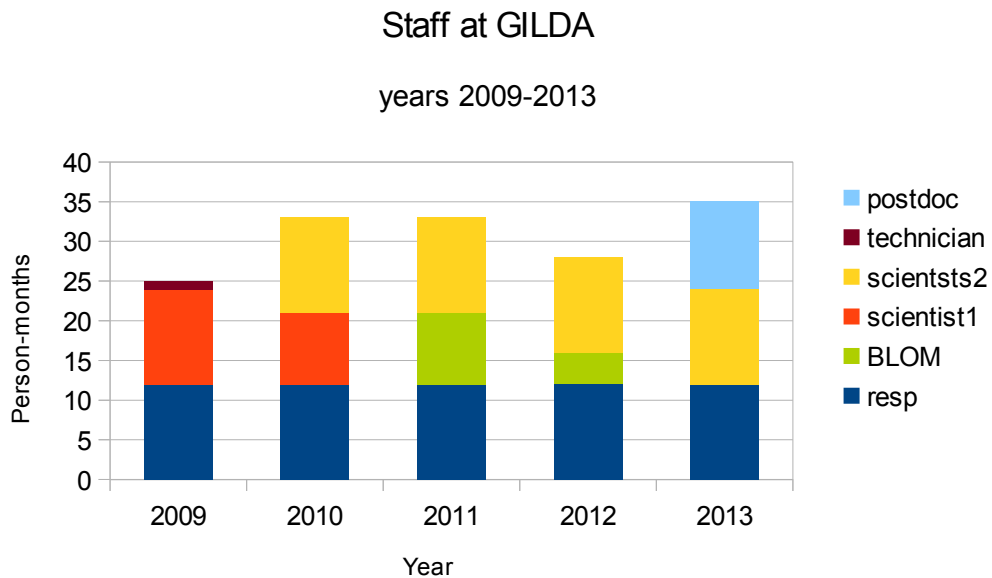
years 2009-2013

Figure S1: Evolution of the resident staff at GILDA in the years 2009-2013. Note that the minimum required by the contract with ESRF is 36 resident person months/year
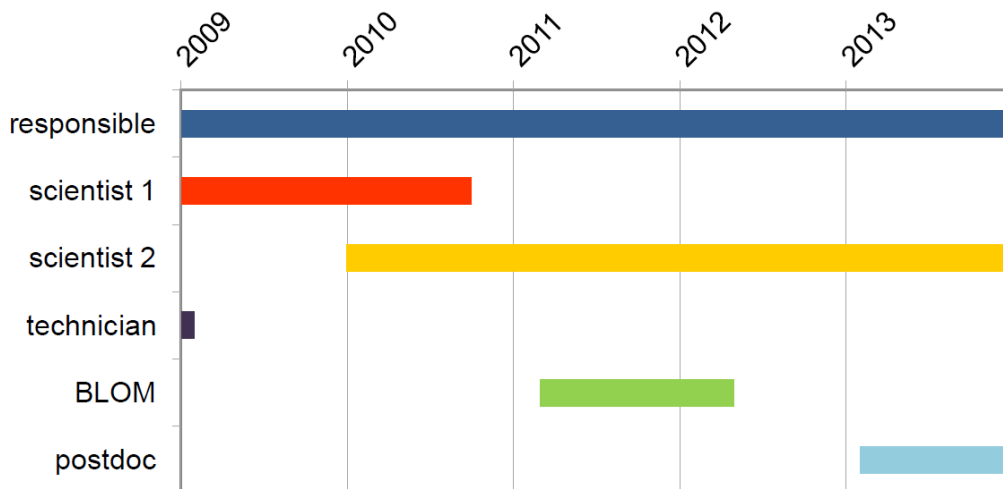
Figure S2: Coverage of the various professional profile positions for the GILDA resident staff.

In addition to these persons, other non-resident collaborators have tightly worked with the GILDA staff:

Settimio Mobilio

- Role: Co-Responsible, chairman of the Beamtime Selection Panel (till Oct 2011).

- Position: Permanent Full Professor, Università Roma Tre
- Period of activity: whole contract period
- Scientific interests: Materials with high electronic correlations, multiferroics, methods and instrumentation

Vinicio Tullio

- Role: Technician
- Position: Permanent technician, INFN-LNF
- Competences: electricity
- Period of activity: 2-3 weeks/year.

Andrea Martin

- Role: Technician
- Position: Permanent technician CNR-IOM
- Competences: electronics
- Period of activity: occasional urgent interventions (< 1 week/year)

The number of staff persons has been exceedingly low during the present period and in some cases this has severely affected the operation of the instrument. We have been asking to the financing institutes the increase of the resident staff but up to now without an effective answer.

Statistical data on Users and scientific production

GILDA has provided beamtime to a wide variety of scientific communities with particular predominance of physicists and chemists. In the years 2009-2013 it has been reported an increased use from scientists from new communities like environment, cultural heritage, applied materials science. The figure below shows the repartition of the total number of experiments between the principal communities:
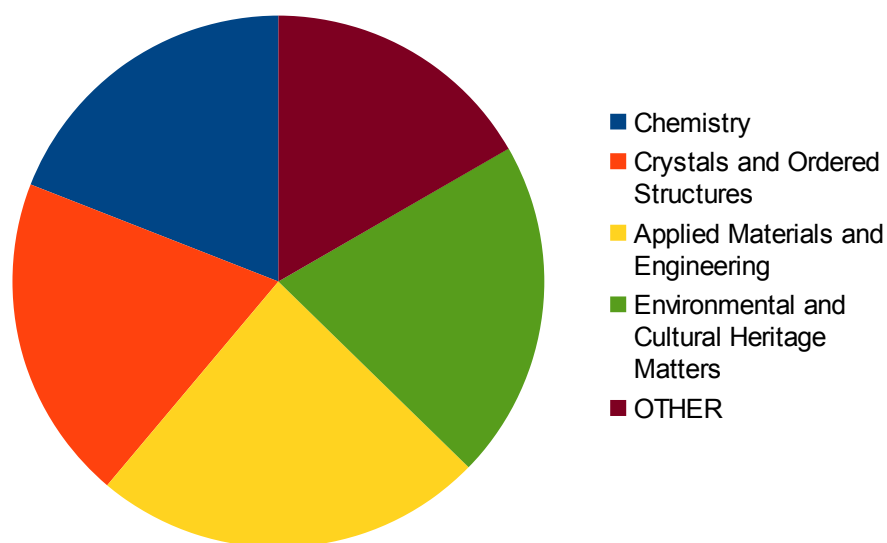
Figure SD1: Distribution of the number of experiments among the main fields of activity.

The activity of GILDA can be divided in four main topics roughly involving 20% each of the experiments: 'chemistry', 'hard condensed matter', 'applied materials science' and 'environment and cultural heritage'. Other activities (Surface science, soft matter, life science) add up to a further 20%. Concerning the nationalities of affiliation of the experiment proposers the following figure collects the data:
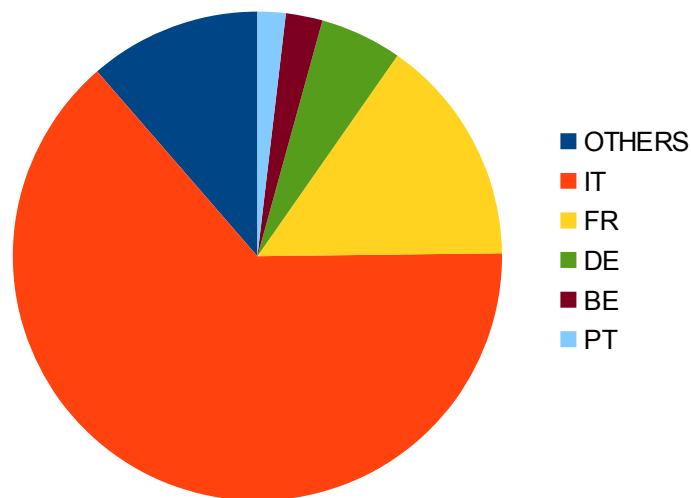
Figure SD2: Distribution of the number of experiments at GILDA by nationality of affiliation of proposers.

The Italian scientific community is the dominant one followed by French users.

The relation between research involving the beamline staff and that carried out by the external users is resumed below:
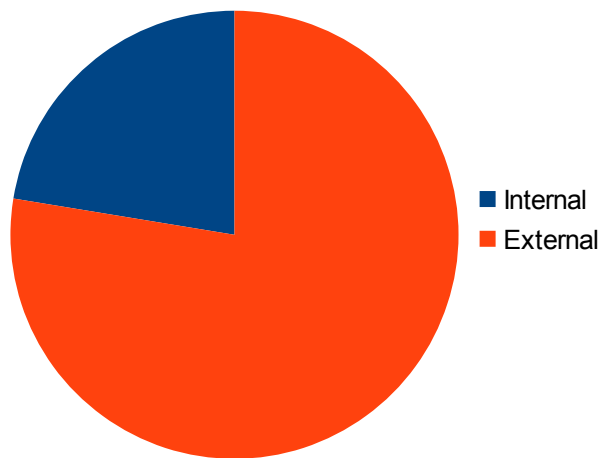
Figure SD3: Division of the total number of publications for the years 2009-2013 between those involving the GILDA staff (blue) and those carried out by the external users (orange).

In total, slightly less than 25% of the total production involves the local staff.

The number of publications related to experiments carried out at GILDA in the years 2009-2013 are shown below:
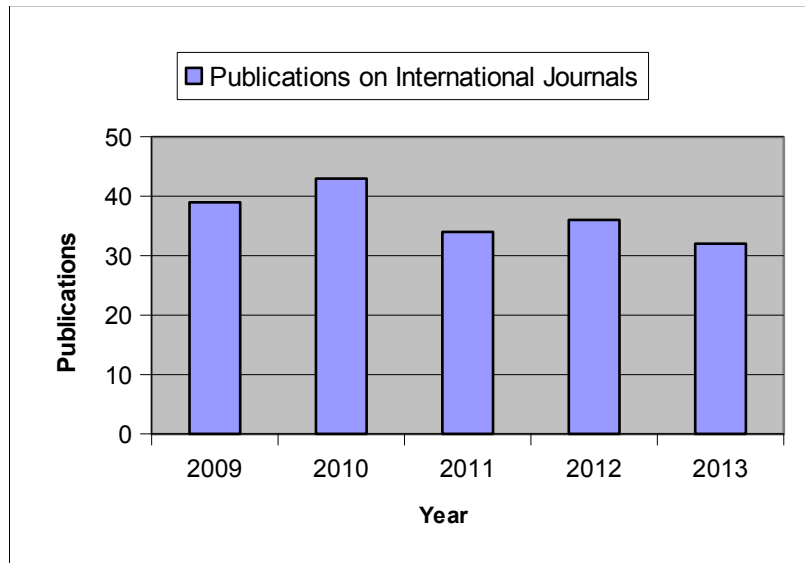
Figure SD4: Number of publications on international journals in the years 2009-2013 related to experiments carried out at GILDA (source ESRF library database).

The quality of the research carried out at GILDA can be derived from the distribution of the Impact Factors (IF) of the journals having published these works:
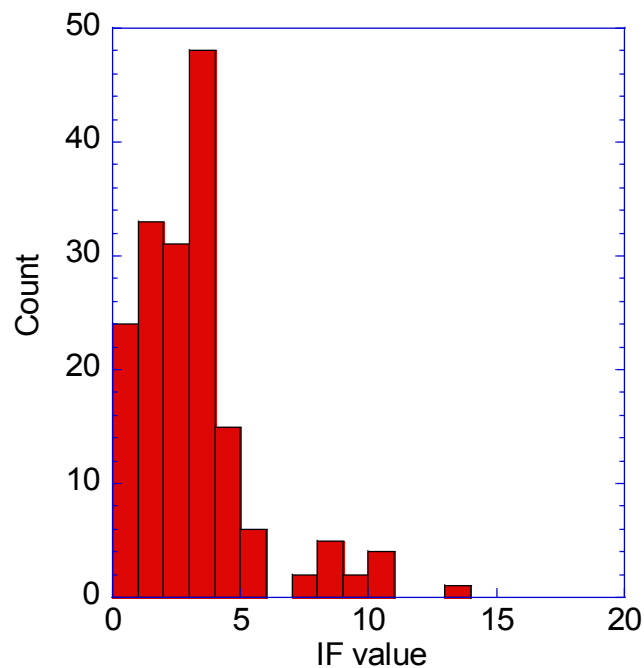
Figure SD5: Distribution of the IF of the journals having published articles related to experiments carried out at GILDA in the years 2009-2013.

The maximum of the distribution is around value IF=3 and a peak around 8 can be noticed as well. The number of experiments carried out at the beamline are shown here:

GILDA Beamline
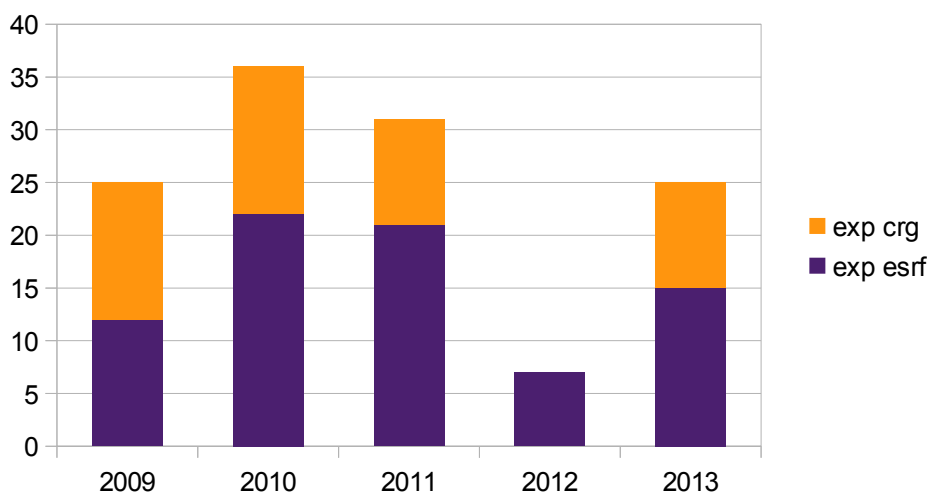
Figure SD6: Number of experiments for ESRF and CRG communities in the years 2009-2013.

The number of experiments carried out has been strongly influenced by the severe staff restriction experienced in year 2012 that has led the beamline direction to suspend the CRG call of period 2012-II and to report the already accepted experiments to the following period. Nonetheless GILDA has remained a highly demanded beamline as shown in the figure below:
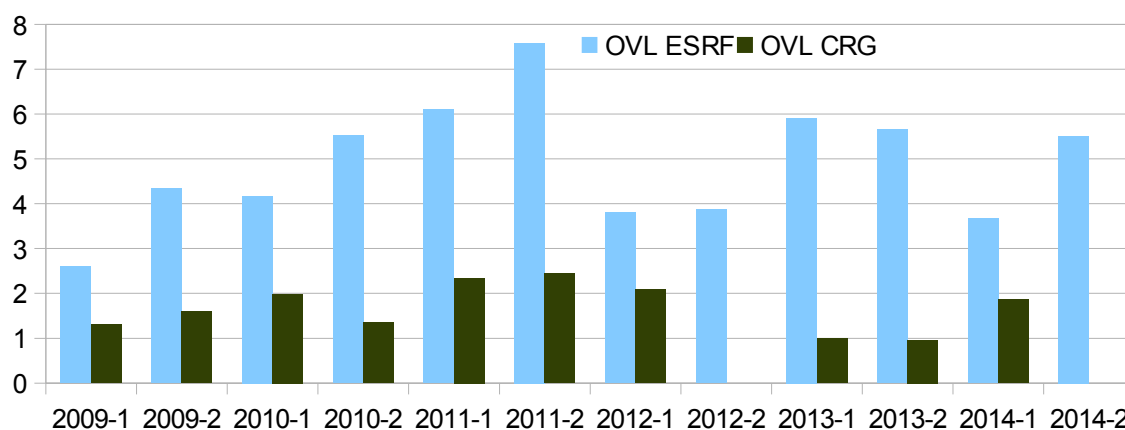
Figure SD7: Overload of the GILDA beamtime divided between the ESRF (cyan) and CRG (green) quotas. The requested shifts are relative to all experiments submitted to GILDA for which a positive feasibility was stated.

The beamline has a high overload for on the ESRF beamtime quota that drops on the CRG side. This can be only partially explained by the larger fraction (2/3) of beamtime available for national users. Another reason is the fact that in the period shown here no financial support has been provided to users on the CRG beamtime by the Italian funding agencies and several groups have decided not to apply due to *in-house* budget restrictions.

Future perspectives and plans for upgrade

Aim of the project

After many years of continuous operation a deep rethinking of the scientific targets of the beamline as well as a renewal of the instrumentation is needed, in order to maintain the beamline performance at the state-of-the-art, improve its reliability and to keep it at the leading edge among the other similar beamlines at the ESRF as well as in the world. It is worth noting that in the last years ESRF has undergone a robust refurbishment plan of its beamlines and an even deeper renewal plan is foreseen for the storage ring in a near future.

As a matter of fact, in the past two decades relevant technological advances in the field of X-ray optics (mirror and monochromator) have been achieved and a modification of the beamline optics components will allow to improve the beam quality (size, stability and homogeneity) fully exploiting the extreme brilliance of the present ESRF X-ray beam and that of the future machine planned for the next years [ESRF white book]. At present, the reliability of some components, in particular of the monochromator, is becoming a critical issue and such aspects have been also underlined by the last ESRF Review Committee (2009). In the upgraded version proposed in this document, the limitations of the present layout (beam inhomogeneity, poor temporal stability) will be overcome and new experimental possibilities will be made available to users. This will make GILDA a unique tool for the advanced analysis of materials in a variety of fields like Environmental Science, Materials Science, Biophysics, Chemistry, Earth Science and Cultural Heritage.

It is worth to remind that GILDA is a unique instrument for the Italian and international community because it makes available to users an intense photon flux in a high energy range (> 20 keV) that is only obtainable at the ESRF. The peculiar experimental aspects of the refurbished beamline, that will make GILDA a top-level instrument, are exposed below:

- use of grazing incidence/total reflection data collection in linear dichroic mode for surface analysis;
- high sensitivity for the analysis of diluted samples;
- high quality in terms of low noise and linearity for XAS data in transmission mode up to 90 keV;
- combined multitechnique *in situ* data collection for extreme conditions or in operando experiments;

To achieve these targets a particular attention will be devoted to the quality of the beam spot in terms of homogeneity, spatial and energy stability, reduced size and divergence.

Design

Basic Concepts

To carry out the outlined research programs, the beamline has to fulfill the following requirements:

- to provide an intense beam also at high energies (E > 20 KeV) building an instrument complementary to those operative on the national sources. This will permit the structural analysis (using XAS at the K absorption edge) of technologically crucial materials like catalysts (containing Mo, Pd), hydrogen reservoirs (Nb, Pd), protonic conductors (In, Ba, Ce, Zr), solar cells and transparent conductors (In, Sn), luminescent and advanced magnetic materials (Rare Earths).

- To realize experiments in Grazing Incidence / Total reflection and linear dichroic mode. This detection mode will greatly benefit from the increased brilliance of the future source and it will permit the structural analysis of thin films, interfaces or the interaction between adsorbed species and model surfaces, with increased data quality and lower detection limits.

- To provide an intense and sub-mm beam in the whole energy range. This is needed for the analysis of diluted materials, for the studies under (moderate) extreme conditions of high temperature or pressure, for pump-probe experiments with electric field or light excitation and for elemental/chemical state surface mapping.

- Provide an homogeneous and stable beam in non-focusing mode to be used in high-quality and low-noise transmission XAS studies as well as for possible X-ray Imaging experiments (Mapping, Radiography).

Preliminary Technical design

The layout of the beamline is shown in Fig. FP1 and will consist in 3 cabins: an optical hutch (OH) and two experimental hutches (EH1 and EH2).
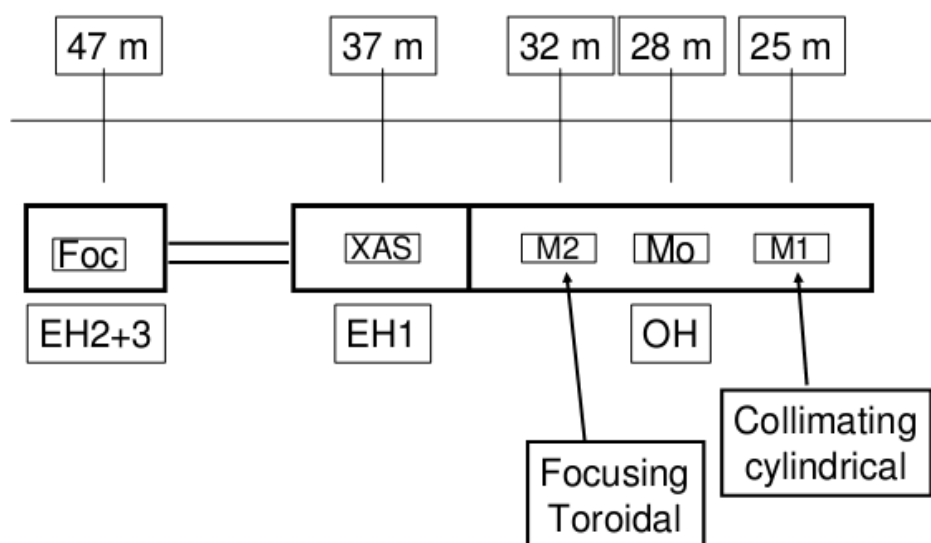
Figure FP1: layout of the new beamline.

The Optical Hutch will contain the optical elements that will focus the beam in the middle of the second experimental hutch EH2. Here, there will be the main experimental setup consisting in two stations, one with a vacuum chamber (containing a manipulator for standard measurements and one for RefIEXAFS experiments) while the other will be an open station permitting the mounting of bulky sample environments and detection systems. The two set-ups will be mounted on a long marble bench and will have the possibility of translating along the beam path to place the sample on the focal spot.

The preceding hutch (Experimental Hutch 1, EH1) will be used for experiments with a non focused beam like EXAFS in transmission mode and low noise conditions or radiography.

X-ray source

At the beginning of its operation the beamline will take the beam from the high field part (0.85 T) of the BM8 bending magnet of ESRF. In this point the X-ray source has dimensions 75 μm (H) and 32 μm (V) FWHM. The source is located at 25 m from the first optical element. The realization of the new lattice of ESRF [ESRF white book] foreseen in operation for late year 2019 will provide the beamline with a 3 pole wiggler source with smaller dimensions (13 $\times$ 4 μm), and intensity increased by a factor 3.

Mirrors

Keeping the constraint of a beamline with high flux, focusing is a major issue for the present project. To meet the requirements stated in the scientific case it is necessary to have at the same time high brilliance, flux and beam homogeneity that are difficult to fulfill at the same time. On other energy scanning XAS beamlines different optical schemes have been adopted to focus the beam. In some cases sagittal focusing has been chosen (FAME at ESRF [Proux-05], SAMBA [Belin-05] and DIFFABS [DIFFABS] at SOLEIL). Sagittal focusing, although providing exceptionally intense beams in a wide energy range, is not suited for our goals as it introduces severe beam inhomogeneities in the horizontal plane. Good results have been obtained from non-focusing designs (BM29 at ESRF [Filipponi-00], XAFS beamline at ELETTRA [Dicicco-09]). This technical solution would however restrict the application field of the beamline to concentrated samples that is too limiting for the scientific case presented here. In more recent projects a great interest for toroidal mirrors has emerged driven by the achromaticity of this element and the strong improvement of the quality of these devices in the latest years. This is the case of protein crystallography on bending magnet beamlines at APS [Mcdowell-04], B18 at DIAMOND [Dent-09], the ROBL beamline at ESRF [Scheinhost-09], the CLAESS beamline at ALBA [CLAESS]. This choice will be adopted for the present project as it ensures at the same time a high intensity and homogeneous beam of reduced size.

The first mirror will have cylindrical shape and be used for collimating the beam as it allows lowering the vertical divergence of the beam from ~40 µrad (determined by the input slits) to the limit of the mirror slope error (currently achievable: a few µrad). As the scattering vector of the monochromator is vertical, this device permits to achieve an instrumental energy resolution well below (less than 25%) the core-hole width of the K edges in the energy range of interest. This will make an optimized configuration for the collection of XANES data at high energy resolution. The first mirror will have 3 stripes: Pt, Pd and Si for an efficient harmonic rejection in the whole energy range.

The second mirror will have a toroidal shape and will focus the beam in a 2:1 condition on the horizontal plane. It will consist in a cylindrical channel cut in a bendable silicon substrate. This choice has been shown to minimize the impact of chromatic aberrations in the focal spot [Mcdowell-04] and will keep at a moderate value the overall length of the beamline. The limited horizontal acceptance of the device (1mrad in this case) is largely compensated by the high quality of the beam achievable in this way. Considered the space available it will be possible to have 2 toroidal channels on the same substrate. The part between the channels section of the second mirror

will be left flat to make available to users a non focused beam. The technical solution consisting in 2 channels realized in the same substrate is not particularly risky and has been successfully used in other projects ([CLAESS], [Dent-09], [Scheinhost-09]). The two channels will be coated one with Pt and the other with Pd, the flat region between the channels will be used for applications needing unfocused beam.

Both mirrors will work at 2 mrad incidence angle. A pair of Pt-coated plane mirrors (already present on the beamline) working at 10mrad will be used to reject harmonics in the lowest part of the energy range.

Monochromator

The monochromator will be a commercial fixed-exit device with a single rotation axis and equipped with thick flat crystals. The cooling will be based on water but the possibility of switching to Liquid Nitrogen cooling will be left open by a suitable design of the instrument. Different pairs of crystals (Si(311) and Si(111)) will be mounted to access the whole energy range of about 5-80 keV. The crystals will be permanently mounted inside the monochromator and the change will be realized by simple horizontal translation of the instrument. This solution will ensure a high quality beam in terms of temporal stability and beam spatial homogeneity thanks to the use of flat reflectors. Depending on the details of the design (in particular, the maximum and minimum Bragg angle achievable) the operation energy range of the various crystals could be modified.

Ray Tracing

A detailed Ray-Tracing calculation of the parameters of the beamline has been carried out using the SHADOW code [Lai-86] and with the present parameters of the ESRF storage ring. The proposed beamline scheme is shown to provide a high photon flux in a wide energy range and a small beam size in compliance with the experimental requirements cited in the previous sections

INTERNAL LIMITS

--GOOD ONLY

INTENS = 18.80
TOT = 15000
LOST = 10742

Horizontal: 1: X [user unit]
Vertical: 3: Z [user unit]

HistoHorizFWHM: 101.033

HistoVertFWHM: 152.429
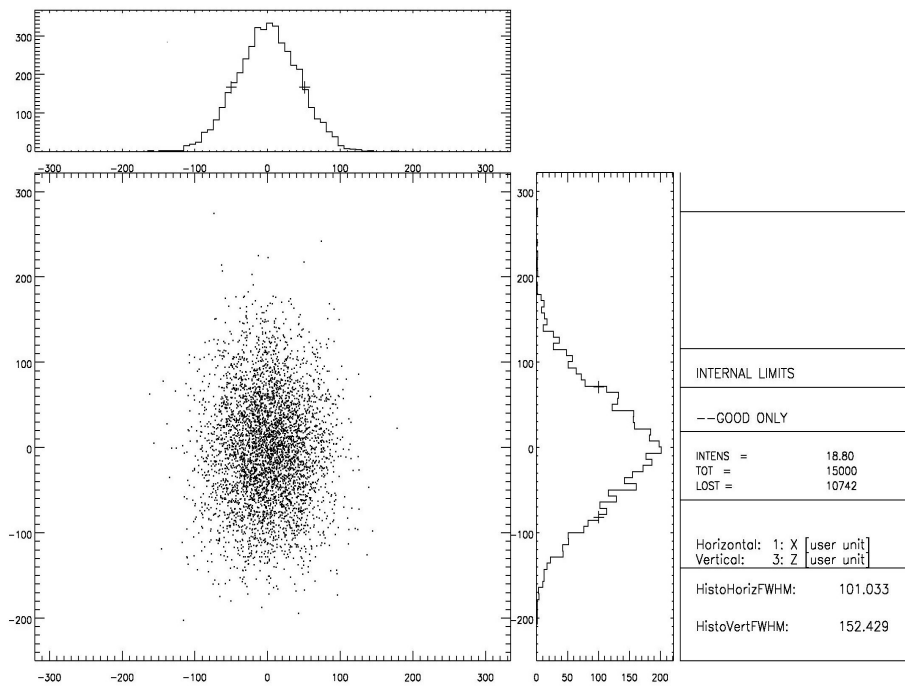
Figure FP2: Simulation of the focal spot carried out with the SHADOW code.
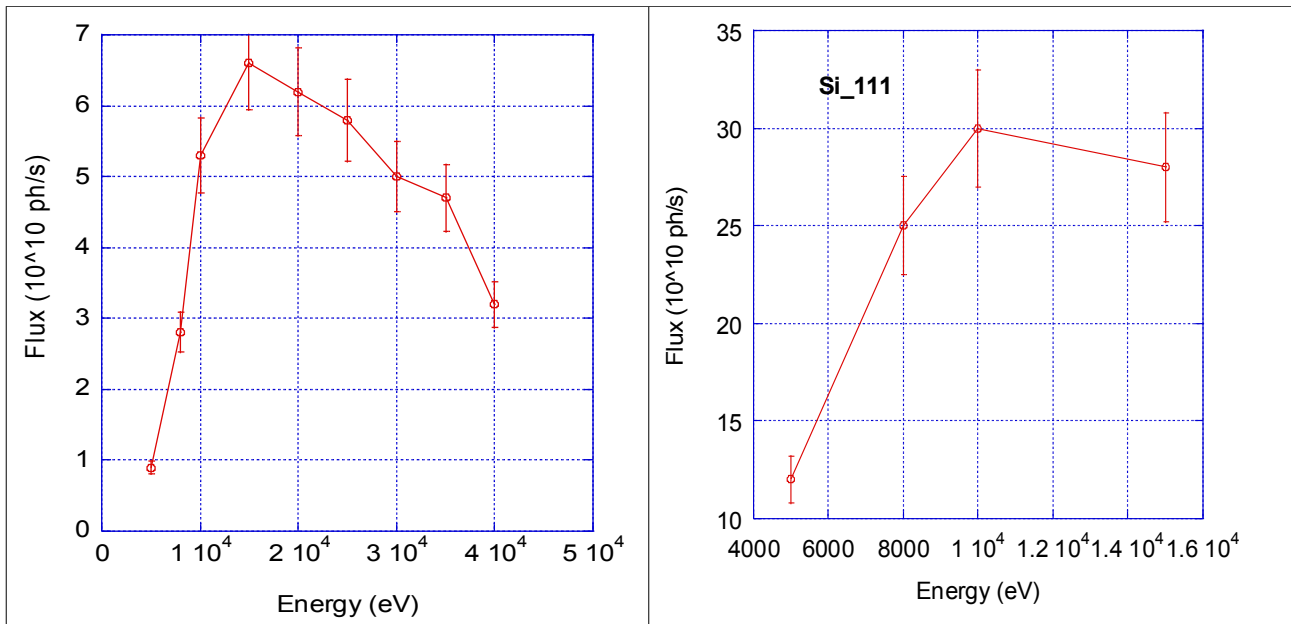
Figure FP3: Estimated flux on the sample for the new optical layout. ESRF running at 200mA, primary slits at 23m, 1mm vert, 23mm hor.

Endstations

The beamline will have 2 experimental stations: the main one, using the focused beam, will be placed in the EH2 . The main station in EH2 will be a long marble bench carrying 2 experimental stations and supports for the ion chambers, one measuring the incoming beam (I0) and the others

reading beam transmitted through the sample (I1) and a reference system (IR). The first experimental stations will carry a vacuum chamber containing two manipulators: one for standard XAS experiments in fluorescence mode and the other for ReflEXAFS experiments. Sideways, a Be window will permit the X-ray arrival to the Fluorescence detector. The second station will be a table with basic translation/rotation stages. This will be used to mount bulky experimental setups and multitechnique detection systems. A new multielement Ge detector will be a key point of the beamline. It will be a 25 elements device with an almost doubled sensitive surface respect to the previous detector and will increase dramatically the capability of investigating diluted samples.

In EH1 there will be an apparatus for the collection of conventional XAS spectra in transmission mode. It will consist in a bench hosting two experimental chambers and ion chambers for the detection of the beam before and after the sample. Used in conjunction to a non-focusing configuration of the beamline it will realize a station for high quality XAS data collection.

The ancillary equipment will include a liquid helium/nitrogen cryostat, a cell for chemical gas-solid reactions and a cell for measurements at high temperature. For the control of the optical elements and instruments in OH and EHs the standard ESRF hardware and software will be used with a consequent ease of operation for users.

Timetable

The refurbishment of the beamline will be carried out in a preliminary design phase and two realization phases in a gradual process aiming to minimize the impact on the user community. The fact of re-using a considerable portion of existing material (lead cabins, slits and attenuators, beam monitors) will permit an effective limitation of the total cost.

- *Preliminary Phase: 0 - +1yr.* During this time the total amount of resources available (capital and personnel) for the project will be defined and the executive plans will be produced. The supply companies will be selected and they will start the production of the items needed for phase I.

- P*hase I: +1yr - +2 yr.* During this phase the beamline infrastructures will be adapted to the new layout (creation of a single EH2, positioning of the beam pipes at the correct height, cabling and piping in EH2) and the new optic elements will be installed, namely the monochromator and the mirrors. The present ReflEXAFS chamber and one of the actual XAS chambers will be moved in the new EH2 for the first experiments and beam characterization. The companies for the production of items of phase II will be selected and

will start the production. After the commissioning, and while waiting the results of the calls for tender for the remaining items, the beamline will be open to users. An investment for about 700 K€ in capital is foreseen for this phase.

- *Phase II: +2yr - +2.5 yr* In the phase II the new experimental station in EH2 will be installed (replacing the old ReflEXAFS chamber) and new fluorescence detector and the related control electronics will be installed. A final commissioning process will be carried out before opening to users. An investment for about 670 K€ in capital is foreseen for this phase.

Contacts with the Italian funding agencies are in progress in order to make available the necessary funds and to define the availability of peak load staff.

Activity Report 2009-2013

Overview of the overall scientific activity

Selection of five publications

1. Bracco S., Comotti A., Ferretti L., Sozzani P. *Supramolecular Aggregation of Block Copolymers in the Solid State As Assisted by the Selective Formation of Inclusion Crystals* Journal of the American Chemical Society **133** 8982-8994 (2011).

2. Chakraborty S., Bardelli F., Charlet L. *Reactivities of Fe(II) on calcite: Selenium reduction* Environmental Science and Technology **44** 1288-1294 (2010).

3. Cianchetta I., Colantoni I., Talarico F., d'Acapito F., Trapananti A., Maurizio C., Fantacci S., Davoli I. *Discoloration of the smalt pigment: Experimental studies and ab initio calculations* Journal of Analytical Atomic Spectrometry **27** 1941-1948 (2012).

4. Devillers T., Rovezzi M., Gonzalez Szwacki N., Dobkowska S., Stefanowicz W., Sztenkiel D., Grois A., Suffczynski J., Navarro-Quezada A., Faina B., Li T., Glatzel P., d'Acapito F., Jakiela R., Sawicki M., Majewski J.A., Dietl T., Bonanni A. *Manipulating Mn-Mg$_k$ cation complexes to control the charge- and spin-state of Mn in GaN* Scientific Reports **2** 722-1-722-6 (2012).

5. Bortolus M., Bisaglia M., Zoleo A., Fittipaldi M., Benfatto M., Bubacco L., Maniero A.L. *Structural characterization of a high affinity mononuclear site in the copper(II)-a-synuclein complex* Journal of the American Chemical Society **132** 18057-18066 (2010).

Highlights of the scientific activity

Local order in semiconductors
F. Boscherini, Univ. Bologna

Introduction

One of the most useful characteristics of XAFS is the possibility of determining the local structure of dilute atoms, with sensitivity to both atomic and electronic structure. Consequently, applications to study dopants and complexes due to their incorporation in host semiconductors have been widespread. Thanks to the state of the art instrumentation developed on the GILDA beamline, including the sagittal focusing monochromator [Pascarelli-96], multi element hyper pure Ge detectors and associated electronics [Ciatto-04], and various flexible and optimized sample holders and geometries (such as the grazing incidence set-up [Dacapito-03, Maurizio-09] and the vibrating sample holder [Tullio-01]), this area of investigation has been very active. Some of the results have been (or will be) illustrated in review papers [Boscherini-12, Boscherini-14, Dacapito-14, Boscherini-15]; XAFS data analysis now increasingly relies on sophisticated *ab-initio* methods, which have often been used in investigations on semiconductors performed at GILDA [Dacapito-11].

Dilute Magnetic Semiconductors (including semiconductor nanostructures)

A dilute magnetic semiconductor (DMS) consists of a non-magnetic semiconductor doped with a few % of a magnetic ion (a transition metal, e.g. Mn or Fe). DMS thin films are typically obtained by MBE growth on an appropriate substrate. In an ideal DMS the ions occupy substitutional sites in the semiconductor lattice and retain ferromagnetic alignment in the presence of spin polarized free carriers. DMSs have been intensely studied in recent years since they are the basic building bloc of spintronic devices. Doping of both bulk and nanostructured semiconductors has been studied.

Research carried out at GILDA has given an important contribution to this field since high quality XAFS measurements at the transition metal's edges are a key tool to correlate local structure, oxidation state and physical properties.

Mn and Fe in GaN

XAFS on GILDA has made a significant contribution for the characterization of Mn and Fe -doped GaN films; it should be remarked that the nitrides are a more defective materials system

than more traditional III-V semiconductors and that continuous evolution is occurring as the close interplay between growth and characterization leads to improved materials. XAFS has provided important results on the site of Mn and Fe in GaN and their oxidation state.

The complexity of the Mn-doped GaN materials system, the strong connection between atomic structure and physical properties and the role of XAFS is very well illustrated by studies [Stefanowicz-10, Bonanni-08] on samples grown by metal organic vapor phase epitaxy (MOVPE). By combining various structural probes, including the key role of XAFS measurements performed at GILDA, it was possible to show that in this system Mn is always substitutional (up to 1% Mn), is homogeneously distributed and that no precipitates are present. Correlation with magnetic measurements demonstrated that the interaction between the Mn ions changes from ferromagnetic to antiferromagnetic when Mn is reduced from Mn^{3+} to Mn^{2+}.

Co-doping of Mn:GaN with Mg can have the effect of modifying the charge state of Mn. This interesting possibility was studied by Devillers *et al.* [Devilliers-12] by combining synchrotron techniques with magnetic, optical and *ab-initio* DFT studies. Mn K edge XAFS at GILDA and non resonant K_{β} X-ray Emission Spectroscopy on ID26 showed that codoping of GaN:Mn with Mg allows to control the Mn^{n+} charge and spin state in the range $3 \leq n \leq 5$ and $2 \geq S \geq 1$. This outstanding degree of tunability arises from the formation of hitherto concealed cation complexes $Mn-Mg_k$, where the number of ligands k is pre-defined by fabrication conditions; these complexes are illustrated in Fig. SMC1. The properties of these complexes allow to extend towards the infrared the already remarkable optical capabilities of nitrides.
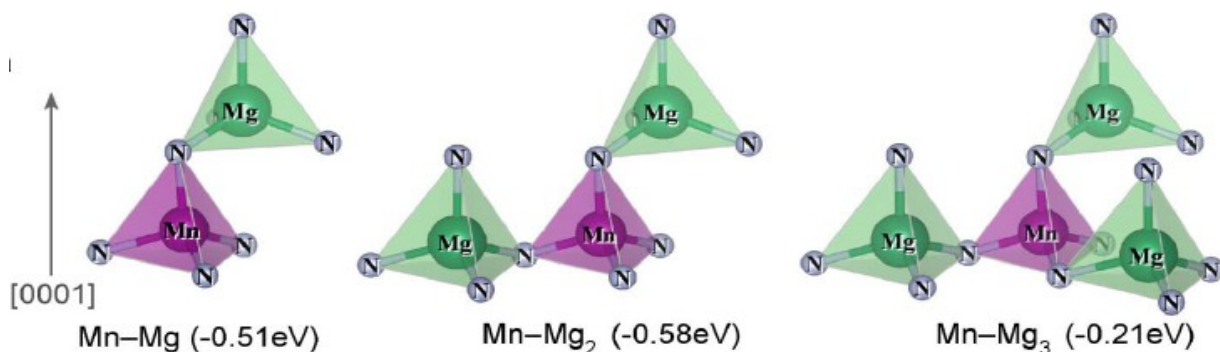

Figure SMC1: Most stable $Mn-Mg_k$ complexes (k = 1-3) and their pairing energies computed by DFT relative to the $Mn-Mg_{k-1}$ complex. From ref. [Devilliers-12].

The same group have also studied in depth Fe-doped GaN samples grown by MOVPE [Bonanni-08, Rovezzi-09, Navarro-10]. With the important contribution of XAFS they have shown

that Fe-containing precipitates (Fe nitrides and also α-Fe nanocrystals) are often formed but that their formation can be hampered by Si co-doping. Magnetism in this system is thus significantly affected by "embedded magnetic phases". In Fig. SMC2 we report data which nicely illustrates the fact that these XAFS measurements provided at the same time information on the local structure and on the charge state of the probed atom. FTs relative to samples deposited without and with Si co-doping, respectively, are reported on the left and center panels, respectively; in the former, a clear peak (labeled R_2) develops at high Fe concentration, indicative of Fe–Fe atomic correlations, while in the latter this peak is absent. In the right panel the corresponding pre-edge and near edge spectral regions are reported. In the sample without Si co-doping the pre-edge structure exhibits a single peak, indicating that Fe is present only in the Fe^{3+} charge state; in the sample with co-doping a low energy pre-edge component is apparent, indicating the presence of Fe^{2+}.
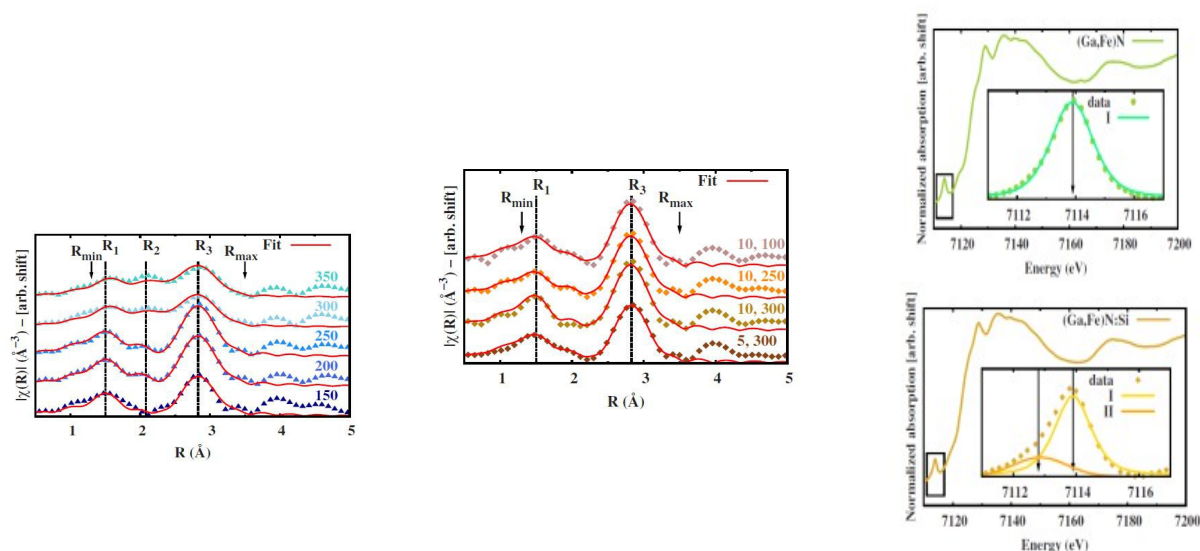
Figure SMC2: Left panel: FT of Fe K-edge XAFS spectra for Fe-doped GaN samples grown without Si co-doping; the Fe concentration increases from bottom to top. Central panel: corresponding spectra for samples grown with Si co-doping. Right panel: Fe K-edge spectra in the pre-edge and near edge regions for Fe-doped GaN without (top) and with (bottom) Si co-doping. The insets highlights the pre-edge peak and reports the fitting with one and two components, respectively. Reprinted from ref. [Rovezzi-09a, Rovezzi-09b] and [Bonanni-08].

Mn in III-V nanowires

Mn doping of III-V nanowires (NWs) has been studied by Mn K-edge XAFS. The growth of InAs NWs [Jabeen-10] was obtained by solid source MBE using Mn droplets on either SiO_2 or GaAs. The incorporation of Mn in the NW, which is in principle desirable in the substitutional form

in order to create a true DMS NW, was instead found to be mainly in a hexagonal MnAs phase. The same group reported [Dacapito-12] growth of Mn-doped GaAs NW using both Mn droplet catalyst or using the more traditional Au droplet catalyst and supplying Mn during the growth. For the Mn catalyzed growth the authors again found incorporation in a disordered MnAs phase, while for Au catalyzed NW Mn is mainly found in a Mn-Au intermetallic phase. These two contributions illustrate the complexity of these materials systems and the precious information which can be gained from XAFS on GILDA.

Mn in group IV semiconductors and their nanostructures

The achievement of ferromagnetism in Ge by introduction of a magnetic transition metal has recently attracted considerable attention due to the expected full compatibility with the mainstream silicon technology. It is hoped that such an approach would allow to finely control polarized currents and will assure both semiconducting behaviour and magnetic ordering. However, due to the very low solubility limit of Mn in Ge (10^{15} cm^{-3}), growth of homogeneous phases of diluted alloys is challenging. The magnetic response of most of the Mn_xGe_{1-x} alloys fabricated so far is probably due to Mn-rich precipitated phases.

One of the more puzzling findings about MnGe was the observation of nanocolumnar structures in epilayers of Mn-Ge alloys grown on Ge [Jamet-06]. A first study conducted by Mn-K edge XAS [Rovezzi-08] revealed a markedly disordered environment around Mn with several shells involved under the main coordination peak and realizing an environment reminiscent of that of Mn2 in the Mn_3Ge_5 structure. However the picture of the 'isolated defect' was questioned in a following article [Arras-12] where it was shown that clustering of Mn is particular structures (a cubic α-$MnGe_2$ phase, isostructural with α-$FeSi_2$) would lead to an energetically favoured scenario. XAS has been applied to this problem with the help from Molecular Dynamics based on Density Functional Theory (MD-DFT) [Arras-12]. Indeed, by simulating the XAS spectra from a model of nanocolumn α-$MnGe_2$ only 2nm in diameter and embedded in Ge through the average of a suitable number of MD-DFT frames, it has been shown that the experimental data could be suitably reproduced (Fig. SMC3).

In this context, Gunnella *et al.* [Gunnella-10] have used Mn K-edge XAFS to study the incorporation of Mn in Ge fabricated by either ion implantation or MBE, at various growth temperatures (from 80 to about 623 K) and few per cent concentrations. They found that when the growth temperature exceeds 330 K, the MBE samples show a high number of precipitated

ferromagnetic nanoparticles, mainly Mn_5Ge_3, nucleated from the previous occupation of interstitial tetrahedral sites. Efficient substitution is observed in the case of MBE samples made by alternate layers of GeMn alloys grown at 433 K and undoped Ge thick layers. Similar good dilution properties are obtained by implanting Mn ions at low temperatures (80 K). In a related paper, Ottaviano *et al.*, [Ottaviano-11] showed that a 2×10^{16} Mn+/cm^2 100 keV ion implantation at liquid-nitrogen temperature onto Ge(100) surfaces produces perfect Mn dilution into a completely amorphized Ge layer (155 nm thickness and 4% average Mn concentration). SQUID investigations demonstrate ferromagnetism up to room temperature. First-principles calculations on Mn-doped amorphous Ge give a rationale to the experiments at the lowest fluence showing that disorder in the amorphous phase with the distortion of the Ge tetrahedra plays a crucial role, favoring inclusion of substitutional Mn and, correspondingly, enhancing the magnetic response of the system.
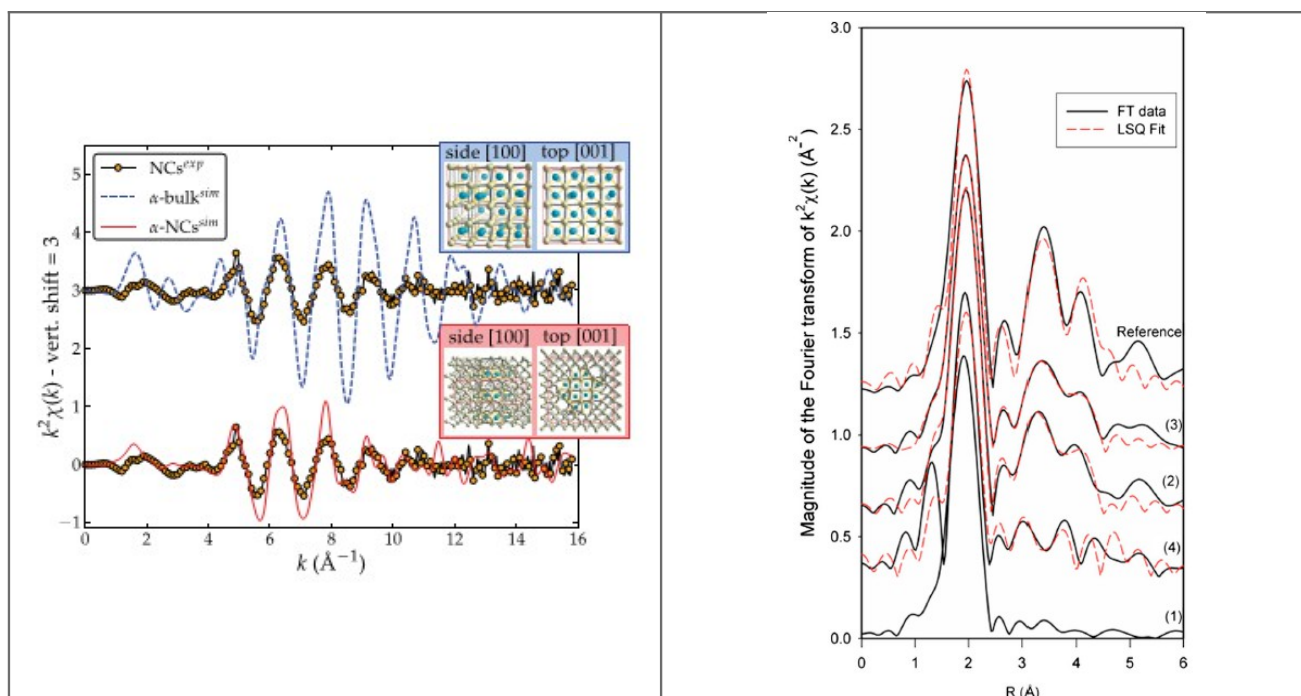
Figure SMC3: Comparison between experimental data (dots) and theoretical MD-DFT simulations (lines) for bulk (upper panel) and nanocolumn (lower panel) forms of α-MnGe$_2$. The disorder introduced by the column boundary permits to explain the low amplitude of the signal. [Arras-12]

Figure SMC4: Magnitudes of the Fourier Transforms of As K-edge EXAFS for As USJ in Si. The various traces are described in the text. [Giubertoni-08].

Group-IV semiconductor nanowires and nanodots are of particular interest for integration into future nanoscale device structures, as they are compatible with existing complementary metal-oxidesemiconductor (CMOS) technologies. Single crystalline Ge and Si nanowires have recently

been synthesized and utilized in various charge-based nanowire devices. However, operational nanowire spin-state devices such as spin gain transistors and spin injection devices have not yet been demonstrated. Theoretical predictions show that such devices can be realized by employing dilute magnetic semiconductors as these materials combine the complementary functionalities of ferromagnetic and semiconductor materials.

Van der Meulen *et al.* [Meulen-09] adapted a wet deposition method, using sputtered gold nanoparticles supported on porous alumina membranes as catalytic seeds for growth, to produce single crystalline $Ge_{1-x}Mn_x$ nanowires; samples had Mn concentration equal to 0.5-1.0 atomic % and displayed ferromagnetism above 300 K. Mn K-edge XAFS measurements demonstrated that Mn atoms are incorporated into the Ge lattice at substitutional sites. Using MBE co-deposition of Si and Ge on Si(100)-2×1, self-assembled Mn-doped $Si_{0.3}Ge_{0.7}$ nanodots on Si(100) were prepared by molecular beam epitaxy by De Padova *et al.*, [Depadova-12]; samples exhibited ferromagnetic behaviour with a Curie temperature of about 225 K. Mn XAFS demonstrated the presence of $Mn_5Ge_1Si_2$ crystallites, thus clarifying the structural origin of the ferromagnetic response.

Other DMS systems

We briefly describe other high quality work performed at GILDA in the field of DMS.

1)   Cu doped ZnO was studied by Vachhani *et al.* [Vachhani-12]. Polycrystalline pellets were synthesized with Cu concentrations varying from 2 to 10 wt% by a solid state reaction route. Magnetization measurements coupled to XMCD showed that all the samples were paramagnetic with an antiferromagnetic interaction between magnetic moments. Cu edge XAS demonstrated that at low Cu content most of the Cu atoms substitute for Zn inside the wurtzite lattice, while for higher Cu concentrations some unreacted CuO remains segregated from the $Zn_{1-x}Cu_xO$ solid solution.

2) Mn/Si_3N_4 multilayers prepared by sputtering and exhibiting room temperature ferromagnetism have been studied by Céspedes *et al.*, [Cespedes-09]. In order to find the most suitable conditions to stabilize the ferromagnetic ordering in this system, the evolution of the magnetic properties has been studied for films in which the Si_3N_4 layer thickness was maintained constant while that of the Mn layer was varied. Structural, compositional, electronic and magnetic characterizations have been performed by means of a variety of probes. Mn edge XAFS provided key information on the charge state of the Mn ions (XANES) and the local atomic structure (EXAFS). The authors found that the peculiar

magnetic behavior of these films is mainly related to the stabilization of a slightly distorted Mn_3N_2 phase that is induced by the Si_3N_4 at the interfaces.

3)   MnP nanostructures embedded in GaP epilayers and MnP polycrystalline films, grown from the vapor phase on GaP(001) substrates using metalorganic precursors have been studied by de Andrés *et al*. [Deandres-11]. The samples exhibit a large increase of the Neel temperature compared to the bulk. XAFS shows that epilayers and films contain MnP grains in the nanometric range with average Mn–P bond lengths very close to those of bulk MnP. The authors conclude that the differences in the magnetic behavior are most probably originated by local structural disorder at the surface of the nanostructures and by finite size effect.

Ultra Shallow Junctions

In the continuing trend toward miniaturization of microelectronic components a crucial recent issue has been to determine the best processing method for the fabrication of ultra shallow junctions (USJs) in Si; USJs are regions with greater than equilibrium dopant concentrations confined to the top 10–20 nm of the Si wafer and which are required to have the sharpest possible concentration profile. USJ are fabricated by very low (a few keV) ion implantation coupled to various annealing treatments. XAFS has been able to elucidate the connection between the local structure of As and B dopants and their physical properties.

Arsenic USJs have been studied by fluorescence detected grazing incidence XAFS in similar studies performed by d'Acapito *et al*. [Dacapito-07] and by Giubertoni *et al*. [Giubertoni-08]. The two studies will be shortly described separately and a brief common conclusion presented.

•   The first group [Dacapito-07] studied a set of samples deposited at 5 keV (estimated projected range 8 nm) at a fluence of 1×10^{15} atoms/cm^2 and subjected to various rapid thermal annealing processes. Variation of the grazing angle allowed varying the probe depth from 6 to 300 nm. Interpretation of XAFS data was aided by *ab-initio* structural simulations of the equilibrium structure of substitutional As (As_{Si}) and vacancy-As complexes involving from one to four As atoms (v-As_n). They detected the presence of mostly As_{Si} accompanied to various amounts of v-As_n, the relative fractions changing with distance from the surface; a considerable degree of structural disorder was found in the top surface regions.

•   The second group of investigators [Giubertoni-10] combined XAFS and *ab-initio* structural simulations of defect structures with secondary mass spectrometry SIMS to measure the As

concentration, sheet resistance measurements and Hall effect to measure the carrier concentration and thus the fraction of active As dopants. Samples were obtained by implantation at 2 keV at a dose of 1 and 3×10^{15} atoms/cm^2 followed by laser submelt annealing or rapid thermal annealing; the latter process was followed by etching to remove the disordered topmost layers. The authors were able to fit the EXAFS data with a linear combination of the signal expected for As_{Si} and $v\text{-}As_n$ defects and thus obtain relative fractions of these different local As environments. They found a good correspondence between the fraction of active As sites determined from transport measurements and the relative amount of As_{Si} sites determined from EXAFS. This is illustrated by Fig. SMC4 in which the Fourier Transforms of the As K-edge EXAFS for various implanted samples are compared to a reference sample of substitutional As (topmost trace). The trace at the bottom corresponds to an as-implanted and amorphized sample and the intermediate ones to higher activation levels (3.4%, 29.5% and 27.3% for samples 4, 2 and 3); it can be noticed that the lineshapes clearly become increasingly similar to the reference as the active fraction increases from bottom to top. The same group subsequently reported on the deactivation of the dopants following thermal treatment [Giubertoni-10].

Both studies just reported clearly show that As is generally present in a range of local structures: As_{Si}, $v\text{-}As_n$ (n = 1 to 4) defects and SiAs precipitates, the first correlating well with the fraction of electrically active As (reasonable on the basis of textbook physics!). It can be commented that these results could not have been obtained without a significant contribution of *ab-initio* structural simulations; a simple analysis based only on the determination of the average coordination numbers in the first few coordination shells would certainly have failed to catch the details of this rather complex system.

Dopants in semiconductors and insulators

The increasing interest in the use of II-VI compounds in devices for room temperature x- and γ-ray detectors relies on their high resistivity, good signal-to-noise ratio and high mobility - lifetime product. High resistivity CdTe (which has has the zincblende structure and a direct band gap of ~ 1.5 eV) can be obtained by introducing Ge impurities which convert the intrinsically p-type CdTe to semi-insulating by the formation of a Ge related deep donor level that is responsible for the compensation of the native acceptors. However, if the Ge concentration exceeds a value of about 10^{17} cm^3, the material shows poor detector performance due to the activation of the so-called "lifetime killer" defects. In this context, Fraboni *et al.* [Fraboni-11] have coupled electrical

measurements with Ge K-edge XANES to study the variation of the Ge local environment with concentration and annealing treatments. By comparing measured XANES lineshape to *ab-initio* simulations (see Fig. SMC5) the authors confirmed that at low concentrations Ge is in a Cd substitutional site while at concentrations of the order of 1×10^{16} atoms/cm^3 Ge clustering occurs; Ge clustering was found to be correlated to the formation of electrically active deep donor traps, one located 0.31 eV below the conduction band edge and the other one at midgap, with an activation energy of 0.82 eV. This is one of the few examples in which the local structure determined from XAFS has been directly correlated with the electrical signature of a particular defect.

Metal induced crystallization (MIC) is one of the most effective methods for lowering the crystallization temperature of amorphous Si (a-Si). Various metals have been tested to reach the optimal thermal expenditure of MIC process. The possible chemical interaction of the metal impurities with *a*-Si during MIC process is a matter of discussion. Different mechanisms have been proposed for different metals used in the MIC phenomena. By using XAFS at the Cr edge Mohiddon *et al*. [Mohiddon-12] have studied its diffusion in the a-Si matrix. The Cr and Si films were deposited using electron beam evaporation onto fused silica substrates, using both metal − on − top and metal − on − bottom geometries at different substrate temperatures. XAFS measurements were performed at selected grazing angles of incidence in order to vary the depth sensitivity. Spectra were fitted with a combination of contributions from metallic Cr, Cr_2O_3 and $CrSi_2$, see Fig. SMC6. A detailed analysis indicated that metallic Cr diffuses into the *a*-Si matrix and reacts with it at sufficiently high temperature to form $CrSi_2$. This $CrSi_2$ acts as crystallization seed for *a*-Si.
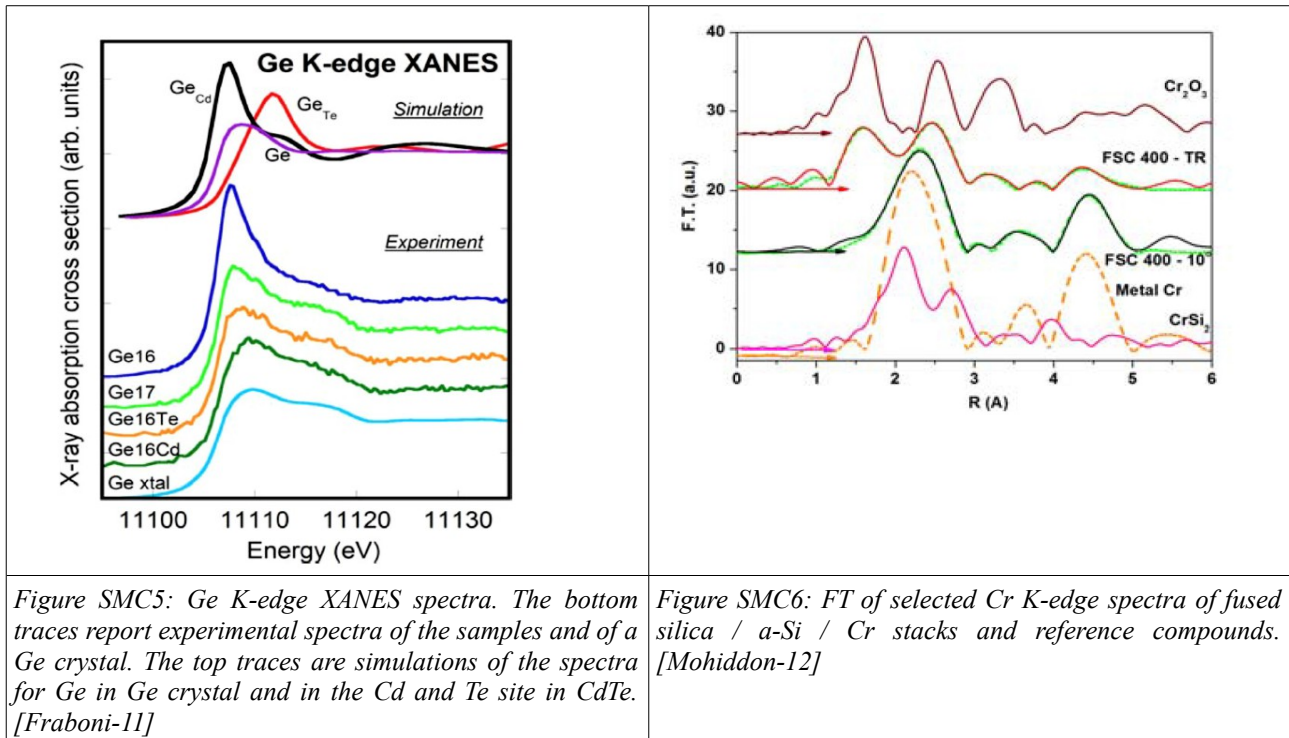
| *Figure SMC5: Ge K-edge XANES spectra. The bottom traces report experimental spectra of the samples and of a Ge crystal. The top traces are simulations of the spectra for Ge in Ge crystal and in the Cd and Te site in CdTe. [Fraboni-11]* | *Figure SMC6: FT of selected Cr K-edge spectra of fused silica / a-Si / Cr stacks and reference compounds. [Mohiddon-12]* |

Finally, a study on Pb ions in LiF have given a detailed description of the doping process in this system. The interest in this material comes from the easiness of formation of color centers in LiF that could be used for imaging X-ray detectors, with Pb enhancing the efficiency of the material. The structure around Pb was determined by Pb-L_3 and Pb-L_1 edge EXAFS and XANES. As a first point Pb was found to enter the crystal as Pb^{2+} [Somma-10] and that a nontrivial order was present around the metal as signals coming from Pb-F-Li collinear configuration was clearly detected [Dacapito-13]. The comparison with structural simulations and defect energy analysis based on Density Functional Theory has permitted to elucidate that Pb in the first steps of doping can enter both substitutional $Pb^{\bullet}_{Li}$ or interstitial $Pb^{\bullet\bullet}_{I}$ sites if in presence of charge compensating Li vacancies V'_{Li}. Then, the structure evolves towards an energetically favoured situation leaving only the complex $Pb_{Li}-V'_{Li}$ as final configuration [Dacapito-13].

Nanotechnology

C. Maurizio, Univ. Padova

The research activity on nanostructured materials at the GILDA beamline in the 2009-2013 period is mainly based on x-ray absorption spectroscopy (XAS) to investigate the nanostructures intentionally produced onto or into a matrix to tailor its specific macroscopic properties. X-ray absorption experiments on this kind of materials are often very demanding in terms of beam stability, especially for heterogeneous samples [Oppo-12] and of signal to noise ratio due to sample dilution, down to 10^{14} atoms/cm^2, or to 0.1 at% in a $\approx$50 nm thick surface layer [Maurizio-11, Cesca-12]. Experiments in total reflection/glancing angle condition allowed to probe the local structure of a very thin surface layer [Battocchio-11], giving crucial information on dopant diffusion [Mohiddon-12, Naidu-13]. Dichroic x-ray absorption measurements using the linearly polarized x-ray beam clarified the anisotropic order of epitaxial magnetic nanostructures [Liscio-10]. In the following, an overview of the main scientific achievements is presented.

Glass-based materials

Rare-earth (RE) doped glasses and glass-ceramics have been in the last five years and are at present the subject of many x-ray absorption spectroscopy experiments at the beamline. XAS experiments (rare-earth L$_3$-edges) have been carried out to get information on the RE sites [Ramamoorthy-12], in particular to investigate the RE solubility into the matrix [Ramamoorthi-13], that is an important issue in view of efficient RE emission properties. The experiments have clarified how in different glasses the local structure depends on the non-bridging oxygen concentration in the glass [Afify-09a,Ramamoorthy-13], while when crystallization occurs (glass ceramics) it has been evidenced that the dopant RE participates to the nanocrystal formation, with evident change of the photoluminescence properties [Oppo-12, Monteiro-13]. Moreover, in glass films doped with REs (Er in particular) it has been shown that RE doping of glass films in conditions far from the equilibrium produce substoichiometric Er environment with relatively short Er-O distances [Cattaruzza-10, Cattaruzza-09, Noe-09, Cesca-12], with relevant consequences on the Er optical properties [Noe-09, Cesca-12].

To increase the low excitation cross section of REs in glass matrices in view of optoelectronic applications, an effective way is to co-dope the glass with other nanostructures (for example metal clusters) that can act as nanoantennas, that efficiently absorb light in a broad range and transfer part

of the absorbed energy to the RE, that then de-excite radiatively. XAS is an elective tool to detect the formation of few-atom aggregates [Maurizio-11, Mazzoldi-13], as well as of dispersed metal fraction [Maurizio-09]. The aim of the performed experiments is to relate the optical properties with the sub-nanometer structure and metal site. XAS experiments performed at the GILDA beamline allowed to completely clarify the energy transfer process from metal aggregates to the RE. It is found that the effectiveness of the energy transfer process from metal aggregate to RE is size dependent (see Figure NT1), being smallest metal aggregates (few-atom clusters) the most efficient [Maurizio-10a, Maurizio-10b, Maurizio-11, Mazzoldi-11]. Possible effects related to matrix defects have been ruled out [Cesca-12]. A first indication that the energy transfer process also depends on cluster composition (alloy or single metal) has also been published [Maurizio-14]. Combined photoluminescence and XAS experiments (at both RE and metal edges) strongly suggests that the energy transfer from metal clusters to RE is due to the light excitation of surface electronic states of few-atoms clusters that are in resonance with the absorbing level of the nearby Er ions [Cesca-13, Cesca-14].
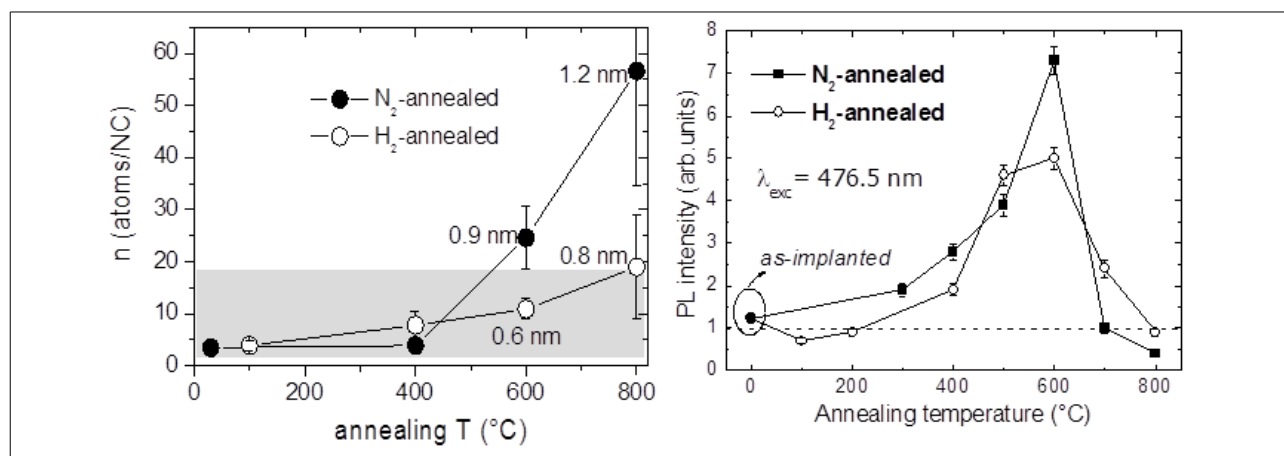
Figure NT1: Au cluster size (left) in Er+Au implanted silica as a function of the annealing temperature and (right) corresponding 1.54 μm Er photoluminescence intensity (out of resonance excitation) [Maurizio-11].

Nanostructured materials (excluded glass-based)

A relevant part of research on nanostructures is on catalytic materials for a number of applications such as CO oxidation, hydrogen storage and selective oxidation. XAS spectroscopy is crucial to relate the nanostructures with the efficiency of the catalyst, which can depend on the catalyst composition and structure, as well as on the catalyst/matrix interface. These materials have been the subject of a number of experiments at the GILDA beamline in the last 5 years.

XAS experiments combined with catalytic investigations on Pd, Au and AuPd nanoparticles prepared by metal vapor synthesis have shown that alloy clusters, formed by a Au core surrounded by a Au-Pd shell are more effective in promoting selective oxidation than the corresponding single-element clusters [Evangelisti-12, Balerna-13].

The crucial role of the catalyst/matrix interface has been investigated in ceria-supported Au nanoclusters for CO oxidation [Longo-12], where it is proposed that ceria crystalline structure serves as a sort of template for Au nanostructures (see Fig. NT2), mediated by a layer of O atoms. A crucial role of interfaces was also elucidated
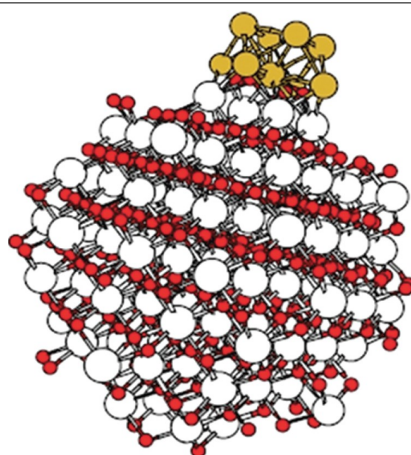
Figure NT2: Pictorial view of a gold cluster supported on ceria. Gold atoms in yellow, oxygen atoms in red, and cerium atoms in white, from [Longo-12].

in Mg-based nanostructures for hydrogen storage [Pasquini-11a, Pasquini-11b, Macchi-12]. In this last case in particular, it has been also evidenced that the catalytic efficiency of Nb catalyst in H sorption process was significantly enhanced when Nb was dispersed into the Mg matrix in form of very small (~ 1 nm) nanoparticles rather in larger clusters (15-20 nm) [Macchi-12].

The local structure measured by XAS or *in-situ* x-ray diffraction has been correlated to macroscopic magnetic or optical properties in nanocrystals [Cruciani-11, Torchio-10a, Torchio-10b] and thin films [Liscio-10, Maurizio-10c]. To this respect, the use of XAS combined to other characterization techniques is essential to get a full insight into the material structure, that is often multiphase [Maurizio-10c, Torchio-10a, Torchio2010b]. As an example of this kind of studies, fcc $CoPt_3$ nanostructures were epitaxially grown onto WSe_2 and their structure was investigated by polarized XAS (Co K-edge). A local structural anisotropy was detected, consisting in a preferential Co-Co bonding along the in-plane direction balanced with preferential heteroatomic bonding along the out-

of-plane direction. This was argued to be responsible for the unexpected perpendicular magnetic anisotropy detected for this system [Liscio-10].

In nanostructured materials especially synthesized to be used as pigments, it is of interest to relate the local structure with the material color, in order to optimize the synthesis process. XAS analysis performed at the beamline allowed correlating the $CoAl_2O_4$ layer color with the local structure of the spinel. In particular, it was found that the green-brownish color, occurring in specific preparation conditions, was due to a partial inversion of the spinel, while uninverted $CoAl_2O_4$ layers are of bright blue color. Temperature-resolved XRD analysis on nanocrystalline titania pigments produced by high temperature-forces hydrolysis in a coordinating high-boiling solvent elucidated how phase composition and crystalline size are drastically influenced by both synthesis condition and doping [Cruciani-10].

XAS spectroscopy has been successfully used to investigate the structure of Ag nanoparticles stabilized with thiols: depending on the synthesis route, clusters are found of metallic Ag [Mari-10] or having an Ag_2S shell surrounding a Ag core [Battocchio-12]. Surface structure around metal atoms in functionalized Pd(II) complexes has also been unveiled [Battocchio-10, Battocchio-11], in particular by means of XAS in total reflective geometry [Battocchio-11].

In the studies of the nucleation and growth mechanisms of metallic (single element or alloy) nanoparticles [Maurizio-12, Placido-09] a specific investigation has been carried out to undisclose the mechanism of Au nanorods growth in ultraviolet-driven photochemical synthesis route. A comparative XAS-TEM study has demonstrated that Ag^0 species, present in the synthesis process, are preferentially adsorbed on Au {110} facets of the growing Au nanoparticles, likely restricting crystal development along relevant crystallographic directions [Placido-09].

A review of XAS characterization of semiconductor nanostructures includes significant papers based on experiments at the GILDA beamline [Boscherini-08]. The structural investigations of Ge-doped CdTe and CdSe/ZnSe quantum dots complete the review [Fraboni-11, Piskorska-09, Piskorska-12]. Moreover, in the last years the crystallization of Si films induced by thin metallic layer (Cr or Ni) has been elucidated by XAS (Cr and Ni K-edges), in standard and total reflection conditions. It has been shown that the metal-induced crystallization is due to the diffusion of the metal into the amorphous Si, which then reacts to form silicides upon annealing, leading to Si crystallization at the silicide–Si interface [Mohiddon-12a, Mohiddon-12b, Mohiddon-13, Naidu-13].

Cements and porous systems

A. Gualtieri, Univ. Modena e Reggio Emilia

X-Ray powder diffraction (XRPD) and X-Ray absorption spectroscopy (XAS) techniques have been successfully used to investigate relevant topics in the field of Materials Science as cement and (micro- and meso-) porous systems. The specific features of the GILDA beamline allowed a full characterization of these systems both at a local (molecular) and statistical standpoint. Full structural characterization was possible both at room environment and *in situ* at high temperature. The use of the Rietveld method allowed both accurate quantitative phase analysis and structural characterization. The XRPD beamline set-up was used to perform time resolved studies, whilst XAS (for both XANES and EXAFS) experimental setup was used for studies on concentrated and diluted samples.

The studies performed at the Gilda beamline can be divided into two main topics:

1) *Cementitious materials*;

2) *Porous systems* divided into 2a) *Microporous materials*; 2b) *Mesoporous materials*.

1)*Cementitious materials*.

As far as the structure characterization of cement binders is concerned, [Biagioni-13] investigated the thermal behavior of two specimens of 14 Å tobermorite (plombièrite), a major paracrystalline phase formed during the setting of cement pastes. The experiment was conducted using *in situ* powder diffraction. During dehydration, plombièrite shortens its basal spacing from 14 to 11 Å, through a progressive approaching of the complex structural modules characterizing its crystal structure. Upon heating, the 11 Å phase progressively contracts its $\underline{c}$ periodicity, with its d_{002} varying from 11.7 to 11.3 Å. At ca. 300 °C, a 9.6 Å phase appears; it is stable up to ca. 700 °C. Above this temperature, it expands its basal spacing up to 10.2 Å, before transforming into wollastonite. This project was fully developed by the users from the University of Pisa and Parma (Italy).

The studies by the Spanish group of Cuberos et al [Cuberos-10], [Cuberos-09] aimed at the structural characterization of cement phases in active iron-rich belite sulfoaluminate cements and conventional and active belite cement pastes. The hydration of the cements was studied by laboratory and synchrotron X-ray powder diffraction (using Rietveld method and chemical constraints) and complementary techniques. Cement pastes have different hydration rates. For non-activated BSA cement, 20 and 48% of the belite reacted after one and three months, respectively.

Conversely, 37-49% after one month and 52-62% after three months of overall belite reactivity has been measured for BSA cements activated with boron oxide.

On the same line of research, [Martinsedeno-10] have published results on the clinkering and early age hydration of aluminum-rich belite sulfoaluminate cements. These projects were fully developed by the users from the Departamento de Química Inorgánica, Cristalografía y Mineralogía, Universidad de Málaga and Unidad Técnica de Investigación de Materiales, AIDICO, Valencia (Spain).

The piece of work presented by Gualtieri et al. [Gualtieri-09], who used the diffraction hutch to perform high temperature *in situ* experiments, aimed at the understanding of cement-asbestos transformation, in view of a safe recycling of the product of thermal decomposition. Cement–asbestos is the main asbestos containing material still found in most of the European countries such as Italy. Man- and weathering induced degradation of the cement–asbestos slates makes them a source of dispersion of asbestos fibres and represents a priority cause of concern. This concern is the main prompt for the actual policy of abatement and disposal of asbestos containing materials in controlled wastes. An alternative solution to the disposal in dumping sites is the direct temperature-induced transformation of the cement–asbestos slates into non-hazardous mineral phases. The product of transformation of cement–asbestos (CATP) has a phase composition similar to that of a natural or a low temperature clinker with the exception of having a larger content of aluminium, iron and magnesium. This product can be safely recycled for the production of bricks, plastic materials, and commercial concrete. The piece of work on the in situ X-ray powder diffraction study of the thermal decomposition of cement- asbestos was conducted by the users in collaboration with the scientists of the GILDA beamline.

Lassinantti Gualtieri et al. [Lassinantti-12] applied the Rietveld method to hydrated lime, a non-hydraulic traditional binder to detect the presence of amorphous phase. Both synchrotron radiation and a conventional X-ray source were used. The applicability of the developed control file for the Rietveld refinements was investigated using samples spiked with glass. The results were cross-checked by other independent methods such as thermal and chemical analyses. It was found that the consistency between the different methods was satisfactory, supporting the validity of FQPA for this material. The amount of amorphous material found in the samples was in the range 2–15 wt.%. This project was fully developed by the users from the University of Modena (Italy).

Taglieri et al. [Taglieri-13] performed the synthesis and X-ray diffraction analyses of calcium hydroxide nanoparticles in aqueous suspension. Calcium hydroxide nanoparticles in aqueous

suspensions (*nanolime*) are successfully employed in Cultural Heritage conservation thanks to the ability of favoring re-adhesion of the pictorial layer on original carbonatic sub- strates or allowing to a better superficial cohesion and protection of treated stones. The authors synthesized nanolime particles in aqueous suspension by two different methods. The produced particles were characterized. Nanoparticles were crystalline, regularly shaped, hexagonally plated and with side dimensions generally ranging from 300 nm to 30 nm or less (see Fig. CPS1).
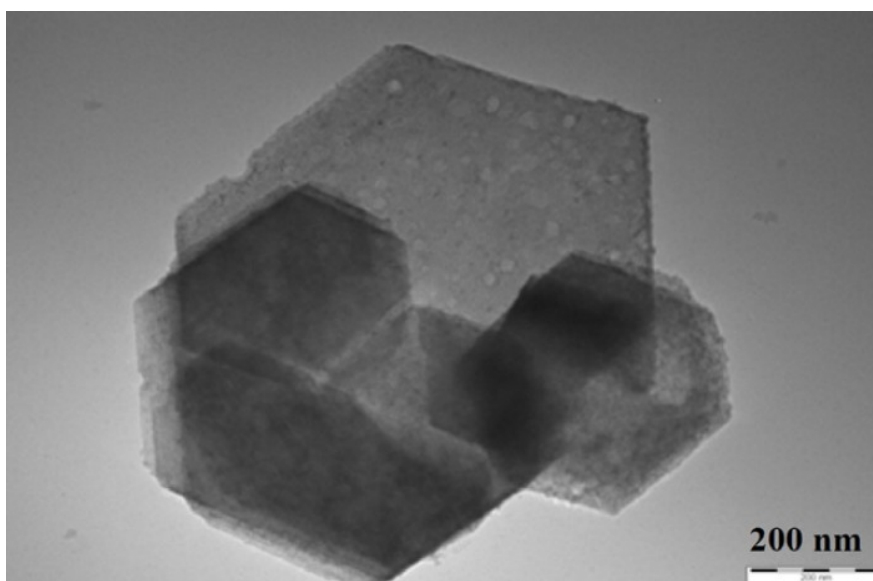
Figure CPS1: Ca(OH)₂ particles, hexagonally plated and regularly shaped, with side dimension of ca. 400 nm.

Crystal structure of nanolime particles directly in the aqueous suspension, has been analyzed by synchrotron powder diffraction. Data have been analyzed by means of the Rietveld method and focused on the structure of $Ca(OH)_2$ particles in suspension in terms of cell parameters, atomic coordinates, bond lengths and angles. This project was developed by the users of the University of l'Aquila (Italy) in collaboration with the scientists of the GILDA beamline.

2) *Porous systems*

2a) *Microporous materials*

Agostini et al. [Agostini-10] investigated *in situ* the dealumination of NH4-Y zeolite during steaming to 873 K, with combined Al K-edge XAS and synchrotron powder diffraction experiments. Water desorption is complete at 450 K, and ammonium decomposition occurs between 500 and 550 K. Only a small fraction of Al^{3+} species (5%) leaves the framework during heating from 710 to 873 K; these species occupy site I′ inside the sodalite cage. This fraction increases up to

8% in the first 50 min at 873 K and remains constant for the following 70 min isotherm and during the high-temperature part of the cooling experiment. During cooling from 500 to 450 K, the electron density at site I′ increases suddenly, corresponding to a fraction of 30-35% of the total Al. At that temperature, in situ Al K-edge XAS indicates a change in Al coordination of a large fraction of Al (see Fig. CPS2). Such molecules drive the dislodgment of most of the Al from the zeolitic framework. Data indicate that considerable structural collapse caused by steaming does not occur at the highest temperature; however, defects form, which lead to significant migration of framework Al^{3+} to extraframework positions, which occurs only as water is able to enter the pores again, that is, at much lower temperature. The results contribute to a better understanding of the phenomena involved on the atomic scale in the preparation of ultrastable Y zeolites (USY). USY are employed in fluid catalytic cracking (FCC), which is the most important conversion process in petroleum refineries to convert the high-boiling hydrocarbon fractions of petroleum crude oils to more valuable products like gasoline and olefinic gases. This project was fully developed by the users from Torino University in collaboration with Nano-SiSTeMI Interdisciplinary Centre, Universita` del Piemonte Orientale, Alessandria, Italy, the Paul Scherrer Institut, Switzerland, and ETH Zurich, Switzerland.
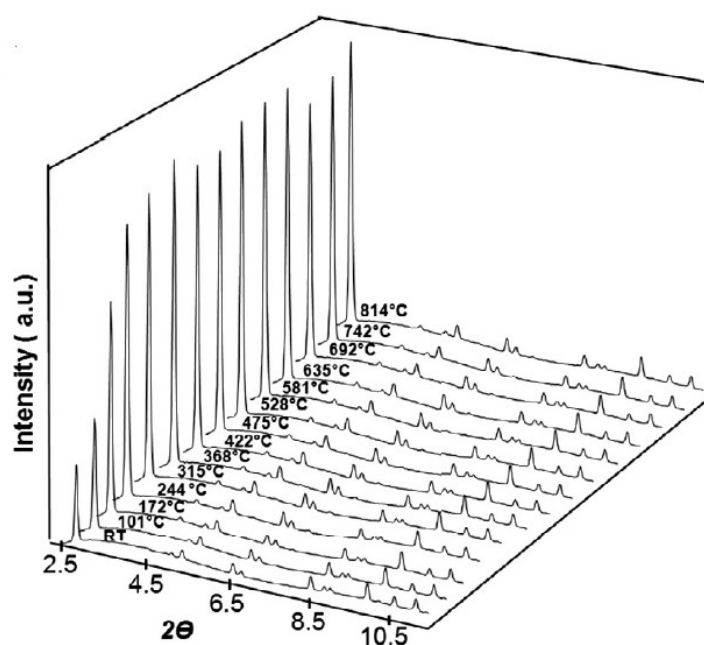

Figure CPS2: Selected powder patterns of zeolite L as a function of temperature reported in the 2θ range

In situ synchrotron X-ray powder diffraction was employed to investigate the dehydration and thermal stability of the synthetic zeolite K-L [Gigli-13]. In the room temperature to 814 °C range (Fig. CPS2), neither structure breakdown nor phase transitions occurred. The largest unit cell deformation was observed between 100 and 240 °C, accompanied by an increase and decrease of the a and c cell parameters, respectively. After complete water release, an inversion of the a and c parameter behavior was observed, while the cell volume continued to increase, although following a more flattened curve. Overall, in the investigated temperature range, a small cell volume increase of 0.7% was observed. The release of the five water molecules present in zeolite L started with the most weakly bonded one and occurred between 80 and 240 °C. During dehydration the framework underwent minor rearrangements, which facilitated water release: the apertures of the main 12-ring and the 8-ring channels became more circular and the 6-membered rings became more hexagonal. The thermal expansion of zeolite L, very unusual for a non-siliceous zeolite, was interpreted and compared with previous data reported in literature for this porous material, and with the behavior of the synthetic phases ITQ-4 and CIT-5. This project was fully developed by the users from the University of Modena and Reggio Emilia (Italy), and Institut Charles Gerhardt de Montpellier, Montpellier, France.

In a series of papers, Leardini an co-workers [Leardini-12a], [Leardini-12b], [Leardini-13] studied the behaviour of both synthetic (boron-ZSM-5, silica sodalite) and natural (levyna) zeolites at high temperature "in situ" using time-resolved synchrotron powder diffraction. This research line was independently developed by the users from the Ferrara University (Italy).

On the same line, the dehydration process of slightly hydrated boron leucite was followed by Martucci et al. [Martucci-11]. A time-resolved experiment was performed using the TIPS (translating imaging plate system). Results show that temperature-induced transformations can be schematized into two main steps. In the 25–565 °C temperature range, the symmetry remained cubic and the unit cell parameter increased with an increase in temperature. The migration of water molecules through the [1 1 1] channels during dehydration determined an opening of the six-member ring apertures which was as wide as possible and, at the same time, a narrowing in the eight-ring along [1 1 1]. This process was accomplished by a twisting in the tetragonal prism, constituting a leucite framework, which led to an opposed tilting in the tetrahedra connecting the prisms. Above 565 °C, a continuous structural transformation led to a displacive polymorphic transition. Rietveld structure refinement of the unit cell parameters showed a remarkable change, thus indicating a change in symmetry. This was associated with a relaxation in the continuous

structural distortions of the leucite framework and the T–O–T and O–T–O angles indicated the formation of more regular apertures. This project was fully developed by the users from the Ferrara University (Italy).

The successful research line on the dehydration dynamics of natural zeolites conducted *in situ* with X-ray synchrotron powder diffraction also included the contributions of Ori and co-workers [Ori-09a], [Ori-09b]. The group from the Modena University specifically focussed on the dehydration dynamics of barrerite and the thermally induced structural modifications of the high silica zeolite gottardiite. These pieces of work were fully developed by the users.

Finally, Sacerdoti and Cruciani [Sacerdoti-12] investigated the high temperature behaviour of zorite, a microporous titanosilicate, with ideal chemical formula $Na_6Ti_5Si_{12}O_{36}.\times 11H_2O$ and compared it to the synthetic counterpart Na-ETS-4. These works were fully developed by the users from the Ferrara University.

2) *Porous systems*

2b) *Mesoporous materials*.

As far as mesoporous materials are concerned, Bracco et al. [Bracco-11] investigated the supramolecular self-assembly of a host molecule with selected blocks of triblock copolymers to form inclusion of 2D nanocrystals that connect consecutive copolymer chains. The selective inclusion of ethylene oxide (EO) blocks in inclusion crystals and the phase segregation of PO blocks of poly(ethylene oxide-b-propylene oxide-bethylene oxide) (EOnPOmEOn) triblock copolymers provide an efficient route to create alternated crystalline lamellae and amorphous layers, forming a well-organized material. The spontaneous formation of the supramolecular architectures was realized by a solvent-free mechanochemical approach or by thermal treatment of the copolymer and host (tris-o-phenylenedioxycyclotriphosphazene), as demonstrated by *in situ* synchrotron X-ray diffraction. The powder X-ray diffraction patterns were performed at variable temperature, from room temperature to 630 K at different heating rates ranging from 0.5 to 1 K/min. This project was fully developed by the users from the Department of Materials Science, University of Milano Bicocca (Italy). Fig. CPS3 reports the structure configuration as obtained by the Rietveld structure refinement.
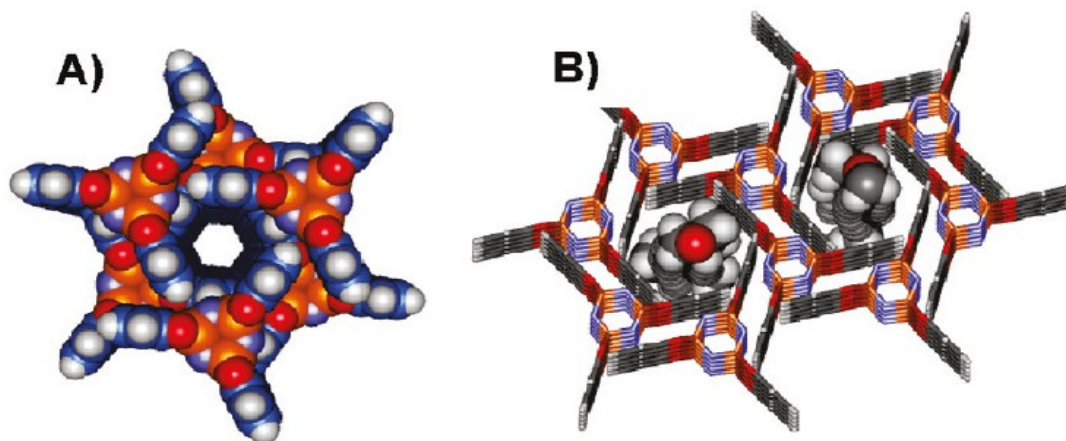
Figure CPS3: (A) The hexagonal crystal structure presents a one-dimensional channel made by paddle-wheel shaped TPP molecules that line the walls with their phenylenedioxy aromatic units facing the channels; (B) The complementary shapes of the TPP nanochannels and the poly(ethylene oxide) chains facilitate association through supramolecular interactions.

A beautiful example of self-assembly of multiple components into well-defined and predictable structures was proposed by Liu et al. [Liu-11], using diffraction data collected at the GILDA beamline. The results of this study were published on Science. These authors reported the rational design of a supramolecular cage assembled from 20 ions of three distinct species through 72 hydrogen bonds. The cage is constructed from two kinds of hexagonal molecular tiles, a tris(guanidinium)nitrate cluster and a hexa(4-sulfonatophenyl)benzene, joined at their edges through complementary and metrically matched N-H···O-S hydrogen bonds to form a truncated octahedron, one of the Archimedean polyhedra. The truncated octahedron, with an interior volume of 2200 cubic angstroms, serves as the composite building unit of a body-centered cubic zeolite-like framework, which exhibits an ability to encapsulate a wide range of differently charged species, including organic molecules, transition metal complexes, and "ship-in-a-bottle" nanoclusters not observed otherwise. This project was fully developed by the users from the Department of Chemistry and the Molecular Design Institute, New York University (USA) in collaboration with the Department of Materials Science, University of Milano Bicocca (Italy).

Tedesco et al. [Tedesco-10]were involved in a long term project on the study of the self-assembly properties of the proximal p-tert-butylcalix[4]dihydroquinone compounds to investigate the role played by crystallization conditions in driving the formation of a previously reported cubic porous framework. In chloroform and anhydrous ethyl acetate, the mutual inclusion of the tert-butyl groups is favored, leading to the cubic porous structure; otherwise, in the presence of a higher water amount, the OH groups provide H-bonds with bridging water molecules and a new triclinic crystal structure is obtained, in which the calixarene molecules include chloroform inside their cavities. By

exposing a cubic/triclinic powder mixture to acetonitrile vapors, a new monoclinic chiral crystal structure is obtained by supramolecular assembly of calixarene, acetonitrile, and water molecules with the formation of single handed helices. XRPD images for the crystalline powder before and after one day exposure to CH_3CN vapors were recorded using the translating imaging plate system available at GILDA allowing the in situ monitoring of the crystallographic transformation induced by the guest uptake and release, also as a function of the temperature. This piece of project was developed by the users from the University of Salerno (Italy) in collaboration with the scientists of the GILDA beamline.

On the same research line, Erra et al. [Erra-12] with the aid of *in situ* powder diffraction studied the inclusion properties of a calixarene-based porous material to investigate the adsorption and the desorption of carbon tetrachloride, chloroform, and water in the zeolite-like structure. Uptake and release processes have been studied both by time-resolved powder X-ray diffraction and by thermogravimetric analysis to obtain structural and kinetic information. The selected guests are able to enter the structure with an increase in the host cell volume and with time-dependent diffusivity coefficients. Chloroform molecules act as a permanent porosity switch promoting a phase transition to non-porous triclinic form. This project was also developed by the users in collaboration with the scientists of the GILDA beamline.

Chemistry

P. Ghigna, Univ. Pavia

In the field of chemistry GILDA has been particularly active in the development of new instruments and methods of data analysis. A new technique for electrochemistry has been developed [Minguzzi-13] and the CARD program for the quantitative analysis of the ReflEXAFS data is now at a full maturity [CARD-12, Costanzo-14]. Also users have contributed to this activity by developing their proper instrumentation for *in-situ* treatment in close contact with the beamline staff [Centomo-13, Minguzzi-13]. The capability of GILDA of investigating surface systems and thin films via the Grazing Incidence or Total Reflection XAS have permitted the realization of several studies in different fields like surface reactions, adsorption and characterization of extremely thin films. The possibility of working at high energy on diluted materials has permitted the realization of series of works on protonic conductors.

Catalysis has been widely investigated by both in situ and ex situ XAS methods. For *in situ* studies, that are completely reviewed in [Bordiga-13] a novel flow-through catalytic cell has been developed allowing experiments on heterogeneous catalysts under working conditions and in the presence of a gas phase. The versatile design of the cell allows fitting it to different experimental setups also in different synchrotron radiation beamlines [Centomo-13]. Ex situ methods have been used in [Rossetti-12] for correlating the catalytic performance for the oxidative dehydrogenation (ODH) of propane to propylene of different oxidic materials based on V_2O_5 with the local structure of the V active sites has been deeply investigated by X-ray absorption spectroscopy, allowing to propose a possible structure of the active sites.

Electrochemistry is another field that has been actively explored both for what concerns methods and materials. Fixed Energy X-ray Absorption Voltammetry (FEXRAV) was introduced, representing a novel in situ X-ray absorption technique for fast and easy preliminary characterization of electrode materials and consisting of recording the absorption coefficient at a fixed energy while varying at will the electrode potential. The energy is chosen close to an X-ray absorption edge, in order to give the maximum contrast between different oxidation states of an element. It follows that any shift from the original oxidation state determines a variation of the absorption coefficient [Minguzzi-13]. For what concerns materials for electrochemistry, materials for Li-based ion batteries such as $Li_{1-x}Fe_{1-x}V_xPO_4/C$ (with $0 \leq x \leq 0.1$) have been studied, demonstrating that V enters the olivine structure substituting for Fe [Moretti-13]. In addition, IrO_2-

based powders, active as electrocalysts in the water splitting reaction, were studied by XAS for what concerns the local structure of each selected sample, confirming the trends found by cyclic voltammetry and give new and unexpected insights on the powder structural features [Minguzzi-12].

Protonic conductors such as $La_{1-x}Ba_{1+x}GaO_{4-\delta}$, Y:BaCeO$_3$, In:BaCeO$_3$, Gd:BaCeO$_3$, Y:BaZrO$_3$, and In:BaZrO$_3$ were extensively investigated using X-ray diffraction (XRD) and X-ray absorption (EXAFS) [Giannici-11, Giannici-10, Giannici-09a, Giannici-09b]. The structure of the GaO$_4$ groups in $La_{1-x}Ba_{1+x}GaO_{4-\delta}$, is independent of the oxide composition. Concerning Y:BaCeO$_3$, In:BaCeO$_3$, Gd:BaCeO$_3$, Y:BaZrO$_3$, and In:BaZrO it was found that each different dopant shows unique behavior, depending mainly on its electronic structure, and that the usual criterion of ionic radius matching is not useful to outline an effective doping strategy of proton-conducting perovskites (Fig. CH1).
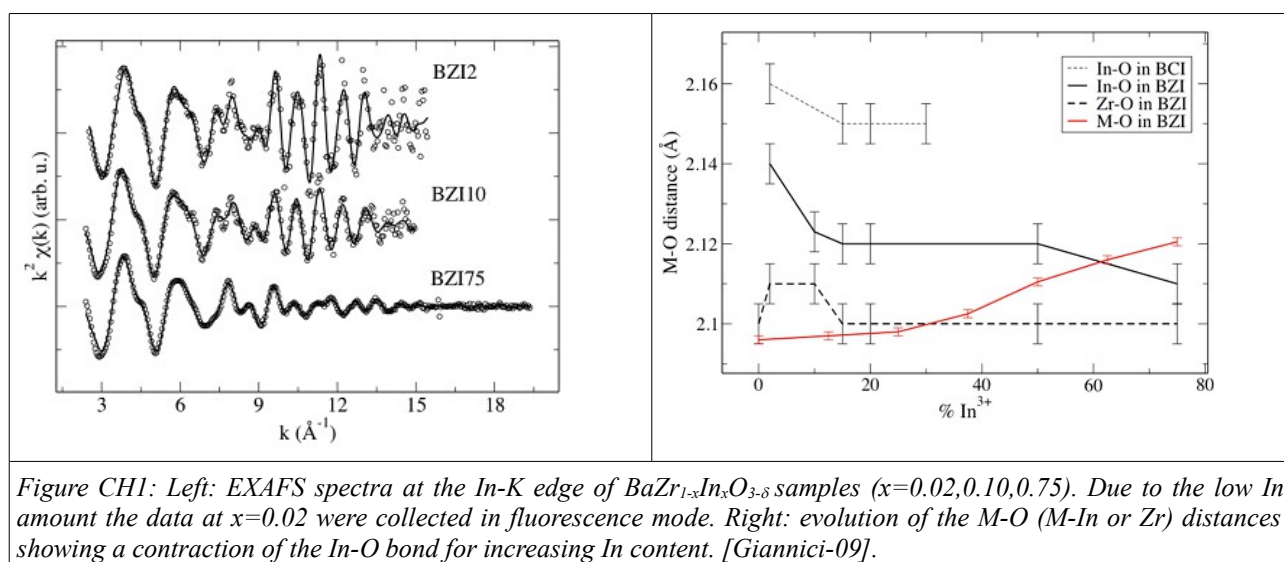
Figure CH1: Left: EXAFS spectra at the In-K edge of BaZr$_{1-x}$In$_x$O$_{3-\delta}$ samples (x=0.02,0.10,0.75). Due to the low In amount the data at x=0.02 were collected in fluorescence mode. Right: evolution of the M-O (M-In or Zr) distances showing a contraction of the In-O bond for increasing In content. [Giannici-09].

The potential and application of X-ray absorption spectroscopy (XAS) for structural investigations of organic–inorganic hybrid materials, with a special emphasis on systems consisting of inorganic building blocks (clusters) embedded into polymer backbones, is extensively reviewed in [Gross-10]. For example, EXAFS was used in [Di Noto-09] to prove the integrity of the wheels once embedded in the macromolecular backbone in the organic–inorganic hybrid materials based on the embedding of a chromium–nickel wheel cluster $\{[(n-C_3H_7)_2NH_2]-[Cr_7NiF_8(O_2C_4H_5)_{16}]\}$ (Cr7Ni) into poly(methyl methacrylate).

Nanochemistry has also be explored in [Giannici-09]. In this study, the mechanisms of the synthesis of water-soluble gold nanorods (Au NRs) by a silver-ion mediated photochemical route under UV irradiation were investigated by means of EXAFS at the Ag K-edge, allowing to probe the chemical state and the local environment of silver in the final product.

Oxidic film epiaxially deposited onto different substrates were extensively investigated [Luches-13, Niu-13, Colonna-09, Tougerti-12]. Cerium oxide ultrathin films supported on Pt(111), were investigated by X-ray photoemission spectroscopy, and the surface structure, measured by low-energy electron diffraction, is compared with the results obtained by the analysis of X-ray absorption fine structure measurements at the Ce L_3 edge, exploiting the polarization dependence of the cross section to probe the in-plane and the out-of-plane atomic correlations, allowing to establish the epitaxial relation between the cerium oxide film and the Pt substrate and give an accurate evaluation of the cerium oxide layer fluorite. The measured compression is compatible with the assumption of a coincidence lattice between overlayer and substrate, in which three CeO_2 surface unit cells match four Pt unit cells. The three-dimensional structure of films with whit different thicknesses is compared with the one expected assuming the bulk-phase elastic constants [Luches-13]. Ternary single crystalline bixbyite $Pr_xY_{2-x}O_3$ films over the full stoichiometry range (x = 0–2) epitaxially grown on Si (111) with tailored electronic and crystallographic structure, were studied for what concerns their local atomic environment by extended X-ray absorption fine structure at both Y K and Pr L_{III} edges, in combination with complementary high resolution x-ray diffraction measurements. The local structure exhibits systematic variations as a function of the film composition [Niu-13]. A structural characterization of the Fe/NiO(100) and Fe/MgO(100) interfaces is also reported by polarization-dependent X-ray absorption spectroscopy: the Fe/MgO(100) interface does not show a significant Fe oxidation or oxygen diffusion while a buckled Fe–O like layer is observed at Fe/NiO(001) [Colonna-09].

Using total reflection XAS and Polarization-dependent EXAFS permitted the characterization of Ni absorbed on Alumina [Tougerti-12]. XAS and XANES ab initio simulations, proved that the for surface precipitated $Ni(OH)_2$ films are parallel to the (012) surface of sapphire, while no deposition of Ni(II) takes place on the (001) surface. Surface precipitation was explained by surface grafting of the Ni precursor ($[Ni(en)(H_2O)_4]^{2+}$) exclusively on the (012) α-Al_2O_3 face and minimization of the total surface energy between the Al_2O_3 surface and α-$Ni(OH)_2$. The use of planar model systems emphasizes the crucial role of specific Al_2O_3 surface orientations for controlling Ni adsorption and dispersion in industrially relevant catalysts [Tougerti-12].

The initial steps of the reaction between ZnO and Al_2O_3 have been deeply investigated [Pin-13a, Pin-13b, Pin-12, Pin-09] using an approach involving X-ray diffraction, atomic force microscopy, and X-ray absorption spectroscopy at the Zn–K edge, starting from epitaxial ZnO films of different thicknesses, deposited on differently oriented sapphire crystals (Fig. CH2). The formation of nonequilibrium phase(s) has been detected in most cases. For the $(001)_{zincite}$ $\|$ $(110)_{sapphire}$ interface, the rate-determining step is the motion of the interface(s); the growth of the spinel layer is linear with time, with a rate constant $k = 1.1(2) \times 10^{-9}$ cms^{-1} at 1000 °C. At the $(110)_{zincite}$ $\|$ $(012)_{sapphire}$ interface, the reaction shows dumped oscillations. For the (001)-oriented Al_2O_3 the reaction eventually yields the $ZnAl_2O_4$ spinel via a complex mechanism involving side and intermediate nonequilibrium compounds, the spinel initially forming with a distribution of lattice parameters. One of these compounds, playing a role similar to reactive intermediates in solution chemistry, has been trapped for the (110) sapphire interface.
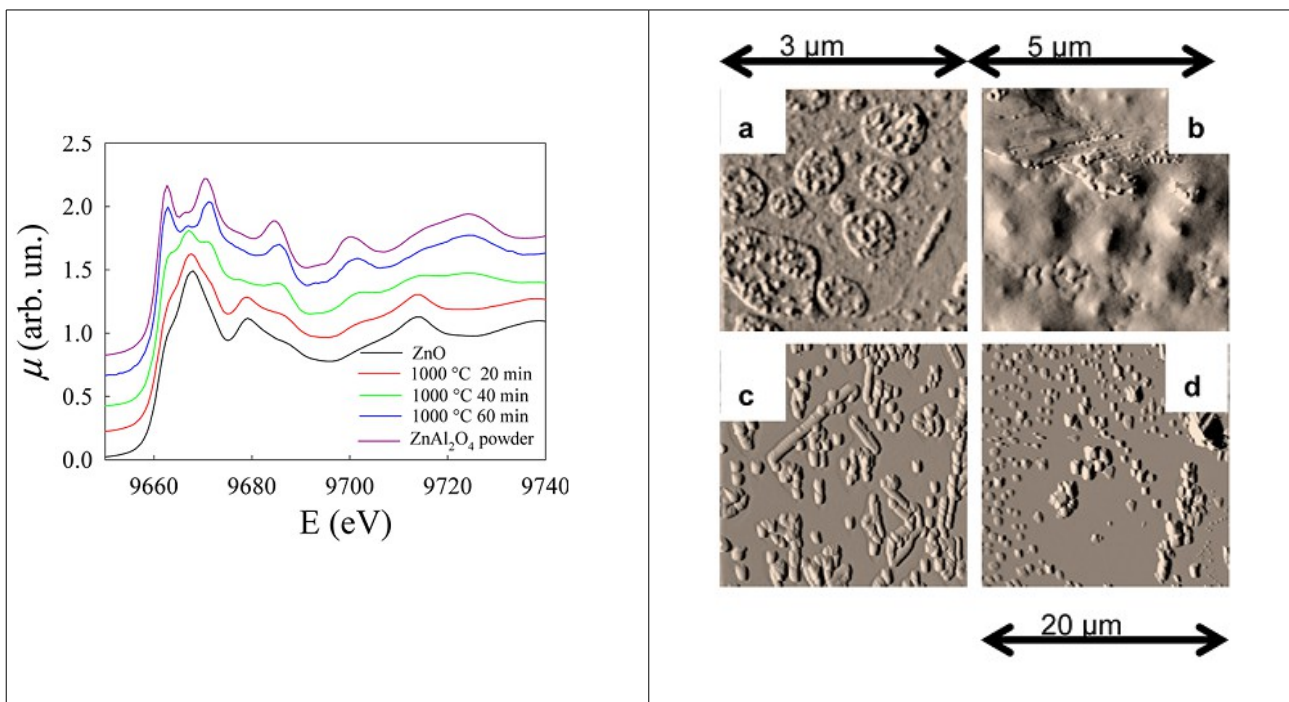
Figure CH2: Left: Evolution of the structure of the ZnO/Al₂O₃ interface treated at 1000 °C for increasing times. 45Nm of ZnO were grown on the (001) face of Al₂O₃ substrate. Right: AFM characterization of a 15nm ZnO grown on (001) Al₂O₃ and treated at 800 °C for 20min (a), 40 min (b), 60 min (c), 120 min (d). Measurements were collected at the AFM facility of GILDA. Figures from [Pin-13a].

These unprecedented experimental findings demonstrate that in a solid-state reaction, the topotactical relationships between the reacting solids are of crucial importance not only in

determining the kinetic and mechanisms of the process in its early stages, but even the chemical nature of the product. All these results have been the subject of a PhD thesis [Pin-10].

X-ray absorption spectroscopy proved also very effective in the study of multilayers [Pompeo-13, Pasquali-11, Mancini-11]. Nb/PdNi/Nb trilayers have been studied as a function of the ferromagnetic layer thickness. With respect to pure Nb, XAFS analysis shows that the heterostructures exhibit larger structural disorder in the superconducting layers [Pompeo-13], obtaining evidences that the ferromagnetic layer acts on the superconducting state. Yb_2O_3/Si(001) and Yb_2O_3/SrF_2/Si(001) were studied by photoemission and x-ray absorption fine structure. A uniform single layer of SrF_2 molecules blocks intermixing and reduces the oxidized Si region to 2.4 Å after deposition and to 3.5 Å after annealing at 500 °C. Sr K edge measurements indicated that the ultrathin fluoride films are reacted, with the formation of bonds between Si and Sr [Pasquali-11]. In the case of the interface between cube textured Ni-W substrates, both bare and Pd-buffered, and the CeO_2/YSZ buffer layer structure-required to growth YBCO coated conductors-samples, XAS was used to probe the Ni-Pd interdiffusion layer, finding that the formation of NiO can be completely prevented while the formation of ternary oxides and of W oxide is favoured [Mancini-11].

Films for optical [Carria-11] and electronic [Giubertoni-10] applications have been also investigated. In the case of s $Ge_2Sb_2Te_5$ films (50 nm) prepared by sputtering (AD), melt quenching, or ion irradiation has been probed by EXAFS and Raman spectroscopy., the EXAFS at the Ge K edge was used for a deep structural study, finding that in the AD films show stronger contribution from the homopolar Ge-Ge bonds with respect to irradiated films [Carria-11]. XAS spectroscopy was also used in the case of single crystal Si (100) wafers implanted with As ions for studying the local structure of As [Giubertoni-10].

The study of epi-layers and buried interfaces at the beamlime is greatly by the state-of-the-art experimental apparatus and proper setup to perform x-ray absorption spectroscopy (XAS) experiments in grazing incidence mode. Both the calculation and the experimental data demonstrate that the specific setup that consists in a grazing incidence and grazing collection geometry is extremely advantageous when compared to the standard geometry used to perform XAS experiments in fluorescence mode, allowing an enhancement in the fluorescence signal from the surface layer without a corresponding increase in the elastic scattering contribution from the matrix [Maurizio-09].

Earth Science

G. Giuli, Univ. Camerino

X-Ray powder diffraction (XRPD) and X-Ray absorption spectroscopy (XAS) techniques have been successfully used in order to investigate relevant topics in Earth Science and related fields. The XRPD beamline set-up is particularly suited for time resolved and/or high-temperature studies, but has been also employed for mineralogical identifications in micrometeorites and impact glasses recovered from Antarctica.. XAS experimental setup has been extensively used for XANES and EXAFS studies which highlighted the structural role of major and minor elements within a crystalline structure or a silicate glass representative of terrestrial magmas.

Determination or refinement of the average crystal structure

Crystal structure determination or structural refinements have been performed on a variety of materials ranging from natural minerals to synthetic mineral analogues.

X-Ray Powder Diffraction (XRPD) data have been used to refine the structure of a natural Co-bearing mansfieldite [Zoppi-09] giving insight on the Co location into the Al site and on structural details of the Al octahedra.

The possibility to collect time resolved spectra thanks to the translating image plate available at Gilda allowed to measure non ambient high temperature XRPD data of a synthetic $Co_3Al_2Si_3O_{12}$ garnet [Tribaudino-11] and of synthetic $LiCrSi_2O_6$ and $LiNiSi_2O_6$ pyroxenes [Tribaudino-09]. In both cases, the setup available at Gilda allowed to determine the lattice parameters variation as a function of temperature. Particularly for the case of pyroxenes, the possibility to collect also low intensity diffraction data, and the accurate determination of cell parameters variations as a function of temperature gave indications on the lattice centering of these samples in the studied temperature range. Moreover, the comparative analysis of the thermal and spontaneous strain contributions in P21/c and C2/c pyroxenes indicated that the high temperature strain in P-$LiNiSi_2O_6$ is very similar to that due to thermal strain only in C2/c spodumene and that a spontaneous strain contribution related to pre-transition features is not apparent in $LiNiSi_2O_6$.

As garnets are a mineral group of great relevance for petrologic studies and for technological applications, several structural studies have again been devoted to reveal structural details of the high temperature behaviour of garnets or to highlight the role of chemical substitutions on local structural distortions. The high temperature structure and thermal expansion of $Co_3Al_2Si_3O_{12}$ garnet

has been studied by XRPD [Tribaudino-11] at T = 298, 423, 573, 723 and 873 K providing novel data on the volume thermal expansion coefficient. The results on synthetic $Co_3Al_2Si_3O_{12}$ garnet were compared with the high temperature structure data of $X_3Al_2Si_3O_{12}$ garnets (with X = Mg, Ca, Mn and Fe) taken from the literature indicating that thermal expansion of the unit cell is very similar in all $X_3Al_2Si_3O_{12}$ garnets so far studied, whereas the thermal expansion of the longest bonds in the distorted cubic cage surrounding the X cation decreases with increasing cation size. Contrarily to the compression behaviour, the thermal expansion in $X_3Al_2Si_3O_{12}$ garnets does not change significantly as a function of composition.

A combination of XANES and EXAFS analyses have been performed to study the Fe local environment in a synthetic $Ca_3Zr_2[Fe_2SiO_{12}]$ garnet by Giuli et al. [Giuli-12]. The XANES data indicated the presence of trivalent Fe in tetrahedral coordination. The EXAFS-derived 〈Fe-O〉 distance (1.85 ± 0.01 Å), while in agreement with the few literature data available for $^{[4]}Fe^{3+}$, i.e. tetra-ferriphlogopite (〈Fe-O〉 = 1.86 ± 0.01 Å), rodolicoite (〈Fe-O〉 = 1.825 Å) and silicate glasses (Fe-O = 1.85 ± 0.01 Å and 1.84 ± 0.02 for phonolitic and rhyolitic glasses, respectively) is much larger relative to the Si-O distance usually found in garnet group minerals. Comparison of XAS-derived local structural information on the Fe environment and XRD derived structural data on the average structure allowed to remark the advantage of combining local vs average techniques to reveal details of the role of chemical substitutions on local structural distortions. Although there are still open questions on the distribution of FeO_4 and SiO_4 tetrahedra and on how the structure accommodates the size difference of these two tetrahedra, this study provided a direct determination of the $^{[4]}Fe^{3+}$-O distance for which only few data are available in the literature.

The use of local techniques is particularly useful also to study the local environment of minor to trace elements in crystalline materials. In this case, in fact, the low concentration of a substituting element does not produce appreciable variations in the average unit cell size or in the average polyhedral bond lengths. Thus, spectroscopic determinations of the local geometry around a dopant element are the only clue of the site location of this element and of the structural distortions triggered by its incorporation into a given site. A Fe K-edge XAS study of amethyst has been performed by Di Benedetto et al. [Dibenedetto-10] on a set of samples of natural α-quartz (SiO_2) providing first hand data on the local geometry and the oxidation state of iron in these materials. In particular, combination of Density Functional Theory structural modelization with EXAFS and XANES data allowed to state the valence state 3+ for the metal and the occurrence of complexes (FeO_3)-OH site Fe substitutional for Si. These data are particularly useful to try explaining the

origin of colour in a widely known gem material like amethyst. Moreover, these data have also implications to understand how Fe speciation in quartz contributes to the variety of health effect of crystalline silica.

Mineralogical identification of crystalline phases in microscopic materials.

The use of high intensity X-ray beam focused to a small (hundreds of μm) size is also particularly useful for performing mineral identification in materials which, due to their minimal size or extremely small concentration of crystalline material present, are difficult to characterize by other laboratory techniques. This is particularly the case for micrometeorites and microscopic impact glass spherules recovered in the Antarctic.

Folco et al. [Folco-09], discovered impact glass spherules in the Transantarctic mountains interpreted to be microtektites from the australasian strewn field. XRPD data collected at GILDA allowed to ascertain the presence of sulphate coating (jarosite and gypsum) on some of the microtektites. Similar studies extended to Australasian microtektites recovered from deep-sea sediment cores within 2000 km of Indochina, allowed to report the occurrence of microscopic inclusions of shocked quartz plus a Zr phase and trace of Fe oxide crystallites in these rare samples. The shocked quartz and the Zr phase were interpreted as relicts of the target rock, giving hints on the localization of the source crater of the australasian tektites, and also suggesting that the Australasian microtektites with the longest trajectories underwent the highest temperatures or were heated longer.

Combination of synchrotron X-ray diffraction data with scanning electron microscopy and electron probe microanalyses, is also applicable to small micrometeorites and provides precious mineralogical data greatly helping their correct classification. Van Ginneken et al. [Vanginneken-12], in analizing a series of micrometeorites from Antarctica took advantage of the mineralogical information provided by the use of an intense X-ray beam and in recognising the presence of chondritic micrometeorites. Besides reporting the first occurrence of a CV-like micrometeorite, their study showed that the abundance of chondritic material supports observations from recent studies on cosmic spherules that a large part of the micrometeorite flux in this size range is of asteroidal origin.

Accurate mineralogical and geochemical data obtained by means synchrotron X-ray diffraction,

combined with field emission-scanning electron microscopy, electron microprobe analyses, and magnetization measurements also allowed to carefully characterise porous aggregate of quench-textured spherules (individual spherules ranging from less than 1 to 65μm in diameter) found in the transantarctic mountains along with micrometeorites and microtektites. These Spherule types, which include porphyritic olivine plus magnesioferrite spherules, dendritic magnesioferrite spherules, barred and feathered olivine spherules, and cryptocrystalline spherules have been interpreted as evidence for a Tunguska-like impact [VanGinneken-10].

Powder X-ray diffraction has been also employed to characterise the mineralogical composition of yyrometamorphic ejecta erupted during recent paroxysmal explosions and hydrothermally altered volcanic and subvolcanic rocks from Stromboli volcano (Aeolian Islands, Italy). Accurate determination of all the mineral phases assemblages present in the samples allowed Del Moro et al. [Delmoro-11] to classify these samples as buchites; that is, glass coupled with a high-temperature, low-pressure modal mineralogy. Three distinct phases (i.e. cordierite-plagioclase, mullite-plagioclase palisade and tridymite-clinopyroxene) were recognized among the buchites, strongly supporting the origin of the buchite ejecta as hydrothermally altered rocks from the Vancori edifice (a period of activity spanning >10 kyr), which underwent high-temperature, low-pressure contact metamorphism.

Determination of minor to trace element redox state and structural environment in silicate glasses representative of terrestrial magmas.

Silicate glasses are thought to represent a good proxy of the atomistic structure of a silicate melts at the temperature of melt to glass transition. As a consequence, they have been widely studied in the literature in an effort to try to reconstruct the structural properties of silicate melts representative of terrestrial magmas and to assess how melt structure affects physical properties (like viscosity and density) and partitioning of trace to minor elements between melt and nucleating/growing mineral phases.

Europium represent one of the most studied trace element in the geochemical literature because of its ability to provide insights on the redox conditions and on the melting/crystallization history of magmatic rocks. However, remarkably there are only few data on the Eu speciation and structural environment in silicate glasses. A series of synthetic silicate glasses with compositions

representative of diverse terrestrial magma types have been studied by XAS at the Eu L3-edge by Cicconi et al. [Cicconi-09, Cicconi-12] providing information on the Eu reduction kinetics and drawing relationships between redox synthesis conditions, composition, and Eu speciation. Moreover, analysis of the EXAFS data collected on the same samples, allowed to characterise the Eu structural environment in these glasses highlighting the large differences in coordination geometry and bond distances between Eu^{2+} and Eu^{3+} species in the glass (Fig. ES1). These data have implications for explaining large variations of the Eu partition coefficients between magmas and crystallising mineral phases like plagioclases, clinopyroxenes and orthopyroxenes.

Fe K-edge XANES study of a glass produced during the first atomic bomb test at the Trinity site (Alamogordo, Mexico) [Giuli-10] allowed to determine the Fe redox along a transect (starting from the un-melted sand up to the free surface of the glass produced during the atomic bomb blast) allowing to ascertain that in that case, the instantaneous production of a large amount of silicate melt was not accompanied by a gradient of the Fe redox across the thickness of the produced melt. This process has interesting similarities to the tektite production process.

$\langle Eu^{3+}\text{-O}\rangle = 2.30 \pm 0.02$ Å

$\langle Eu^{2+}\text{-O}\rangle = 2.68 \pm 0.02$ Å
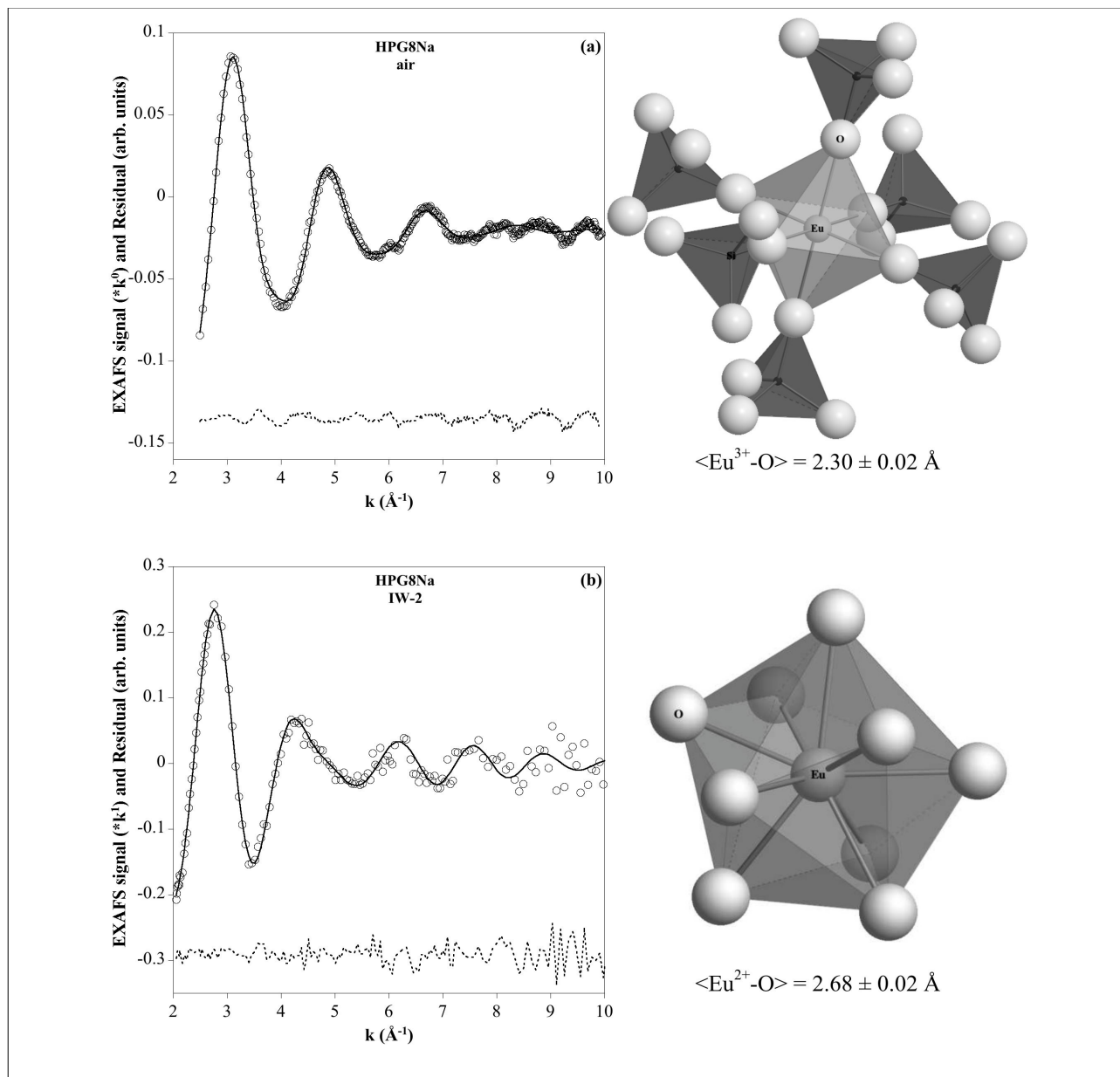
Figure ES1: Experimental (empty circles), theoretical (solid line), and residual (dashed line) Eu-EXAFS signals of the haplogranitic glasses synthesized in air (upper left panel) and under reducing conditions (at IW-2 buffer, lower left panel). On the right panels are shown the model structures used to calculate the theoretical contributions included in the fit. The large differences in the structural environment around Eu^{2+} and Eu^{3+} in the silicate glass/melt easily explains the preference of Eu^{2+} to enter the large site in the plagioclase structure instead of the smaller site in the clinopyroxene structure, which preferentially incorporates Eu^{3+} (smaller CN and shorter bond distances).

Environment

F. di Benedetto, Univ. Firenze

Environmental studies

This section groups several studies dealing with materials having environmental implications, or specifically with some health effects related to their interactions with the human body. Most of them pertain to the Earth Sciences community. The common aim of most of these studies can be devised in the determination of the potential toxicity of an element or a mineral phase in relation to its local structure, oxidation state, mobility in aqueous media, retention in poorly mobile phases. For these reasons, both XANES and EXAFS techniques were applied with success. The activity of many research groups in this field at the GILDA beamline was acknowledged in the general review of the environmental research at ESRF by Cotte et al. [Cotte-10]. Namely, GILDA beamline was cited in relation to its ability in providing insight on the fate of metallic contaminants in soils, plants, and microorganisms, and to the specific hot topic of the fate of As in the environment.

In the following, the scientific activity carried out in this field will be illustrated in two subsections,

a) contaminants in soils and rocks

A number of studies are related to this sub-topic. The most investigated subject deals with the identification of the valence state and local structure of Arsenic in several potential mineralogical hosts, in relation to its toxicity and mobility. Both Charlet and co-workers and Lattanzi and co-workers dealt with the identification of the occurrence of As(III) in solid phases pertaining to soils or sub-soil levels able to diffuse in the aquifers. Namely, Parsons et al. [Parsons-13] exploited the the cumulative effects of repetitive soil redox cycles on a calcareous fluvisol, the native microbial community and arsenic mobility following a simulated contamination event. In this context, the authors exploited through XANES a consistent As(III) presence, which however reduced during the redox cycling, because of a partial sequestration of As(V) species in slowly reacting solids. Bardelli et al. [Bardelli-11b] and Winkel et al. [Winkel-13] investigated travertines from Val di Pecora (Italy) and Chalkidiki (Greece), respectively, evidencing a relevant role played by calcite in the uptake of As from aqueous media. However, the first study indicated the occurrence of both As(III) and As(V) related to calcite, whereas the second only As(V). The differences in As valence states resides in the origin of the two travertine deposits. As bound to calcite is supposed to be removed from its geochemical cycle for significant time.

In a study by Chakraborty et al. [Chakraborty-11], the retention activity played by biotite with respect to the As(III) and As(V) species was explored. In particular, the mineral phase was found to significantly interact with the two As species, As(III) being bound through both bidentate mononuclear edge-sharing and bidentate binuclear corner-sharing inner sphere complexes. No redox activity at the mineral/pollutant interface was observed, thus suggesting biotite to play as a potential sink of As in reducing groundwater. Conversely changes in soil redox conditions and alteration of biotite (chemical and/or microbial weathering) may contribute to the occurrence of high As levels in groundwater.

The mobility of As was followed in the Acid Mine Drainage sediments related to the Tinto Santa Rosa acid stream (Iberian Pyritic Belt; SW, Spain) [Asta-10]. Aqueous As and Fe concentrations definitely drop down within 300 m downstream the source, suggesting iron minerals precipitation coupled with As uptake. A multianalytical spectroscopic study indicated As to occur mainly in the pentavalent state and the Fe phases involved in the As retention are Fe oxyhydroxides, as schwertmannite, goethite and jarosite, with evidence of interconversion of them in relation to the consolidation of the precipitate.

Related to the topic of the diffusion of As in the environment is also the study by Di Benedetto et al. [Dibenedetto-11], which deals with the valence states of As in the mineral enargite, Cu_3AsS_4, in relation to the understanding of the oxidation process of enargite. This process has, in fact, important implications for both environmental issues and mineral processing. The XANES study supports the "traditional" assignment of a monovalent state to Cu, and pentavalent to As. However, the strong similarity between the energy values of the As(V) edge in the sulfide, and of the As(III) oxides, suggest a preferred oxidation pathway towards the trivalent state during the alteration of the mineral.

Some studies were devoted to understand the physico-chemical and biological processes that govern Selenium bioavailability in the environment. In particular, the role of Fe-bearing minerals in reducing the Se(IV) and Se(VI) species was explored ([Chakraborty-10]; [Charlet-12]; [Kang-13]). Chakraborty et al. [Chakraborty-10] investigated the reductive immobilization of Se(IV) by micrometer-sized calcite, promoted by the redox activity of Fe(II) sorbed or co-precipitated at the carbonate surface. The reaction between the two redox species produces nanometer size needles of elemental Se at the mineral surface. (Fig. E1)
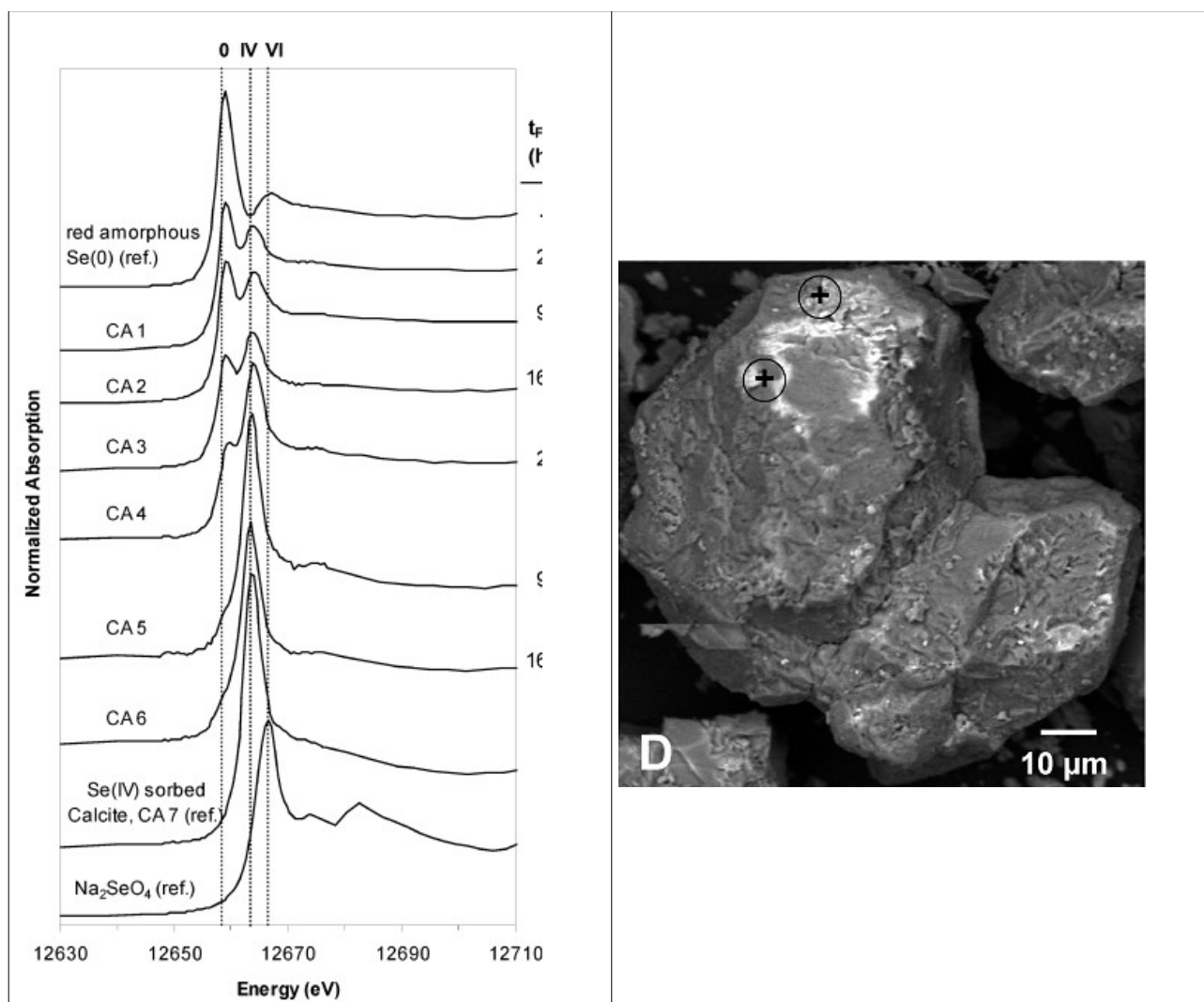
Figure E1: Left: XANES spectra of several micrometric calcite samples with FeII and SeIV sorbed on the surface. Some samples (CA1-to CA4) present a considerable amount of reduced Se0 species. Right: Electron microscopy image of one clacite grains with Se0 needles evidence d by the circles. Figures from [Chakraborty-10].

A successive study by Charlet et al. [Charlet-12] investigated the interaction between Se(IV) and Se(VI) solution with pyrite, FeS_2, and greigite, Fe_3S_4, in the form of nanoparticles. The XANES results undoubtedly reveal the presence of ferroselite, $FeSe_2$, thus pointing to the capability of the Fe(II) and Fe(III) species to reduce Se beyond its elemental state, also present in the batch reactors. A further step of the redox equilibria involving Se with environmental relevance was devised by Kang et al. [Kang-13], who studied the interaction between FeSe and $FeSe_2$ with aqueous Se(IV) and Se(VI). Results indicate that Se(0) is formed from the interaction between Se(IV) and the Fe(II) selenides, thus representing a process that compete with that proposed by [Charlet-12], highlighting also a specific role for Fe(III).

A study of the confinement of [79]Se for nuclear waste disposal was carried out by Bingham et al. [Bingham-11], who investigated by means of XANES and EXAFS the redox state and coordination of Se in alkali borosilicate glasses, conventionally used as confinement media before disposing the nuclear waste in the geological repositories. Results point to [79]Se occurring in alkali borosilicate glasses as Se^{4+} in SeO_3^{2-} selenite groups. Additional informations in relations to the differences in the melting procedure are provided.

Malherbe et al. [Malherbe-11] worked on a method able to quantify Cr(VI) directly in the solid state. This new approach was compared with the conventional extraction procedure (EPA Method 3060A), evidencing this latter method to systematically underestimate the Cr(VI) content in all studied samples. The coupling of the two methods is thus proposed to improve the EPA 3060A performance.

In three studies by Lattanzi et al. [Lattanzi-10a], [Lattanzi-10b] and Medas et al. [Medas-12] and of the group of Cagliari, the role of the hydrozincite, $Zn_5(CO_3)_2(OH)_6$, mineral in the uptake of heavy elements is deeply investigated.

The case of the Ingurtosu Pb–Zn mine (S-W Sardinia) is investigated. In this context, hydrozincite precipitation is associated to the drop down of aqueous concentration of Pb, Cd, Cu and Ni, and the characteristics of their uptake by hydrozincite are studied. Moreover, the site is markedly controlled by seasonal seasonal biomineralization processes. Cd, in particular is found to be weakly bound to hydrozincite as a disordered amorphous surface precipitate. The loose nature of the binding suggests a limited potential of hydrozincite as a control on the Cd mobility. In contrast, a stronger bond occurs between the mineral and Pb, which can be fixed in two modes: as a replacing ion for Zn in its tetrahedral site, or co-precipitated as a presumably amorphous phase, similar to cerussite. Hydrozincite is thus proposed as a potential sink for Pb.

A comprehensive review of the interaction of many pollutants with the environment and the geogenic materials is provided in the paper by Cuello et al. [Cuello-09]. In this study, some prominent results obtained by the use of the synchrotron radiation-based spectroscopy (and among them particularly XAS) are compared with the insights potentially obtainable with the use of neutron-based methods. These perspectives are critically analysed as far as concerns the mobility and interactions of pollutant in soils and in the field of the radioactive waste disposal.

b) contaminants in particulate matter

Some studies have been specifically designed to investigate the role of contaminants in the particulate matter (PM), in relation to the host mineral phases and to the diffusion in the environment.

The speciation of Fe and Mn in road dust particles in the peculiar context of the Traforo del San Bernardo highway tunnel was undertaken by means of XAS spectroscopy (Bardelli et al., [Bardelli-09a]; [Bardelli-11b], [Bardelli-11c]). The complicate and variable mineralogical assemblage of the airborne dusts was taken into account with the aid of a statistical approach (Principal Component Analysis) in analysing the spectral data. XAS analysis showed that Fe is mainly present as Fe_3O_4 and $FeCl_3$ forms, and the anthropic origin of these products was assessed.

Another study by Varrica et al. [Varrica-13] set the focus on the Sb speciation in PM and in residues of brake linings, brake pad wear, and road dust samples. XAS spectroscopy was able to ascertain the presence of Sb(III) and Sb(V) in different relative abundances. Brake linings turned out to be composed by Sb(III) oxide (Sb_2O_3) and stibnite (Sb_2S_3). A mechanism of contamination by stibnite and a successive reaction towards more stable Sb mixed oxide forms was thus inferred.

Another topic closely related to the diffuse PM concerns with the investigation of the metal content in the asbestos fibres, in relation to its toxicity for humans. This argument is a subject of two studies by Gualtieri et al. [Gualtieri-09] and by Giacobbe et al. [Giacobbe-10] , who studied the thermal denaturation of asbestos fibres at 1200 °C into non-fibrous crystalline phases. The evolution of the mineralogical phases during the thermal treatments were monitored thorugh time-resolved synchrotron radiation XRD [Gualtieri-09], in particular evidencing the appearance of some metastable phases. The coordination and valence state of Fe in this contexts were studied by XANES [Giacobbe-10]. With respect to the original chrysotile samples, where Fe is distributed between a paramagnetic phase and Fe_3O_4, at the end of the thermal treatment Fe is mostly contained in a phase, supposedly Fe-bearing akermanite-gehlenite, where it occurs tetrahedrally coordinated in the ferric state.

Cultural Heritage

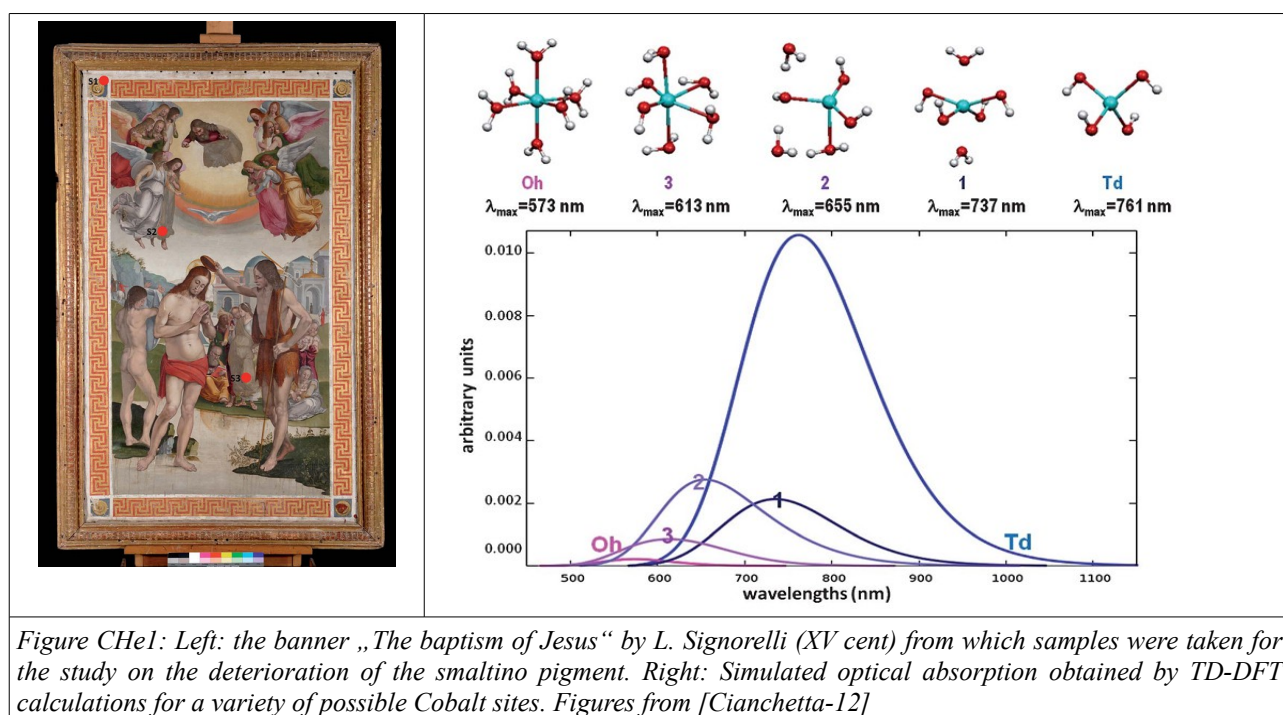*F. d'Acapito, CNR-IOM Grenoble*

Several studies in the field of Cultural Heritage have been conducted in the recent years at GILDA, mainly promoted by the Italian scientific community. These investigations have frequently been the outcome a tight collaboration between on one side scientists of the physics, chemistry and earth science area and on the other representatives of several art and conservation institutes (*Opificio delle pietre dure*, *Istituto Superiore del Restauro*, several *Soprintendenze per i beni archeologici*).

In particular, problems linked to chromophores and pigments have been addressed aiming to their chemical/physical characterization and to study their degradation. All the experiments carried out here are based on the fact that the chromatic response of a pigment is tightly linked to the symmetry, valence state and local geometry of the chromophore (usually a 3d metal). Thus, XAS reveals to be an ideal technique as it provides all this information by exploiting different regions (pre-edge, edge, XANES, EXAFS) of the same spectrum. In general, metals were added to production or painting materials with the aim of giving a particular hue to the manufact but they are present in limited amount, typically below 1 at%. For this reason, the use of fluorescence detection is of paramount importance, along with an intense X-ray beam, for the collection of high quality x-ray absorption spectra. The size of the beam of a few mm^2 did not represent a major limitation since studies were oriented towards macroscopic objects (namely ceramic decorations, mosaic tesserae, glass fragments) being in this way highly complementary to other instruments specialised on studies on the micro- and sub-micrometric scale. Also the lower area photon density respect to an undulator source (at least 10^4 less in terms of photons/mm^2) represented an advantage for samples potentially sensitive to radiation damage.

For the future it is planned the further development of experimental techniques made available by the recent use of standard ESRF control system (namely SPEC). In particular, the use of imaging techniques on large areas will be further exploited with the possibility of realizing elemental maps with valence state or symmetry selectivity.

The origin of the discoloration of the smaltino pigment has been addressed in Ref. [Cianchetta-12]. Smaltino is a potassium based glass additioned with Cobalt to obtain a deep blue color. It is known that with the effect of external agents this pigment can turn to a greyish hue. This study was carried out using fragments of the "Baptism of Jesus" banner by Luca Signorelli (XV

Cent.) and artificially aged specimens of smaltino prepared in laboratory. Scanning electron microscopy coupled with Energy dispersive X-ray Analysis found that Co remains in the degraded grains whereas K is found to leave these grains. The X-ray Absorption Spectroscopy analysis at the Co-K edge was carried out on fresh, artificially aged and original degraded specimens and the main result was that the degradation couples to the formation of 'octahedral-like' sites. The valence state of Co, on the other hand, was found to keep the 2+ value in both cases. The amount of "octahedral-like" sites is relatively low (30%) yet sufficient to change dramatically the hue of the grain. This meant that these sites must possess a high optical absorption cross section. In order to understand in more detail this process, *ab-initio* Time Dependent Density Functional Theory (TD-DFT) simulations were carried out based on the structures found with the XAS analysis. This, with the aim of determining the optical response of the structures and thus if the observed structural changes can be responsible for the color alteration. The results are shown in Fig. CHe1

Figure CHe1: Left: the banner „The baptism of Jesus" by L. Signorelli (XV cent) from which samples were taken for the study on the deterioration of the smaltino pigment. Right: Simulated optical absorption obtained by TD-DFT calculations for a variety of possible Cobalt sites. Figures from [Cianchetta-12]

From this analysis it is clear that regular octahedral sites (Oh) cannot be the exclusive responsible for the color degradation as the associated absorption is extremely low. Intermediate distorted "octahedral-like" structures (namely 2) are the best candidates as they possess at the same time a relatively high absorption cross section and an appreciable shift of the absorption maximum wavelength.

Another interesting application of *ab-initio* methods was reported in Ref. [Cartechini-11], in this case with the aim of simulating full EXAFS spectra. This work was devoted to understand if the "Naples Yellow" pigment (NY) found in renaissance maiolicas (in principle constituted of lead antimonate) could have been enriched on purpose with Zn of Fe to alter the chromatic effect. Indeed, previous studies have revealed increased content of Zn and Fe in these parts of the ceramic shed and a micro-Raman investigation has evidenced that both the metals could indeed enter the structure of the NY crystals. In order to evidence the actual incorporation site of these metals (in particular distinguishing the possible occurrence of Zn in the Sb site [Zn_{Sb}] or Zn in the Pb site [Zn_{Pb}]) in the NY, a XAS investigation was carried out at the Zn-K and Fe-K edges. In order to interpret the EXAFS analyses structural simulations based on Density Functional Theory (DFT) were also carried out and, based on the relaxed structures, theoretical EXAFS spectra were generated by averaging the frames of a DFT-based Molecular Dynamics (MD) cycle. The main results are shown in Fig. CHe2:
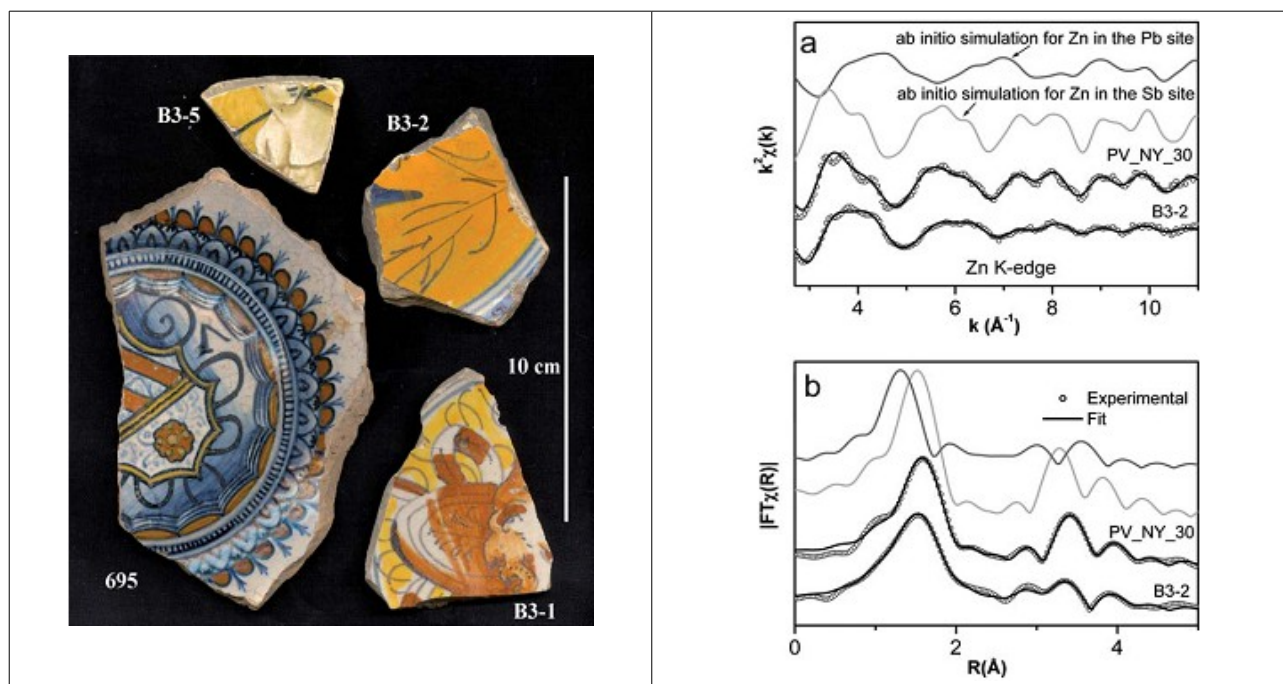

Figure CHe2: Left: image of the ceramic sheds used for the investigation in [Cartechini-11]. Right: experimental EXAFS data and related Fourier Transforms (open dots) relative to an original specimen (B3-2) and a laboratory prepared pigment (PV_NY_30). Superimposed are the best fit curves. In the upper part of the panels the EXAFS data generated with MD-DFT are shown for Zn in two possible sites, Zn_{Sb} (light grey) and Zn_{Pb} (dark gray).

Here it can be seen that Zn actually replaces Sb in the Lead Antimonate crystals and this is effectively assessed by the qualitative agreement between the experimental and the simulated data both in the laboratory specimen and on the original one. The Pb_{Zn} site would produce a completely different spectrum and the occurrence of this configuration was ruled out. The quantitative comparison between the structural data derived from EXAFS and those from the DFT modeling were in close agreement for Sn_{Zn} and completely different (namely for the first shell bond length) for the Pb_{Zn} site. The investigation on Fe gave a similar response for the laboratory specimen whereas the original ceramic did not agree to this interpretation presumably to the fact that Fe is also present in other portions of the shed, in particular in the underlying *terra-cotta* support.

A series of studies have been dedicated to the link between color and valence state of Fe and Mn in Roman [Gliozzo-13, Gliozzo-10, Arletti-11] and medieval/Byzantine [Arletti-13, Arletti-10] glasses. The samples investigated in these studies presented the advantage of containing a relatively high amount of Fe and Mn (0.1-1 at %) whereas other known chromophores (Cu, Co) were at ppm levels thus making clearer the role of these elements in the final color. In these studies a considerable work was carried out on the analysis of the resonances present in the pre-edge zone ascribed to 1s-3d transitions and known to contain rich information about local symmetry and valence state of the metal. As a general procedure, it is known that Fe-bearing glasses were added with Mn to promote Fe oxidation to Fe^{3+} and de-color the manufact. Predominantly, Fe is actually found in 3+ state whereas Mn is present in the 2+ state. The partial presence of Fe^{2+} was found to determine the final hue of the object. Glassware fragments from the Thamusida site (Morocco, [Gliozzo-13]) revealed a link between the residual Fe^{2+} content and the coloration: between 30 and 52% of the total Fe content the color is aqua blue whereas for lower amounts the manufact turns light green. The predominant phase of Fe^{3+} and Mn^{2+} states was also assessed in [Arletti-10, Arletti-11, Arletti-13] where the role of Mn as decoloring agent was stressed. This element was added to glasses as mineral Pyrolusite (Mn^{4+}) and its reduction to Mn^{2+} led to the oxidation of Fe. Small amounts of Mn^{3+} were also detected in some specimen but using the more sensitive technique of UV-Vis absorption, XAS being not sufficiently accurate to detect such low amounts of this species. Less clear appeared to be the situation in the mosaic panels of the Faragola site [Gliozzo-10] where the presence of Cu at about 1% level played a role in the coloration of green and blue tesserae. Indeed the presence of Cu in the +2 state was interpreted as the main coloring agent for these specimens even in presence of Fe in the 3+ state.

A more clear scenario was found in the case of copper based tesserae studied in [Gliozzo-10] and [Silvestri-12]. In the case of Cu it is not possible to exploit the pre-edge peaks as the filling of the d states is complete (Cu^+, $3d^{10}$) or almost complete (Cu^{2+}, $3d^9$) so the intensity of these peaks is null or extremely reduced. On the other hand, the technique for distinguishing one valence state from the other can be based on the analysis of the edge region (a resonance at 8982 eV it particularly strong in Cu^+ bearing glasses), on the edge position (the inflection point is at 8979 n Cu^0, 8981 in Cu^+ and 8984 eV in Cu^{2+}) and on the Cu-O typical distances that range around 1.82-1.85 Ang in Cu^+ and 1.93 in Cu^{2+} cases. In mosaic tesserae analyzed in [Silvestri-12] it was found that the deep red hue was due to nanoparticles of metallic Cu whereas the orange color was due to crystals of Cu_2O. In more oxidizing conditions the state of Cu switches to an equilibrium between Cu^+ and Cu^{2+}: as the isolated Cu^+ ion is non coloring (having a $3d^{10}$ electronic configuration) Cu^{2+} can lead to green/blue color and [Silvestri-12] found a correlation between the intensity of the color and the content of Cu^{2+}. The role of Cu^{2+} in providing a green coloration has also been evidenced in Sicilian Renaissance pottery [Crupi-10]. The role of Fe and Mn was also studied by the same group [Bardelli-11] in ceramic decorations in medieval Sicilian manufacts finding both metals in the 3+ state.

A final work used X-ray Diffraction, Proton Induced X-ray Emission and micro-Raman in order to characterize a collection of gemstones from the Palatine Hill in Rome [Gliozzo-11]. Following the structure determined by XRD the gemstones were divided as chalcedonies, jaspers, and other minerals even if this characterization did not provide sufficient elements to determine the origin of the raw materials.

Health, medicine and life science

S. Mangani, Univ. Siena

The experimental setup of the GILDA beamline has allowed the completion of a series of X-ray absorption spectroscopy (XAS) studies on different biological systems. These investigations have studied metal ion binding in different systems spanning from the interaction of metal-based drugs with proteins, to metal binding in lipids and classical studies on metal binding sites in proteins. The experimental approaches range from the classical use of the XAS technique to study relevant biochemical problems (see for example the paper of Banci et al.) to new methodological applications of XAS (see the paper from Giachini et al.) that highlight the potentiality of the technique. The results have been published on journal of high to medium-high impact factor evidencing the high quality of the data collected and the versatility of the beamline.

XAS is an established and powerful technique in structural biology, because of its capability to provide very accurate information about the local structure of a metal ion in intrinsically diluted systems like metal-containing biological macromolecules. In front of the disadvantage to be limited, in practice, to give radial information on the metal coordination, the XAFS use in studying biological systems has several advantages:

1. the possibility to obtain structural information independently of the physical state (crystalline, amorphous or liquid) of the sample.

2. the unique capability of the technique to independently determining the environment of different atom types present in the same sample and obtain, at the same time, information on the electronic structure of the atom of interest (oxidation state, coordination geometry) by exploiting the different regions of the XAS spectrum (pre-edge, edge, XANES, EXAFS) in a synergistic way.

3. the high-resolution of the local structure of a metal ion embedded in a biological macromolecule renders XAS synergistic to other lower-resolution techniques like EPR or NMR (mainly) and (in some cases) X-ray crystallography.

4. synergism between XAS and ab-initio theoretical calculations applied to complex systems of unknown structure.

The papers reporting the results obtained from the data collected at GILDA are summarized below in descending order of appearance in the literature.

An EXAFS study of the binding of Cd and Pb ions to lipid films [Bergamino-13]

This paper reports Extended X-ray Absorption Fine Structure (EXAFS) measurements performed on Langmuir-Blodgett (LB) films containing cadmium and lead ions. The study reveals the different coordination structures of the two cations in lipid membranes. LB films have been prepared with stearic and 1,2 distearoyl-Lα-phosphatidic acids. The measurements have been performed on films of two different thicknesses, one and seven molecular layers, and at two different values of relative humidity. The local atomic environment of Cd ions in stearate films is consistent with unidentate coordination in which a Cd ion binds two stearate molecules, while that of Pb ions is consistent with a bidentate coordination in which a Pb ion binds only one stearate molecule. Furthermore, in lead stearate films, the presence of Pb clusters has been observed.

Interaction of cisplatin with human superoxide dismutase [Banci-12]

The study is an example of the synergism mentioned before as XAS has been used coupled to X-ray crystallography and NMR spectroscopy to prove that the interaction of *cis*-diamminedichloroplatinum(II) (cisplatin) with human superoxide dismutase (hSOD1) observed in the crystal is maintained in solution. This work demonstrates that cisplatin inhibits aggregation of demetalated oxidized hSOD1, and it is further able to dissolve and monomerize oxidized hSOD1 oligomers in vitro and in cell, thus indicating its potential use as a leading compound for treating amyotrophic lateral sclerosis (ALS syndrome).
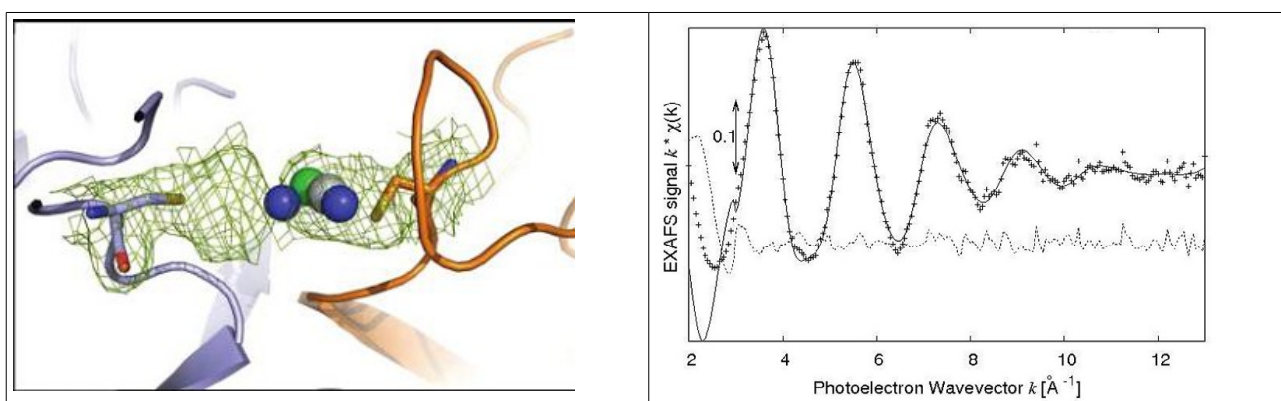

Figure HML1: Left: Crystal structure of cisplatin-bound apo hSOD1. Ribbon representation of one of the two dimers present in the asymmetric unit highlighting the two Cys111 facing each other at the interface and the cisplatin bound to one of them (N, blue; Pt, gray; Cl, green). Right: EXAFS data collected in acqueous solution., best fit curve and residue that confirm the structure found in the crystal form. Figures from [Banci12 and related Supporting Informations].

X-ray absorption spectroscopy studies of the adducts formed between cytotoxic gold compounds and two major serum proteins [Messori-11]

The work reported in this paper provides a nice example of the complementary information obtainable from the different regions of the XAS spectrum. Both X-ray absorption near-edge spectroscopy (XANES) and extended X-ray absorption fine structure (EXAFS) have been used to gain insight into the nature of the adducts formed between three representative gold(I, III) metallodrugs (i.e., auranofin; [Au(2,20-bipyridine)(OH)$_2$] PF$_6$:Aubipy; dinuclear [Au$_2$(6,60-dimethyl-2,20- bipyridine)$_2$(l-O)$_2$](PF$_6$)$_2$: Auoxo6) and two major plasma proteins: bovine serum albumin (BSA) and human serum apotransferrin (apoTf). XANES spectra revealed that auranofin, upon protein binding, conserves its gold(I) oxidation state. Protein binding most probably takes place through release of the thiosugar ligand and its subsequent replacement by a thiol (or a thioether) from the protein. This hypothesis is independently supported by EXAFS results. In contrast, the reactions of Aubipy with serum albumin and of Auoxo6 with serum apoTf invariantly result in gold(III) to gold(I) reduction. Gold(III) reduction, clearly documented by XANES, is accompanied, in both cases, by release of the bipyridyl ligands. For Auoxo6 cleavage of the gold–gold dioxo bridge is also observed. Gold(III) reduction leads to formation of protein bound gold(I) species, with deeply modified metal coordination environments, as evidenced by EXAFS. In these adducts, the gold(I) centers are probably anchored to the protein through nitrogen donors.

X-Ray absorption spectroscopy quantitative analysis of biomimetic copper(II) complexes with tridentate nitrogen ligands mimicking the *tris*(imidazole) array of protein centres [Borghi-10]
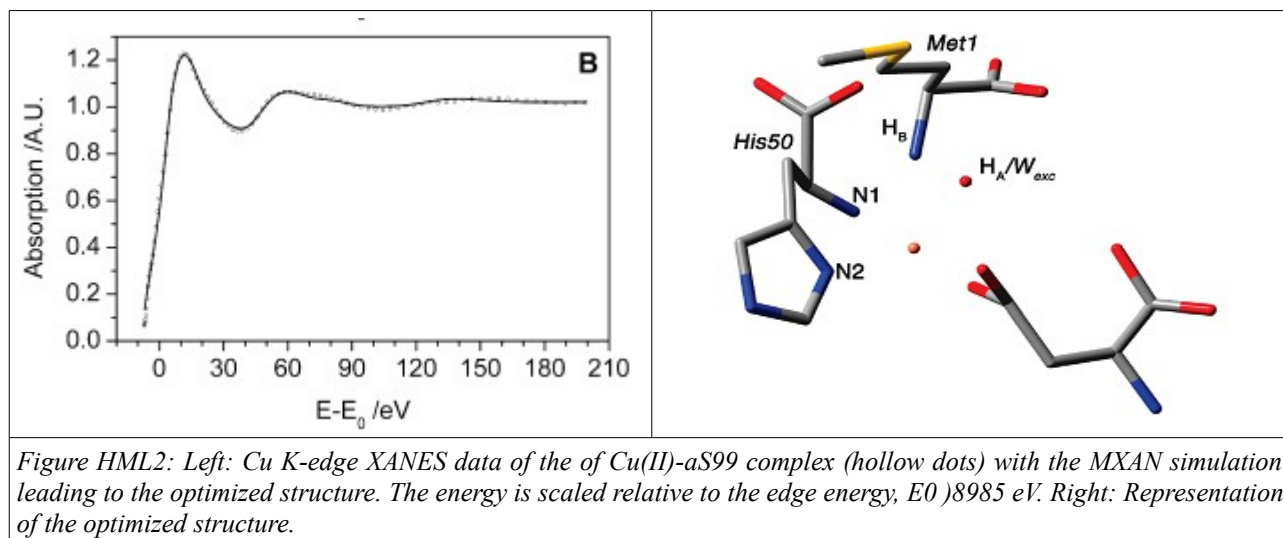
In this study copper(II) complexes with the tridentate nitrogen ligand bis[2-(1-methylbenzimidazol-2-yl)ethyl]amine (2-BB) are considered as model compounds for the Cu-tris(imidazole) array found in several copper proteins. 2-BB chelates copper(II) forming two six-membered rings and the complexes contain methanol, nitrite, azide and water as ancillary ligands; both the coordination numbers and stereochemistries differ in these complexes. Their key structural features were investigated by using full multiple-scattering theoretical analysis of the copper K-edge X-ray absorption spectrum with the MXAN code. The authors show that using cluster sizes large enough to include all atoms of the ligand, the analysis of the XANES region can give both a structural model of the metal centre and map the structure of the 2-BB complexes. Complex [Cu(2-BB)(N$_3$)]$^+$ provided a critical test through the comparison of the XANES simulation results with crystallographic data, thus permitting the extension of the method to the complex [Cu(2-BB)(H$_2$O)$_n$]

[+] (n = 1 or 2), for which crystallographic data are not available but is expected to bear a five-coordinated Cu(3N)(2O) core (n = 2). The structural data of [Cu(2-BB)(MeOH)(ClO$_4$)]$^+$ and [Cu(2-BB)(NO$_2$)]$^+$, both with a Cu(3N)(2O) core but with a different stereochemistry, were used as the starting parameters for two independent simulations of the XANES region of the [Cu(2-BB)(H$_2$O)$_2$]$^+$ cation. The two structural models generated by simulation converge towards a structure for the aqua-cation with a lower coordination number. New calculations, where four-coordinated Cu(3N)(O) cores were considered as the starting structures, validated that the structure of the aqua-complex as powder has a copper(II) centre with a four-coordinated Cu(3N)(O) core and a molecular formula [Cu(2-BB)(H$_2$O)](ClO$_4$)·(H$_2$O). A water solvation molecule, presumed to be disordered from the simulations with the two Cu(3N)(2O) cores, is present. The successful treatment of this Cu-2-BB complex system allows the extension of the method to other biomimetic compounds when a structural characterization is lacking.

Structural characterization of a high affinity mononuclear site in the copper(II)-a-synuclein complex [Bortolus-10]

This work exploits a combination of Electron Paramagnetic Resonance spectroscopic techniques (EPR, CW-EPR, pulsed-EPR, pulsed-ENDOR, HYSCORE) and XANES have been employed to study the binding of Cu(II) to a truncated form of Human α-Synuclein (αS99: residues 1-99) to elucidate the residues involved in the binding site and the role of copper ions in the protein oligomerization. αS is a 140 amino acid protein that is the main constituent of Lewy bodies, the cytoplasmatic deposits found in the brains of Parkinson's disease patients, where it is present in an aggregated, fibrillar form. The results of both multifrequency continuous wave experiments and pulsed experiments at X-band and the comparison of 9.5 and 95 GHz data showed that at pH 6.5 only one copper binding mode is present the Cu(II)-αS99 complex. To identify the nature of the ligands, electron Spin Echo Envelope Modulation, Hyperfine Sublevel Correlation Spectroscopy, and pulsed Davies Electron-Nuclear Double Resonance (Davies-ENDOR) experiments were performed. The obtained EPR parameters are typical of a type-II copper complex, in a slightly distorted square planar geometry. The combined results from the different pulsed techniques provide evidence that the equatorial Cu(II) ligands are an imidazole nitrogen, a deprotonated amido backbone nitrogen, attributed to His50, an exchangeable water molecule, and oxygen from an unidentified ligand. The participation of the free amino terminus (Met1) to the complex as an axial ligand is also proposed. The MXAN analysis of the XAS Kedge absorption allowed the authors to

independently validate the structural features proposed on the basis of the magnetic parameters of the Cu(II)-αS99 complex and then to further refine the quality of the proposed structural model (Fig. HML2).

Figure HML2: Left: Cu K-edge XANES data of the of Cu(II)-aS99 complex (hollow dots) with the MXAN simulation leading to the optimized structure. The energy is scaled relative to the edge energy, E0)8985 eV. Right: Representation of the optimized structure.

Synergic approach to XAFS analysis for the identification of most probable binding motifs for mononuclear zinc sites in metalloproteins [Giachini-10]

This work presents an interesting data analysis approach, based on XAFS data to identify the most probable binding motifs of unknown mononuclear zinc sites in metalloproteins. This approach combines multiple-scattering EXAFS analysis performed within the rigid-body refinement scheme, non muffin-tin ab initio XANES simulations, average structural information on amino acids and metal binding clusters provided by the Protein Data Bank, and Debye–Waller factor calculations based on density functional theory. The efficacy of the method is tested by using three reference zinc proteins of known crystal structure. To show the applicability of the method to unknown structures, not deposited in the Protein Data Bank, the XAFS spectra of six mononuclear zinc binding sites present in membrane proteins were collected and analyzed. By comparing the Zn K-edge XAFS features exhibited by these proteins with those of the reference structures, key spectral characteristics, related to specific binding motifs, have been identified supporting the validity of the proposed method. This publication stems from the PhD thesis work of G. Veronesi at the University of Bologna.

Ab initio analysis of the x-ray absorption spectrum of the myoglobin‐carbon monoxide complex [Veronesi-10]

This paper presents a comparison between Fe K-edge X-ray absorption spectra of carbonmonoxy–myoglobin simulated by curved-wave multiple-scattering theory and the simulation of its atomic and vibrational structure based on density-functional theory. This work aims to exploit the possible synergy between the experimental XANES and computational DFT approaches for determining the atomic and vibrational structure of a metalloprotein. The case of MbCO is particularly interesting because of its biological relevance and because taking into account the vibrational damping of the many strong multiple scattering (MS) contributions reliably and correctly is the subject of current research. This work shows that excellent comparison between experiment and simulations is obtained without the need of any structural fitting parameters as far as the contributions to the spectra of the heme plane and the proximal histidine are concerned. The work also shows that simulations are essential to determine the geometry of the CO ligand, illustrating how notable improvements can be obtained with this synergistic approach to data analysis .

X-ray absorption studies of Zn2+-binding sites in *Escherichia coli* transhydrogenase and its ßH91K mutant [Veronesi-10b]

Zn K-edge X-ray absorption fine structure (XAFS) has been used to determine the local structure of Zn(II) bound to *Escherichia coli* transhydrogenase. Transhydrogenase couples hydride transfer between NADH and NADP(+) to proton translocation across a membrane. The binding of Zn(II) inhibits the steps associated with proton transfer with a mechanism to be ascertained. XAFS experiments have been performed on wild-type enzyme and on a mutant in which βHis91 was replaced by Lys (βH91K). This well-conserved His residue, located in the membrane-spanning domain of the protein, has been suggested to function in proton transfer, and to act as a ligand of the inhibitory Zn(II). The XAFS analysis has identified a Zn(II)-binding site formed by one Cys, two His, and one Asp/Glu residue, arranged in a tetrahedral geometry. The structure of the site is consistent with the notion that Zn(II) inhibits proton translocation by competing with H^+ binding to the His residues. The same cluster of residues with very similar bond lengths best fits the spectra of wild-type transhydrogenase and βH91K demonstrating that βHis91 is not directly involved in Zn(II) binding. These findings indicate that the loci of βHis91 and of the Zn(II)-binding site, although both on (or close to) the proton-transfer pathway of transhydrogenase, are spatially separate.

Potential antitumor gold drugs: DFT and XANES studies of local atomic and electronic structure [Soldatov-09]

     This Conference Proceeding reports about an investigation of the local atomic and electronic structure of the potential antitumor agent gold(III) complex Au(bipy)(OH)$_2$. Geometry structure optimization of Au(bipy)(OH)$_2$ was carried out by means of density functional theory (DFT) simulations and compared to the experimental Au L3-edge X-ray absorption near edge structure (XANES) spectrum of the compound. The Au L3-XANES spectra of the gold(III) complex were simulated using both the self-consistent real-space full multiple scattering theory within the muffin-tin approximation for the potential shape and the full-potential finite difference method. DFT simulations in relativistic approach show the most probable structure for Au(bipy)(OH)$_2$ in a good agreement with XANES data analysis. The approach allows to define the exact local atomic structure of the gold(III) complex by two independent methods.

Acknowledgements

References

Generic References

[Belin-05] Belin S., Briois V., Traverse A., Idir M., Moreno T., Ribbens M., Physica Scripta. Vol. T115, 980–983, (2005) http://www.synchrotron-soleil.fr/portal/page/portal/Recherche/LignesLumiere/SAMBA.

[Benzi-08] Benzi F., Davoli I., Rovezzi M., d'Acapito F., Rev. Sci. Instrum. 79, 103902 (2008).

[Bonanni-08] Bonanni A., Navarro-Quezada A., Tian Li, Wegscheider M., Matěj Z., Holý V., Lechner R. T., Bauer G., Rovezzi M., d'Acapito F., Kiecana M., Sawicki M., Dietl T., Phys. Rev. Lett. 101, 135502 (2008).

[Boscherini-14] Boscherini F. in *X-ray Absorption Spectroscopy of Semiconductors*, Schnor C. and Ridgway M. eds., Springer (to appear in 2014).

[Boscherini-15] Boscherini F. in *XAS and XES: theory and applications*, C. Lamberti and van Bokhoven J. A. eds., John Wiley and Sons (to appear in 2015).

[CARD-12] http://www.esrf.fr/computing/scientific/CARD/CARD.html.

[Cesca-14] Cesca T., Kalinic B., Maurizio C., Scian C., Battaglin G., Mazzoldi P., Mattei G., Nanoscale 6 1716-1724 (2014).

[Cesca-13] Cesca T., Maurizio C., Kalinic B., Scian C., Trave E., Battaglin G., Mazzoldi P., Mattei G., Nucl. Instr. Meth. B (2013), in press.

[Ciatto-04] Ciatto G., d'Acapito F., Boscherini F. and Mobilio S., J. Synchrotron Radiation 11, 278 (2004).

[CLAESS] https://www.cells.es/Beamlines/CLAESS/

[Costanzo-14] Costanzo T., Benzi F., Ghigna P., Pin S., Spinolo G., d'Acapito F., J. Synchrotron Rad. 21, 395-400 (2014).

[Dacapito-03] d'Acapito F., Davoli I., Ghigna P., Mobilio S., J. Synchrotron Radiat. 10, 260 (2003).

[Dacapito-07] d'Acapito F., Milita S., Satta A., Colombo A., J. Appl. Phys. 102, 043524 (2007).

[Dacapito-14] d'Acapito F., "*III-V and II-VI nanowires and rods*" in *X-ray Absorption Spectroscopy of Semiconductors*, Schnor C. and Ridgway M. eds., Springer (to appear in 2014).

[Dacapito-98] d'Acapito F., Colonna S., Pascarelli S., Antonioli G., Balerna A., Bazzini A., Boscherini, Campolungo F., Chini G., Dalba G., Davoli I., Fornasini P., Graziola R., Licheri G.,

Meneghini, Rocca F., Sangiorgio L., Sciarra V., Tullio V., Mobilio S., ESRF Newsletter 30, 42 (1998).

[Dent-09] Dent A. J., Cibin G., Ramos S., Smith A. D., Scott S. M., Varandas L., Pearson M. R., Krumpa N. A., Jones C. P., Robbins P. E., Journal of Physics: Conference Series 190 012039 (2009).

[Dicicco-09] Di Cicco A., Aquilanti G., Minicucci M., Principi E., Novello N., Cognigni A., Olivi L., Journal of Physics: Conference Series 190 012043 (2009).

[DIFFABS] http://www.synchrotron-soleil.fr/portal/page/portal/Recherche/LignesLumiere/DIFFABS

[ESRF white book] ESRF UPGRADE PROGRAMME PHASE II (2015-2019) WHITE PAPER available at http://www.esrf.fr/news/general/latticeupgrade

[Filipponi-00] Filipponi A., Borowski M., Bowron D. T., Ansell S., Di Cicco A., De Panfilis S., Itie J.-P., Rev. Sci. Instrum. 71, 2422 (2000).

[Giubertoni-08] Giubertoni D., Pepponi G., Gennaro S., Bersani M., Sahiner M.A., Kelty S. P., Doherty R., Foad M.A., Kah M., Kirby K.J., Woicik J.C., Pianetta P., J. Appl. Phys. 104, 103716 (2008).

[Jamet-06] Jamet M., Barski A., Devillers T., Poydenot V., Dujardin R., Bayle-Guillemaud P., Rothman J., Bellet-Amalric E., Marty A., Cibert J., Mattana R., Tatarenko S., Nat. Mater. 5, 653 (2006).

[Lai-86] Lai B., Cerrina F., Nucl. Instrum. Methods, A246 337-341 (1986).

[Maurizio2014] Maurizio C., Cesca T., Trapananti A., Kalinic B., Scian C., Mazzoldi P., Battaglin G., Mattei G., Nucl. Instr. Meth. B, in press (2014)

[Mcdowell-04] MacDowell A. A., Celestre R. S., Howells M., McKinney W., Krupnick J., Cambie D., Domning E. E., Duarte R. M., Kelez N., Plate D. W., Cork C. W., Earnest T. N., Dickert J., Meigs G., Ralston C., Holton J. M., Alber T., Berger J. M., Agarde D. A., Padmorea H. A., J. Synchrotron Rad. 11 447-455 (2004).

[Pascarelli-96] Pascarelli S., Boscherini F., D'acapito F., Hrdy J., Meneghini C., Mobilio S., J. Synchrotron Rad. 3 147 (1996).

[Proux-05] Proux O., Biquard X., Lahera E., Menthonnex J.-J., Prat A., Ulrich O., Soldo Y., Trevisson P., Kapoujyan G., Perroux G., Taunier P., Grand D., Jeantet P., Deleglise M. , Roux J-P. and Hazemann J-L., Physica Scripta. Vol. T115, 970–973 (2005).

[Rovezzi-08] Rovezzi M., Devillers T., Arras E., d'Acapito F., Barski A., Jamet M., Pochet P., Applied Physics Letters 92, 242510 (2008).

[Scheinhost-09] Scheinost A., *"Upgrade of X-ray optics at the Rossendorf Beamline (BM20), European Synchrotron Radiation Facility*, 02.09.FWR"* July 2009.

[Tullio-01] Tullio V., D'Anca F., Campolungo F., d'Acapito F., Boscherini F., Mobilio S., *"Vibrating sample holder for x-ray absorption measurements on single crystals"*, INFN-LNF Internal Note LNF-01/020 (NT) 4 May 2001.

GILDA 2009-2013 Publications

[Arletti-13] Arletti R., Quartieri S., Freestone I.C., Applied Physics A 111 99-108 (2013).

[Aurelio-13] Aurelio G., Bardelli F., Prado R.J., Sánchez R.D., Saleta M.E., Garbarino G., Chemistry of Materials 25 3307-3314 (2013).

[Balerna-13] Balerna A., Evangelisti C., Schiavi E., Vitulli G., Bertinetti L., Martra G., Mobilio S., Journal of Physics: Conference Series 430 012052-1-012052-4 (2013).

[Bergamino-13] Bergamino M., Relini A., Rispoli P., Giachini L., Rolandi R., European Physical Journal E 36 102-1-102-7 (2013).

[Biagioni-13] Biagioni C., Bonaccorsi E., Merlino S., Bersani D., Cement and Concrete Research 49 48-54 (2013).

[Bordiga-13] Bordiga S., Groppo E., Agostini G., van Bokhoven J.A., Lamberti C., Chemical Reviews 113 1736-1850 (2013).

[Centomo-13] Centomo P., Meneghini C., Zecca M., Review of Scientific Instruments 84 054102-1-054102-5 (2013).

[Dacapito-13] d'Acapito F., Pochet P., Somma F., Aloe P., Montereali R.M., Vincenti M.A., Polosan S., Applied Physics Letters 102 081107-1-081107-4 (2013).

[Dibenedetto-13] Di Benedetto F., d'Acapito F., Bencista I., Luca A., Fornaciai G., Frizzera S., Innocenti M., Montegrossi G., Pardi L.A., Romanelli M., Physica Status Solidi (c) 10 1055-1057 (2013).

[Giglio-13] Gigli L., Arletti R., Quartieri S., Di Renzo F., Vezzalini G., Microporous and Mesoporous Materials 177 8-16 (2013).

[Gliozzo-13] Gliozzo E., Santagostino Barbone A., d'Acapito F., Archaeometry 55 609-639 (2013).

[Kang-13] Kang M., Ma B., Bardelli F., Chen F., Liu C., Zheng Z., Wu S., Charlet L., Journal of Hazardous Materials 248-249 20-28 (2013).

[Leardini-13] Leardini L., Martucci A., Cruciani G., Microporous and Mesoporous Materials 173 6-14 (2013).

[Luches-13] Luches P., Pagliuca F., Valeri S., Boscherini F., Physical Chemistry C 117 1030-1036 (2013).

[Minguzzi-13] Minguzzi A., Lugaresi O., Locatelli C., Rondinini S., d'Acapito F., Achilli E., Ghigna P., Analytical Chemistry 85 7009-7013 (2013).

[Mohiddon-13] Mohiddon M.A., Naidu K.L., Dalba G., Rocca F., Krishna M.G., AIP Conference Proceedings 1512 686-687 (2013).

[Monteiro-13] Monteiro G., Santos L.F., Almeida R.M., d'Acapito F., Journal of Non-Crystalline Solids 377 129-136 (2013).

[Moretti-13] Moretti A., Giuli G., Nobili F., Trapananti A., Aquilanti G., Tossici R., Marassi R., Journal of the Electrochemical Society 160 A940-A949 (2013).

[Naidu-13] Naidu K.L., Mohiddon M.A., Krishna M.G., Dalba G., Rocca F., Journal of Physics : Conference Series 430 012035-1-012035-4 (2013).

[Niu-13] Niu G., Zoellner M.H., Zaumseil P., Pouliopoulos A., d'Acapito F., Schroeder T., Boscherini F., Journal of Applied Physics 113 043504-1-043504-6 (2013).

[Parsons-13] Parsons C.T., Couture R.M., Omoregie E.O., Bardelli F., Grenèche J.M., Román-Ross G., Charlet L., Environmental Pollution 178 254-263 (2013).

[Pin-13a] Pin S., Suardelli M., d'Acapito F., Spinolo G., Zema M., Tarantino S.C., Barba L., Ghigna P., Journal of Physical Chemistry C 117 6113-6119 (2013).

[Pin-13b] Pin S., Suardelli M., d'Acapito F., Spinolo G., Zema M., Tarantino S.C., Ghigna P., Journal of Physical Chemistry C 117 6105-6112 (2013).

[Pompeo-13] Pompeo N., Torokhtii K., Meneghini C., Mobilio S., Loria R., Cirillo C., Ilyina E.A., Attanasio C., Sarti S., Silva E., Journal of Superconductivity and Novel Magnetism 26 1939-1943 (2013).

[Ramamoorthy-13] Ramamoorthy R.K., Bhatnagar A.K., Vachhani P.S., Dalba G., Grisenti R., Mattarelli M., Montagna M., Armellini C., Rocca F., Journal of Physics: Conference Series 430 012089-1-012089-4 (2013).

[Sipr-13] Sipr O., Vackar J., Vachhani P.S., Ramamoorthy R.K., Dalba G., Bhatnagar A.K., Rocca F., Journal of Physics: Conference Series 430 012128-1-012128-6 (2013).

[Taglieri-13] Taglieri G., Mondelli C., Daniele V., Pusceddu E., Trapananti A., Advances in Materials Physics and Chemistry 3 108-112 (2013).

[Varrica-13] Varrica D., Bardelli F., Dongarrà G., Tamburo E., Atmospheric Environment 64 18-24 (2013).

[Winkel-13] Winkel L.H.E., Casentini B., Bardelli F., Voegelin A., Nikolaidis N.P., Charlet L., Geochimica et Cosmochimica Acta 106 99-110 (2013).

[Arras-12] Arras E., Lancon F., Slipukhina I., Prestat E., Rovezzi M., Tardif S., Titov A., Bayle-Guillemaud P., d'Acapito F., Barski A., Favre-Nicolin V., Jamet M., Cibert J., Pochet P., Physical Review B 85, 115204 (2012).

[Banci-12] Banci L., Bertini I., Blazevits O., Calderone V., Cantini F., Mao J., Trapananti A., Vieru M., Amori I., Cozzolino M., Carri M.T., Journal of the American Chemical Society 134 7009-7014 (2012).

[Bardelli-12] Bardelli F., Barone G., Crupi V., Longo F., Maisano G., Majolino D., Mazzoleni P., Venuti V., Journal of Synchrotron Radiation 19 782-788 (2012).

[Battocchio-12] Battocchio C., Meneghini C., Fratoddi I., Venditti I., Russo M.V., Aquilanti G., Maurizio C., Bondino F., Matassa R., Rossi M., Mobilio S., Polzonetti G., Journal of Physical Chemistry C 116 19571-19578 (2012).

[Boscherini-12] F. Boscherini in *Characterization of Semiconductor Heterostructures and Nanostructures*, 2nd edition, C. Lamberti and G. Agostini eds., Elsevier (2012).

[Cesca-12] Cesca T., Maurizio C., Kalinic B., Perotto G., Mazzoldi P., Trave E., Battaglin G., Mattei G., Optics Express 20 16639-16649 (2012).

[Charlet-12] Charlet L., Kang M., Bardelli F., Kirsch R., Géhin A., Grenèche J.M., Chen F., Environmental Science and Technology 46 4869-4876 (2012).

[Cianchetta-12] Cianchetta I., Colantoni I., Talarico F., d'Acapito F., Trapananti A., Maurizio C., Fantacci S., Davoli I., Journal of Analytical Atomic Spectrometry 27 1941-1948 (2012).

[Cicconi-12] Cicconi M.R., Giuli G., Paris E., Ertel-Ingrisch W., Ulmer P., Dingwell D.B. , American Mineralogist 97 918-929 (2012).

[Dacapito-12] d'Acapito F., Rovezzi M., Boscherini F., Jabeen F., Bais G., Piccin M., Rubini S., Martelli F., Semiconductor Science and Technology 27 085001-1-085001-6 (2012).

[Depadova-12] De Padova P., Olivieri B., Mariot J.M., Favre L., Berbezier I., Quaresima C., Paci B., Generosi A., Rossi Albertini V., Cricenti A., Ottaviani C., Luce M., Testa A.M., Peddis D., Fiorani D., Scarselli M., De Crescenzi M., Heckmann O., Richter M. C. , Hricovini K, d'Acapito F., Journal of Physics Condensed Matter 24 142203-1-142203-5 (2012).

[Devilliers-12] Devillers T., Rovezzi M., Gonzalez Szwacki N., Dobkowska S., Stefanowicz W., Sztenkiel D., Grois A., Suffczynski J., Navarro-Quezada A., Faina B., Li T., Glatzel P., d'Acapito F., Jakiela R., Sawicki M., Majewski J.A., Dietl T., Bonanni A., Scientific Reports 2 722-1-722-6 (2012).

[Erra-12] Erra L., Tedesco C., Immediata I., Gregoli L., Gaeta C., Merlini M., Meneghini C., Brunelli M., Fitch A.N., Neri P., Langmuir 28 8511-8517 (2012).

[Evangelisti-12] Evangelisti C., Schiavi E., Aronica L.A., Caporusso A.M., Vitulli G., Bertinetti L., Martra G., Balerna A., Mobilio S. Bimetallic, Journal of Catalysis 286 224-236 (2012).

[Giuli-12] Giuli G., Cicconi M.R., Paris E., European Journal of Mineralogy 24 783-790 (2012).

[Jana-12] Jana S., Meneghini C., Sanyal P., Sarkar S., Saha-Dasgupta T., Karis O., Ray S., Physical Review B 86 054433-1-054433-6 (2012).

[Lassinantti-12] Lassinantti Gualtieri M., Romagnoli M., Miselli P., Cannio M., Gualtieri A.F., Cement and Concrete Research 42 1273-1279 (2012).

[Leardini-12a] Leardini L., Martucci A., Alberti A., Cruciani G., Microporous and Mesoporous Materials 167 117-126 (2012).

[Leardini-12b] Leardini L., Martucci A., Cruciani G., Microporous and Mesoporous Materials 151 163-171 (2012).

[Longo-12] Longo A., Liotta L.F., Pantaleo G., Giannici F., Venezia A.M., Martorana A., Journal of Physical Chemistry C 116 2960-2966 (2012).

[Macchi-12] Macchi C., Maurizio C., Checchetto R., Mariazzi S., Ravelli L., Egger W., Mengucci P., Bazzanella N., Miotello A., Somoza A., Brusa R.S., Physical Review B 85 214117-1-214117-19 (2012).

[Maurizio-12] Maurizio C., Mattei G., Mazzoldi P., Radiation Effects and Defects in Solids 167 478-486 (2012).

[Medas-12] Medas D., Cidu R., Lattanzi P., Podda F., De Giudici G., Soil Biology 31 113-130 (2012).

[Minguzzi-12] Minguzzi A., Locatelli C., Cappelletti G., Scavini M., Vertova A., Ghigna P., Rondinini S., Journal of Physical Chemistry A 116 6497-6504 (2012).

[Mohiddon-12a] Mohiddon M.A., Krishna M.G., Dalba G., Rocca F., Materials Science and Engineering B 177 1108-1112 (2012).

[Mohiddon-12b] Mohiddon M.A., Naidu K.L., Dalba G., Rocca F., Krishna M.G., Physica Status Solidi (c) 9 1493-1495 (2012).

[Oppo-12] Oppo C.I., Corpino R., Ricci P.C., Paul M.C., Das S., Pal M., Bhadra S.K., Yoo S., Kalita M.P., Boyland A.J., Sahu J.K., Ghigna P., d'Acapito F., Optical Materials 34 660-664 (2012).

[Pin-12] Pin S., Newton M.A., d'Acapito F., Zema M., Tarantino S.C., Spinolo G., de Souza R.A., Martin M., Ghigna P., Journal of Physical Chemistry C 116 980-986 (2012).

[Piskorska-12] Piskorska-Hommel E., Holý V., Caha O., Wolska A., Gust A., Kruse C., Kröncke H., Falta J., Hommel D., Journal of Alloys and Compounds 523 155-160 (2012).

[Ramamoorthy-12] Ramamoorthy R.K., Bhatnagar A.K., Rocca F., Mattarelli M., Montagna M., Journal of Physics Condensed Matter 24 505101-1-505101-8 (2012).

[Rossetti-12] Rossetti I., Mancini G.F., Ghigna P., Scavini M., Piumetti M., Bonelli B., Cavani F., Comite A., Journal of Physical Chemistry C 116 22386-22398 (2012).

[Sacerdoti-12] Sacerdoti M., Cruciani G., *"Comparison of Structural Changes upon Heating of Zorite and Na-ETS-4 by In Situ Synchrotron Powder Diffraction"* pp 187-197 in *Minerals as Advanced Materials II*, Krivovichev S. V. ed., Springer (2012).

[Saleta-12] Saleta M.E., Aurelio G., Bardelli F., Sánchez R.D., Malta M., Torresi R.M., Journal of Physics Condensed Matter 24 435302-1-435302-8 (2012).

[Santos-12] Santos L.F., Monteiro G., Almeida R.M., d'Acapito F.Ciencia & Tecnologia dos Materiais 24 138-142 (2012).

[Silvestri-12] Silvestri A., Tonietto S., d'Acapito F., Molin G., Journal of Cultural Heritage 13 137-144 (2012).

[Tougerti-12] Tougerti A., Llorens I., d'Acapito F., Fonda E., Hazemann J.L., Joly Y., Thiaudière D., Che M., Carrier X., Angewandte Chemie International Edition 51 7697-7701 (2012).

[Vachhani-12] Vachhani P.S., Dalba G., Ramamoorthy R.K., Rocca F., Sipr O., Bhatnagar A.K., Journal of Physics Condensed Matter 24 506001-1-506001-7 (2012).

[Vanginneken-12] van Ginneken M., Folco L., Cordier C., Rochette P., Meteoritics & Planetary Science 47 228-247 (2012).

[Bardelli-11a] Bardelli F., Barone G., Crupi V., Longo F., Majolino D., Mazzoleni P., Venuti V., Analytical and Bioanalytical Chemistry 399 3147-3153 (2011).

[Bardelli-11b] Bardelli F., Benvenuti M., Costagliola P., Di Benedetto F., Lattanzi P., Meneghini C., Romanelli M., Valenzano L., Geochimica et Cosmochimica Acta 75 3011-3023 (2011).

[Bardelli-11c] Bardelli F., Cattaruzza E., Gonella F., Rampazzo G., Valotto G., Atmospheric Environment 45 6459-6468 (2011).

[Battocchio-11] Battocchio C., Fratoddi I., Venditti I., Yarzhemsky V.G., Norov Y.V., Russo M.V., Polzonetti G., Chemical Physics 379 92-98 (2011).

[Bingham-11] Bingham P.A., Connelly A.J., Cassingham N.J., Hyatt N.C., Journal of Non-Crystalline Solids 357 2726-2734 (2011).

[Bonanni-11] Bonanni A., Sawicki M., Devillers T., Stefanowicz W., Faina B., Li T., Winkler T.E., Sztenkiel D., Navarro-Quezada A., Rovezzi M., Jakiela R., Grois A., Wegscheider M., Jantsch W., Suffczynski J., d'Acapito F., Meingast A., Kothleitner G., Physical Review B 84 035206-1-035206-11 (2011).

[Boscherini-11] Boscherini F., d'Acapito F., Galata S.F., Tsoutsou D., Dimoulas A., Applied Physics Letters 99 121909-1-121909-3 (2011).

[Bracco-11] Bracco S., Comotti A., Ferretti L., Sozzani P., Journal of the American Chemical Society 133 8982-8994 (2011).

[Carria-11] Carria E., Mio A.M., Gibilisco S., Miritello M., d'Acapito F., Grimaldi M.G., Rimini E., Electrochemical and Solid-State Letters 14 H480-H482 (2011).

[Cartechini-11] Cartechini L., Rosi F., Miliani C., d'Acapito F., Brunetti B.G., Sgamellotti A., Journal of Analytical Atomic Spectrometry 26 2500-2507 (2011).

[Chakraborty-11] Chakraborty S., Bardelli F., Mullet M., Grenèche J.M., Varma S., Ehrhardt J.J., Banerjee D., Charlet L., Chemical Geology 281 83-92 (2011).

[Cruciani-11] Cruciani G., Dalconi M.C., Dondi M., Meneghini C., Matteucci F., Barzanti A., Lorenzi G., Baldi G., Journal of Nanoparticle Research 13 711-719 (2011).

[dacapito-11] F. d'Acapito, Semic. Sci. Technol. **26**, 064004 ((2011).

[Deandres-11] de Andrés A., Espinosa A., Prieto C., García-Hernández M., Ramirez-Jimenez R., Lambert-Milot S., Masut R.A., Journal of Applied Physics 109 113910-1-113910-9 (2011).

[Deferri-11] De Ferri L., Arletti R., Ponterini G., Quartieri S., European Journal of Mineralogy 23 969-980 (2011).

[Delmoro-11] Del Moro S., Renzulli A., Tribaudino M., Journal of Petrology 52 541-564 (2011).

[Dibenedetto-11] Di Benedetto F., Da Pelo S., Caneschi A., Lattanzi P., Neues Jahrbuch fur Mineralogie - Abhandlungen 188 11-19 (2011).

[Fraboni-11] Fraboni B., Boscherini F., Fochuk P., Cavallini A., Journal of Applied Physics 110 053706-1-053706-4 (2011).

[Giannici-11] Giannici F., Messana D., Longo A., Martorana A., Journal of Physical Chemistry C 115 298-304 (2011).

[Gliozzo-11] Gliozzo E., Grassi N., Bonanni P., Meneghini C., Tomei M.A., Archaeometry 53 469-489 (2011).

[Liu-11] Liu Y., Hu C., Comotti A., Ward M.D., Science 333 436-440 (2011).

[Malherbe-11] Malherbe J., Isaure M.P., Séby F., Watson R.P., Rodriguez-Gonzalez P., Stutzman P.E., Davis C.W., Maurizio C., Unceta N., Sieber J.R., Long S.E., Donard O.F.X., Environmental Science and Technology 45 10492-10500 (2011).

[Mancini-11] Mancini A., Vannozzi A., Galluzzi V., Rufoloni A., Augieri A., Armenio A.A., Colantoni I., Davoli I., Celentano G., IEEE Transactions on Applied Superconductivity 21 2891-2895 (2011).

[Martucci-11] Martucci A., Pecorari P., Cruciani G., Microporous and Mesoporous Materials 142 570-576 (2011).

[Maurizio-11] Maurizio C., Trave E., Perotto G., Bello V., Pasqualini D., Mazzoldi P., Battaglin G., Cesca T., Scian C., Mattei G., Physical Review B 83 195430-1-195430-11 (2011).

[Mazzoldi-11] Mazzoldi P., Mattei G., Maurizio C., Trave E., Cesca T., Bello V., Mariazzi S., Brusa R.S., Radiation Effects and Defects in Solids 166 357-366 (2011).

[Messori-11] Messori L., Balerna A., Ascone I., Castellano C., Gabbiani C., Casini A., Marchioni C., Jaouen G., Congiu Castellano A., Journal of Biological Inorganic Chemistry 16 491-499 (2011).

[Middey-11] Middey S., Ray S., Mukherjee K., Paulose P.L., Sampathkumaran E.V., Meneghini C., Kaushik S.D., Siruguri V., Kovnir K., Sarma D.D., Physical Review B 83 144419-1-144419-8 (2011).

[Mino-11] Mino L., Gianolio D., Agostini G., Piovano A., Truccato M., Agostino A., Cagliero S., Martínez-Criado G., d'Acapito F., Codato S., Lamberti C., Small 7 930-938 (2011).

[Ottaviano-11] Ottaviano L., Continenza A., Profeta G., Impellizzeri G., Irrera A., Gunnella R., Kazakova O., Physical Review B 83 134426-1-134426-9 (2011).

[Pasquali-11] Pasquali L., Montecchi M., Nannarone S., Boscherini F., Journal of Physics Condensed Matter 23 355003-1-355003-11 (2011).

[Pasquini-11a] Pasquini L., Boscherini F., Callini E., Maurizio C., Pasquali L., Montecchi M., Bonetti E., Physical Review B 83 184111-1-184111-12 (2011).

[Pasquini-11b] Pasquini L., Callini E., Brighi M., Boscherini F., Montone A., Jensen T.R., Maurizio C., Antisari M.V., Bonetti E., Journal of Nanoparticle Research 13 5727-5737 (2011).

[Roscioni-11] Roscioni O.M., Zonias N., Price S.W.T., Russell A.E., Comaschi T., Skylaris C.K., Physical Review B 83 115409-1-115409-8 (2011).

[Tribaudino-11] Tribaudino M., Ohashi H., Periodico di Mineralogia 80 135-144 (2011).

[Agostini-10] Agostini G., Lamberti C., Palin L., Milanesio M., Danilina N., Xu B., Janousch M., van Bokhoven J.A., Journal of the American Chemical Society 132 667-678 (2010).

[Arletti-10a] Arletti R., Giacobbe C., Quartieri S., Sabatino G., Tigano G., Triscari M., Vezzalini G., Archaeometry 52 99-114 (2010).

[Arletti-10b] Arletti R., Quartieri S., Vezzalini G., American Mineralogist 95 1247-1256 (2010).

[Asta-10] Asta M.P., Ayora C., Román-Ross G., Cama J., Acero P., Gault A.G., Charnock J.M., Bardelli F., Chemical Geology 271 1-12 (2010).

[Battocchio-10] Battocchio C., Fratoddi I., Vitaliano R., Russo M.V., Polzonetti G., Solid State Sciences 12 1881-1885 (2010).

[Borghi-10] Borghi E., Casella L., Physical Chemistry - Chemical Physics 12 1525-1534 (2010).

[Bortolus-10] Bortolus M., Bisaglia M., Zoleo A., Fittipaldi M., Benfatto M., Bubacco L., Maniero A.L., Journal of the American Chemical Society 132 18057-18066 (2010).

[Campiglio-10] Campiglio P., Campione M., Canepa F., Canevali C., Cimberle M.R., Fanciulli C., Miozzo L., Moret M., Papagni A., Rizzato S., Sassella A., European Physical Journal B 73 495-501 (2010).

[Cataruzza-10] Cattaruzza E., Maurizio C., Visentin L., Trave E., Martucci A., Ali S., Battaglin G., Gonella F., Nuclear Instruments and Methods in Physics Research B 268 311-315 (2010).

[Chakraborty-10] Chakraborty S., Bardelli F., Charlet L., Environmental Science and Technology 44 1288-1294 (2010).

[Cotte-10] Cotte M., Auffan M., Degruyter W., Fairchild I., Newton M.A., Morin G., Sarret G., Scheinost A.C., Synchrotron Radiation News 23 28-35 (2010).

[Crupi-10] Crupi V., Majolino D., Venuti V., Barone G., Mazzoleni P., Pezzino A., La Russa M.F., Ruffolo S.A., Bardelli F., Applied Physics A 100 845-853 (2010).

[Cuberos-10] Cuberos A.J.M., De la Torre Á.G., Alvarez-Pinazo G., Martín-Sedeño M.C., Schollbach K., Pollmann H., Aranda M.A.G., Environmental Science and Technology 44 6855-6862 (2010).

[Dibenedetto-10] Di Benedetto F., d'Acapito F., Fornaciai G., Innocenti M., Montegrossi G., Pardi L.A., Tesi S., Romanelli M., Physics and Chemistry of Minerals 37 283-289 (2010).

[Folco-10] Folco L., Perchiazzi N., D'Orazio M., Frezzotti M.L., Glass B.P., Rochette P., Geology 38 211-214 (2010).

[Giachini-10] Giachini L., Veronesi G., Francia F., Venturoli G., Boscherini F., Journal of Synchrotron Radiation 17 41-52 (2010).

[Giacobbe-10] Giacobbe C., Gualtieri A.F., Quartieri S., Rinaudo C., Allegrina M., Andreozzi G.B., European Journal of Mineralogy 22 535-546 (2010).

[Giannici-10] Giannici F., Longo A., Kreuer K.D., Balerna A., Martorana A., Solid State Ionics 181 122-125 (2010).

[Giubertoni-10] Giubertoni D., Pepponi G., Sahiner M.A., Kelty S.P., Gennaro S., Bersani M., Kah M., Kirkby K.J., Doherty R., Foad M.A., Meirer F., Streli C., Woicik J.C., Pianetta P., Journal of Vacuum Science and Technology B 28 C1B1-C1B5 (2010).

[Giuli-10] Giuli G., Pratesi G., Eeckhout S.G., Koeberl C., Paris E., *"Iron reduction in silicate glass produced during the 1945 nuclear test at the Trinity site (Alamogordo, New Mexico, USA)"*, in *Large Meteorite Impacts And Planetary Evolution IV Book Series* Volume 465 pp 653-660, Gibson R. L., Reimold W. U. eds., Geological Society of America Special Paper (2010).

[Gliozzo-10] Gliozzo E., Santagostino Barbone A., d'Acapito F., Turchiano M., Turbanti Memmi I., Volpe G., Archaeometry 52 389-415 (2010).

[Gross-10] Gross S., Bauer M., Advanced Functional Materials 20 4026-4047 (2010).

[Gunnella-10] Gunnella R., Morresi L., Pinto N., Di Cicco A., Ottaviano L., Passacantando M., Verna A., Impellizzeri G., Irrera A., d'Acapito F., Journal of Physics Condensed Matter 22 216006-1-216006-10 (2010).

[Jabeen-10] Jabeen F., Piccin M., Felisari L., Grillo V., Bais G., Rubini S., Martelli F., d'Acapito F., Rovezzi M., Boscherini F., Journal of Vacuum Science and Technology B 28 478-483 (2010).

[Jana-10] Jana S., Singh V., Kaushik S.D., Meneghini C., Pal P., Knut R., Karis O., Dasgupta I., Siruguri V., Ray S., Physical Review B 82 180407-1-180407-4 (2010).

[Lattanzi-10a] Lattanzi P., Maurizio C., Meneghini C., De Giudici G., Podda F., European Journal of Mineralogy 22 557-564 (2010).

[LAttanzi-10b] Lattanzi P., Meneghini C., De Giudici G., Podda F., Journal of Hazardous Materials 177 1138-1144 (2010).

[Liscio-10] Liscio F., Maret M., Meneghini C., Mobilio S., Proux O., Makarov D., Albrecht M., Physical Review B 81 125417-1-125417-9 (2010).

[Mari-10] Mari A., Imperatori P., Marchegiani G., Pilloni L., Mezzi A., Kaciulis S., Cannas C., Meneghini C., Mobilio S., Suber L., Langmuir 26 15561-15566 (2010).

[Martinsedeno-10] Martín-Sedeño M.C., Cuberos A.J.M., De la Torre Á.G., Alvarez-Pinazo G., Ordóñez L.M., Gateshki M., Aranda M.A.G., Cement and Concrete Research 40 359-369 (2010).

[Maurizio-10a] Maurizio C., El Habra N., Rossetto G., Merlini M., Cattaruzza E., Pandolfo L., Casarin M., Chemistry of Materials 22 1933-1942 (2010).

[Maurizio-10b] Maurizio C., Perotto G., Mattei G., Trave E., Mazzoldi P., Nuclear Instruments and Methods in Physics Research B 268 3215-3218 (2010).

[Maurizio-10c] Maurizio C., Perotto G., Trave E., Pellegrini G., Mattei G., Mazzoldi P., Nuclear Instruments and Methods in Physics Research B 268 3219-3222 (2010).

[Navarro-10] Navarro-Quezada A., Stefanowicz W., Li T., Faina B., Rovezzi M., Lechner R.T., Devillers T., d'Acapito F., Bauer G., Sawicki M., Dietl T., Bonanni A., Physical Review B 81 205206-1-205206-11 (2010).

[Noun-10] Noun W., Popova E., Bardelli F., Dumont Y., Bertacco R., Tagliaferri A., Tessier M., Guyot M., Berini B., Keller N., Physical Review B 81 054411-1-054411-10 (2010).

[Pin-10] Pin S., *Studio dei primi istanti delle rezioni solido-solido (Probing the initial stages of solid state reactions),* Ph.D. Thesis, Univ. Pavia and Univ. J. Fourier Grenoble (2010).

[Somma-10] Somma F., Aloe P., d'Acapito F., Montereali R.M., Polosan S., Secu M., Vincenti M.A., IOP Conference Series: Materials Science and Engineering 15 012035-1-012035-5 (2010).

[Stefanowicz-10] Stefanowicz W., Sztenkiel D., Faina B., Grois A., Rovezzi M., Devillers T., d'Acapito F., Navarro-Quezada A., Li T., Jakiela R., Sawicki M., Dietl T., Bonanni A., Physical Review B 81 235210-1-235210-14 (2010).

[Tedesco-10] Tedesco C., Erra L., Immediata I., Gaeta C., Brunelli M., Merlini M., Meneghini C., Pattison P., Neri P., Crystal Growth & Design 10 1527-1533 (2010).

[Torchio-10a] Torchio R., Meneghini C., Mobilio S., Capellini G., García Prieto A., Alonso J., Fdez-Gubieda M.L., Liveri V.T., Longo A., Ruggirello A.M., Neisius T., Journal of Magnetism and Magnetic Materials 322 3565-3571 (2010).

[Torchio-10b] Torchio R., Meneghini C., Mobilio S., Capellini G., Prieto A.G., Alonso J., Fdez-Gubieda M.L., Liveri V.T., Longo A., Ruggirello A., Neisius T., Journal of Physics: Conference Series 200 072100-1-072100-4 (2010).

[Vanginneken-10] van Ginneken M., Folco L., Perchiazzi N., Rochette P., Bland P.A., Earth and Planetary Science Letters 293 104-113 (2010).

[Veronesi-10a] Veronesi G., "*Advanced applications of x-ray absorption spectroscopy to the study of protein metal sites*", Ph.D. Thesis, Univ. Bologna (2010).

[Veronesi-10b] Veronesi G., Boschi C.D.E., Ferrari L., Venturoli G., Boscherini F., Vila F.D., Rehr J.J., Physical Review B 82 020101-1-020101-4 (2010).

[Veronesi-10c] Veronesi G., Whitehead S.J., Francia F., Giachini L., Boscherini F., Venturoli G., Cotton N.P.J., Jackson J.B., Biochimica et Biophysica Acta 1797 494-500 (2010).

[Afify-09a] Afify N.D., Dalba G., Rocca F., Journal of Physics D 42 115416-1-115416-11 (2009).

[Afify-09b] Afify N.D., Mountjoy G., Physical Review B 79 024202-1-024202-12 (2009).

[Ahmed-09] Ahmed S.I., Dalba G., Fornasini P., Vaccari M., Rocca F., Sanson A., Li J., Sleight A.W., Physical Review B 79 104302-1-104302-8 (2009).

[Bardelli-09a] Bardelli F., Cattaruzza E., Gonella F., Rampazzo G., Valotto G., Journal of Physics: Conference Series 190 012192-1-012192-4 (2009).

[Bardelli-09b] Bardelli F., Meneghini C., Mobilio S., Ray S., Sarma D.D., Journal of Physics Condensed Matter 21 195502-1-195502-9 (2009).

[Bonanni-09] Bonanni A., Nanotechnology, 2009. IEEE-NANO 2009. 9th IEEE Conference on , vol., no., pp.426,431, 26-30 July 2009.

Maurizio C., Ali S., Trave E., Journal of Physics D 42 045301-1-045301-5 (2009).

[Cespedes-09] Céspedes E., Román E., Huttel Y., Chaboy J., García-López J., de Andrés A., Prieto C., Journal of Applied Physics 106 043912-1-043912-10 (2009).

[Cicconi-09] Cicconi M.R., Giuli G., Paris E., Ertel-Ingrisch W., Dingwell D.B., Journal of Physics: Conference Series 190 012179-1-012179-4 (2009).

[Colonna-09] Colonna S., Cricenti A., Luches P., Valeri S., Boscherini F., Qi J., Xu Y., Tolk N., Superlattices and Microstructures 46 107-113 (2009).

[Comaschi-09] Comaschi T., Balerna A., Mobilio S., Journal of Physics Condensed Matter 21 325404-1-325404-9 (2009).

[Cuberos-09] Cuberos A.J.M., De la Torre Á.G., Martín-Sedeño M.C., Moreno-Real L., Merlini M., Ordónez L.M., Aranda M.A.G., Cement and Concrete Research 39 833-842 (2009).

[Cuello-09] Cuello G.J., Román-Ross G., Fernández-Martínez A., Sobolev O., Charlet L., Skipper N.T., *Pollutant Speciation in Water and Related Environmental Treatment Issues*,   pp 491-520 in *Neutron Applications in Earth, Energy and Environmental Sciences*, Liang L. Rinaldi R., Schober H. Eds., Springer US (2009).

[Dinoto-09] Di Noto V., Boer A.B., Lavina S., Muryn C.A., Bauer M., Timco G.A., Negro E., Rancan M., Winpenny R.E.P., Gross S., Advanced Functional Materials 19 3226-3236 (2009).

[Folco-09] Folco L., D'Orazio M., Tiepolo M., Tonarini S., Ottolini L., Perchiazzi N., Rochette P., Glass B.P., Geochimica et Cosmochimica Acta 73 3694-3722 (2009).

[Fornasini-09] Fornasini P., Abd el All N., Ahmed S.I., Sanson A., Vaccari M., Journal of Physics : Conference Series 190 012025-1-12025-6 (2009).

[Giannici-09a] Giannici F., Longo A., Balerna A., Kreuer K.D., Martorana A., Chemistry of Materials 21 2641-2649 (2009).

[Giannici-09b] Giannici F., Longo A., Balerna A., Martorana A., Chemistry of Materials 21 597-603 (2009).

[Giannici-09c] Giannici F., Placido T., Curri M.L., Striccoli M., Agostiano A., Comparelli R., Dalton Transactions 10367-10374 (2009).

[Gualtieri-09] Gualtieri A. F., Lassinantti-Gualtieri M., Meneghini C., Zeitschrift für Kristallographie Supplements 30 353-358 (2009).

[Kulkarni-09] Kulkarni S.R., Merlini M., Phatak N., Saxena S.K., Artioli G., Amini S., Barsoum M.W., Journal of Alloys and Compounds 469 395-400 (2009).

[Malferrari-09] Malferrari D., Brigatti M.F., Elmi C., Laurora A., Valdré G., Zeitschrift für Kristallographie 224 311-315 (2009).

[Maurizio-09a] Maurizio C., Quaranta A., Ghibaudo E., d'Acapito F., Broquin J.E., Journal of Physical Chemistry C 113 8930-8937 (2009).

[Maurizio-09b] Maurizio C., Rovezzi M., Bardelli F., Pais H.G., d'Acapito F., Review of Scientific Instruments 80 063904-1-063904-6 (2009).

[Meneghini-09] Meneghini C., Ray S., Liscio F., Bardelli F., Mobilio S., Sarma D.D., ,Physical Review Letters 103 046403 -1-046403-4 (2009).

[Noe-09] Noé P., Okuno H., Jager J.B., Delamadeleine E., Demichel O., Rouvière J.L., Calvo V., Maurizio C., d'Acapito F., Nanotechnology 20 355704-1-355704-8 (2009).

[Ori-09a] Ori S., Mazzucato E., Vezzalini G., American Mineralogist 94 64-73 (2009).

[Ori-09b] Ori S., Vezzalini G., Galli E., Microporous and Mesoporous Materials 126 171-181 (2009).

[Pin-09] Pin S., Ghigna P., Spinolo G., Quartarone E., Mustarelli P., d'Acapito F., Migliori A., Calestani G., Journal of Solid State Chemistry 182 1291-1296 (2009).

[Piskorska-09] Piskorska-Hommel E., Wolska A., Flege J.I., Gust A., Kruse C., Hommel D., d'Acapito F., AIP Conference Proceedings 1199 531-532 (2009).

[Placido-09] Placido T., Comparelli R., Giannici F., Cozzoli P.D., Capitani G., Striccoli M., Agostiano A., Curri M.L., Chemistry of Materials 21 4192-4202 (2009).

[Rovezzi-09a] Rovezzi M., *Étude de l'ordre locale autour d'impuretés magnétiques dans les semiconducteurs pour l'électronique de spin (Study of the local order around magnetic impurities in semiconductors for spintronics)*, Ph.D. Thesis, Univ. J. Fourier Grenoble (2009).

[Rovezzi-09b] Rovezzi M., d'Acapito F., Navarro-Quezada A., Faina B., Li T., Bonanni A., Filippone F., Bonapasta A.A., Dietl T., Physical Review B 79 195209-1-195209-9 (2009).

[Sipr-09] Sipr O., Rocca F., Fornasini P., Journal of Physics Condensed Matter 21 255401-1-255401-9 (2009).

[Soldatov-09] Soldatov M.A., Ascone I., Congiu-Castellano A., Messori L., Cinellu M.A., Balerna A., Soldatov A.V., Yalovega G.E., Journal of Physics : Conference Series 190 012210-1-12210-4 (2009).

[Tribaudino-09] Tribaudino M., Bromiley G., Ohashi H., Nestola F., Physics and Chemistry of Minerals 36 527-536 (2009).

[Vandermeulen-09] van der Meulen M.I., Petkov N., Morris M.A., Kazakova O., Han X., Wang K.L., Jacob A.P., Holmes J.D., Nano Letters 9 50-56 (2009).

[Zoppi-09] Zoppi M., Pratesi G., Acta Crystallographica E 65 i6-i7 (2009).